Building a Better Flat-Field: An Instrumental Calibration Projector for the Large Synoptic Survey Telescope

by

Amali L. Vaz

Submitted to the Department of Physics
in partial fulfillment of the requirements for the degree of

Bachelor of Science in Physics

at the

MASSACHUSETTS INSTITUTE OF TECHNOLOGY

February 2011

Author .....
Department of Physics
January 14, 2011

Certified by .....
Christopher Stubbs
Professor of Physics and of Astronomy, Harvard University
Thesis Supervisor

Certified by .....
Nergis Mavalvala
Professor of Physics, Massachusetts Institute of Technology
Thesis Supervisor

Accepted by .....
Nergis Mavalvala
Senior Thesis Coordinator

Building a Better Flat-Field: An Instrumental Calibration Projector for the Large Synoptic Survey Telescope

by

Amali L. Vaz

Submitted to the Department of Physics
on January 14, 2011, in partial fulfillment of the
requirements for the degree of
Bachelor of Science in Physics

Abstract

The Large Synoptic Survey Telescope (LSST) is a next-generation ground-based survey telescope whose science objectives demand photometric precision at the 1% level. Recent efforts towards 1% photometry have advocated in-situ instrumental calibration schemes that use a calibrated *detector*, rather than a celestial *source*, as the fundamental reference point for all measurements of system throughput. Results have been promising, but report systematic errors due to stray and scattered light from the flat-field screens used. The LSST calibration scheme replaces the traditional Lambertian-scattering flat-field screen with an array of projectors whose light is constrained in angle, thereby minimizing scattered light incident on the detector. This thesis presents the construction and testing of a single prototype projector within the LSST array. In particular, we evaluate the use of Engineered Diffusers to define the angular radiance of incident light, and of either a Fresnel lens or parabolic mirror to collimate that light. We find that flat-top Engineered Diffusers produce light that is constrained in angle, but which shows persistent pixel-to-pixel non-uniformity at the 5-10% level, and color-to-color non-uniformity at the 5-15% level; unless compensated, chromatic non-uniformity renders them unsuitable for our purposes. The additional chromatic aberrations introduced by Fresnel lens collimators render such transmissive collimators infeasible. Nevertheless, we demonstrate the soundness of the flat-field projector concept by constructing an alternative projector prototype, based on an integrating sphere, that satisfies each criterion well within our tolerances. The magnitude of improvement granted by the integrating sphere projector suggests that future work further investigate this approach.

Thesis Supervisor: Christopher Stubbs
Title: Professor of Physics and of Astronomy, Harvard University

Thesis Supervisor: Nergis Mavalvala
Title: Professor of Physics, Massachusetts Institute of Technology

Acknowledgments

To call this thesis *mine* might suggest that it is the work of one cloistered laboratory scholar. Let me be clear: it isn't. I owe a great debt of gratitude to my supervisor, Prof. Stubbs, as well as to my project collaborators: Peter Doherty, Bill Gressler, Ming Liang, Victor Krabbendam, and the wider group of physicists and astronomers at Harvard and within the LSST group who have contributed to this work. Thank you all.

Additional thanks go to my family, who have awaited my graduation with infinite patience, for their support throughout my time at MIT. My nieces, too, deserve a special mention, for making me laugh and always knowing what chapter I was working on (I'm done now). To Mr. Spock, Isaac Asimov, and Diana Kelley: thank you for the awesome. To pLep and the Internets, thanks for being encouraging. And to Gautham Narayan, for his patient good humor in the face of unremitting thesis-panic, for midnight explanations of equations of state, and also for the waffles. Mmm, waffles.

Contents

List of Figures

List of Tables

Chapter 1

Introduction

The Large Synoptic Survey Telescope (LSST) is a proposed wide-field large-aperture ground based optical survey telescope. From the summit of Cerro Pachon, in the Chilean Andes, it will survey the visible night sky for a period of ten years with a cadence of four days. The LSST's final product will be a data set of unprecedented sky coverage, cadence, and depth: it will see more of the sky more frequently and with fainter objects than any previous astronomical survey.

The LSST is a *photometric* instrument. It counts the photoelectrons registered at each pixel of its CCD detector, thereby measuring the apparent brightness of each celestial object in its field of view. Brightness data can then be analyzed to reveal not only how bright an object is – its astronomical *magnitude* – but also whether that magnitude is changing, and by how much. Relative magnitudes between different broadband filters, each spanning a separate range of wavelengths, can be compared to determine an object's *color*.

Astronomical CCD detectors convert incident photons into photoelectric measurements. But of those photons from a given source that reach the Earth, some will be scattered or absorbed by Earth's atmosphere; others may scatter from optical surfaces inside the telescope. The broadband astronomical filter in place transmits more photons at one wavelength than another. Individual pixels on the detector vary in their intrinsic sensitivity. Nor is the amount of light lost constant: mirrors will dull with time; filters will degrade; cosmic rays

will damage detector pixels; dust will settle over the instruments.

In order to perform photometry, we need to determine how much light is lost between the top of the Earth's atmosphere and the electronic detector: we must photometrically *calibrate* the telescope and its instruments. This thesis focuses only on *relative* photometric calibration, with the aim of achieving *precise* photometric measurements; the *absolute* calibration which ties measured flux to astronomical magnitudes, and which is responsible for photometric *accuracy*, is a separate topic and is not considered here.

What follows in this chapter is an attempt to motivate the work of this thesis – the construction of an instrumental calibration system designed to improve photometric precision – by noting that traditional calibration methodology is inadequate for several of the LSST's scientific objectives.

1.1 Current instrumental calibration procedures

Most current astronomical observatories calibrate their instruments using a white screen that acts as a diffuse reflector. Standard practice is to illuminate this screen with broadband "white" light, point the telescope directly at the screen, and take a series of images through each of the telescope's bandpasses. What results is a *flat-field* image – a frame awash with light that would, in the ideal case, be uniform, but which instead is marked with the characteristic shadows and out-of-focus rings of dust on the optics, scratches on the filters, edge-effects of the detector, and other irregularities. The array of flat-field values at each pixel is used as a multiplicative corrector for raw data in the relevant passband.

Within a given passband, and at a given pixel, the flat-field is a simple scalar value. Therefore, flat-fielding presupposes that the spectral energy distribution (SED) within that passband is identical for every source detected at that pixel. In on-sky data, though, multiple sources with different SEDs might easily contribute to the measured flux in a single pixel. Traditional flat-fielding is therefore limited in the photometric precision it can achieve.

Under current methodology, photometric measurements between different fields, or at different times, are plagued by fractional uncertainties in magnitudes on the order of a few

percent. For example, the Sloan Digital Sky Survey (SDSS), which obtained multi-color images over more than a quarter of the sky, quotes (Stoughton et al., 2002) a systematic uncertainty in the photometric zeropoint of 2% across the fields it imaged. A comparison (Saha et al., 2005) of photometric precision reported by multiple sources found systematic discrepancies at the level of 2% - 5%. Although photometric measurements at this level are sufficient for their intended purpose – measuring stellar magnitudes – there are astronomical questions providing real impetus for photometry with still finer precision.

1.2 The case for 1% photometry

The LSST has science programs that demand photometric precision at the 1% level, and for which differential single-frame photometry is impractical. A few such programs are discussed here, as concrete examples of the interplay between precision photometry and science results.

1.2.1 The formation history of the Solar System

Sky surveys are ideal for detecting and classifying the multitudes of "minor planets" – asteroids and comets – populating the Solar System. These bodies orbit singly, or in swarms, belts, and clouds, at distances spanning the breadth of the Solar System, from those near Earth to the distant Kuiper Belt and Oort Cloud.

Within the large group of main-belt asteroids, we have found "families" of bodies that share similar orbital parameters as well as the similar colors that indicate similar composition. Models suggest that these families shared a common formation history: that they were formed in the same region of space around the same time. Asteroids in such families can serve as dynamical tracers, acting as "test particles" whose observed motion provides a record of any earlier perturbation.

Minor planets in the outer Solar System, especially those at Neptune's orbit and beyond, provide a fossil history of the Solar System. They are so distant from the sun that minimal heating, melting, or outgassing has altered their chemical composition post-formation.

Mapping of family clusters within the Kuiper Belt would provide dynamical traces of the history of the outer solar system. Objects at such distances, though, require discerning instrumentation and careful measurement to detect and classify.

Asteroid taxonomy proceeds by comparison of observed color, measured as the ratio of detected flux in separate passbands: spectroscopy with a broad-passband brush. The variation between families can be subtle, and depends on how precisely each passband's flux is known. To separate populations, color-based taxonomy requires photometry better than 1-2% (Ivezić et al., 2008).

1.2.2 Mapping the Milky Way

A similar mapping of stellar populations can trace the makeup of the Milky Way. Just as relative colors separate asteroid populations, the color magnitudes of stars determine stellar type. To separate hydrogen-burning stars from aging giant stars, for instance, also requires photometric precision of 1% across passbands (Ivezić, 2010).

Additionally, precise photometry allows for the mapping of Galactic features such as interstellar dust and tidal streams. Dust between stars absorbs light, making distant objects appear dimmer; this dimming must, of course, be accounted for. But the amount of dust absorption can depend on wavelength. In turn, absorption then skews the relative color measurements of a star seen through dust. It is important to carefully measure the profile of Galactic dust – a task which becomes more difficult as the density of the dust column decreases. Determining the wavelength dependence of interstellar dust requires photometric precision of at least 2% (Ivezić, 2010).

Tidal streams arise from gravitaional interactions that rip apart a star cluster, drawing the component stars along ribbonlike streams that wrap the Galaxy. Detecting these streams allows for mapping of the gravitational potential of the Galaxy as a whole. Tidal streams are difficult to detect, though, because they require separating faint background stream stars from a field of foreground stars. Detection usually requires careful analysis of stellar types in a certain field, and selective filtering of only those stars whose color-magnitude profile matches

that expected of stars born in a particular variety of cluster. More precise photometric measurements allow for a narrower color-magnitude filter, and thereby the detection of more tidal streams.

1.2.3 Constraining cosmic expansion

The equation of state parameter of the dark energy gives the ratio of its pressure to density: $w = P/\rho$. Constraining the value of w can provide clues as to the nature and behavior of the dark energy.

Placing constraints on w requires a careful measurement of cosmic expansion. Type Ia supernovae are often used as "standard candles" for such measurements, because observations of their light curves and spectra allow derivation of each supernova's intrinsic luminosity. A comparison of luminosity distance to redshift over supernovae across the sky generates data that constrains the shape of the Hubble brightness-redshift relationship (Kent et al., 2009). Supernova luminosity and redshift measurements demand careful calibration of the relative sensitivity in the astronomical passbands measured. Precision at the level of 1% or better is required for supernova flux measurements; the difference between models with different values for cosmological parameters can be as fine as 0.02 magnitudes, or 2% photometric precision. Figure 1-1 depicts a few such models of cosmological parameters.

The Supernova Legacy Survey team (SNLS), which is attempting to measure w, implicates photometric calibration as their dominant source of systematic uncertainty (Regnault et al., 2009).

1.3 Outline of this thesis

The main body of work presented in this thesis concerns the laboratory construction and optical testing of prototype elements in the LSST's instrumental calibration system. Chapter 2 formalizes the calibration problem, and details recent work that has been done, at various other telescopes, to implement the revised calibration philosophy adopted by the LSST.

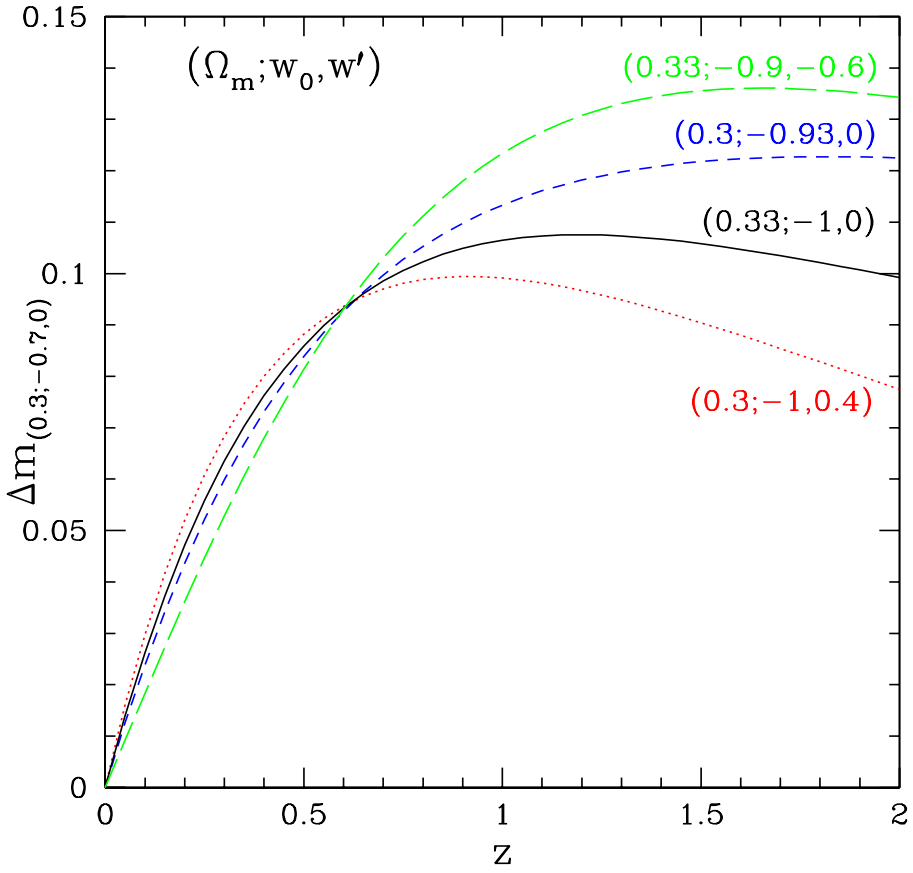

Figure 1-1: Differential magnitude-redshift diagram for dark energy models. Note that the difference between models is only 0.02 magnitudes: placing constraints on one or another model requires precision in supernova flux measurements of 1% or better. Figure from Linder and Huterer (2003).

Chapter 3 describes the calibration system we propose to use at the LSST, and gives an overview of the engineering constraints, optical requirements, and optical design we are testing. Chapter 4 describes the benchtop testing setup in our laboratory, and introduces the analytical procedures used in evaluation of each prototype. Chapters 5 and 6 provide an analysis of each component piece used, and a comparison of options where more than one is available; Chapter 7 discusses tests of full projector prototypes. Finally, Chapter 8 summarizes the results of benchtop testing, extrapolates those results to the final LSST system, and discusses future avenues of investigation.

Work detailed here represents a collaborative effort between researchers at Harvard University, the National Optical Astronomy Observatory, and the much larger collaboration that makes up the LSST group. In particular, Ming Liang (personal communication, July 2010) and Bill Gressler (Gressler et al., 2010) are responsible for the optical design of the projector prototypes tested here, and this thesis builds on philosophical (Stubbs and Tonry, 2006) and experimental foundations established by Stubbs et al (2007, 2010).

Laboratory setup and benchtop testing – Chapters 4 through 7 – represent the work of the author.

Chapter 2

Improving Photometric Calibration

Ground-based photometry involves the measurement of a celestial source by an Earthbound detector. Any measurement of that source is subject to the combined efficiencies of all intervening media: Earth's atmosphere, the optics in the telescope, and the detector itself. Photometry of the source is limited in precision by the degree to which we can account for the effects of the transmission chain.

Stubbs and Tonry (2006) advocate the following as steps in approaching the problem of 1% photometry:

1. Separating the systematic errors due to atmospheric effects from those due to the response of the telescope and detector.

2. Measuring telescope and detector response together, as a single relative "instrumental response" quantity.

3. Adopting a calibrated detector, rather than a celestial source, as the standard against which all throughput measurements on a given telescope will be compared.

This chapter formalizes the instrumental calibration problem and outlines experimental work that has been done toward 1% precision, based on the philosophy outlined above.

2.1 Calibration arithmetic

We formalize the relationship between source flux and measured counts according to the treatment outlined in Stubbs and Tonry (2006).

The photon flux from a source incident at the top of the atmosphere, $\mathcal{F}$, has a particular spectral energy density (SED) which introduces a dependence on wavelength λ. The intensity I of light from that source incident upon the telescope's entrance aperture is then a function of wavelength, pointing angle $\boldsymbol{\beta}$ of the telescope's optical axis, incident angle $\boldsymbol{\alpha}$ relative to the optical axis, and time.Because the source flux is subject to atmospheric effects, I is equal to $\mathcal{F}$ weighted by an atmospheric transmission function T:

$$I(\lambda, \boldsymbol{\alpha}, \boldsymbol{\beta}, t) = \mathcal{F}(\lambda, \boldsymbol{\alpha}, \boldsymbol{\beta}) T(\lambda, \boldsymbol{\alpha}, \boldsymbol{\beta}, t). \tag{2.1}$$

Optics within the telescope transfer incoming light to the telescope's focal plane. An astronomical telescope is designed to image sources that are essentially infinitely distant. The telescope functions, therefore, as a linear optical system that maps the *angle* of incident light onto *position* at the focal plane. Focal plane intensity Φ at focal plane coordinates $\boldsymbol{x}$ is related to incoming photon flux I at entrance aperture coordinates $\boldsymbol{x'}$ by means of a transfer function H:

$$\Phi(\boldsymbol{x}, \boldsymbol{\beta}, t, \lambda, P) = \int I(\boldsymbol{x'}, \boldsymbol{\alpha}, \boldsymbol{\beta}, t, \lambda, P) H(\boldsymbol{x}, \boldsymbol{x'}, \boldsymbol{\alpha}, \boldsymbol{\beta}, t, \lambda, P) d^2\boldsymbol{x'} d^2\boldsymbol{\alpha} \tag{2.2}$$

Here, focal plane intensity is a function not only of position $\boldsymbol{x}$ and pointing angle $\boldsymbol{\beta}$, but of time, wavelength λ, and polarization P. In this discussion, the effects of polarization are suppressed.

A contemporary astronomical instrument generally places a charge-coupled device (CCD) detector at the focal plane of the telescope. The CCD converts the incident photon flux Φ at detector-plane position $\boldsymbol{x}$ into a photoelectric count S, where S is the integral of Φ over wavelengths within a passband b, weighted by the detector quantum efficiency Q:

$$S_b(\boldsymbol{x}) = \int_b \Phi(\boldsymbol{x}, \lambda) Q(\boldsymbol{x}, \lambda) d\lambda \tag{2.3}$$

Q is generally assumed to depend only weakly on sub-pixel location, angle of arrival of incident light, or polarization.

Ground-based photometry seeks to convert the measured quantity $S(\boldsymbol{x})$, the distribution of photoelectrons across detector pixels, back to $\mathcal{F}(\lambda)$, the photon spectra of the source. In order to do so, we must understand the effects of 1) the atmospheric transmission T, 2) the optical transfer function of the apparatus, H, and 3) the detector quantum efficiency Q. This thesis is concerned only with the relative instrumental calibration required by points 2) and 3) – that is, with the determination of total light loss between the telescope's entrance aperture and its focal-plane measurement. Although work on atmospheric calibration has proceeded in parallel (for instance, in Stubbs et al. (2007a)), it is a problem to be treated separately, and is not discussed further here; neither do we discuss conversion between detected counts and stellar magnitudes.

2.2 Building a better flat-field

The problem of improving instrumental calibration is that of more precisely measuring the *total effect* of the optical transfer function H and detector quantum efficiency Q. Standard practice has been to measure each element of the optical train separately: filter transmission curves are specified by the manufacturer; detector efficiency is measured on the lab bench. But such a piecemeal approach suffers from cumulative systematic errors, whose effect is to limit achievable precision. Neither does the combined throughput measurement of the apparatus, with each component measured separatly, grant resolution of the instrumental response at the pixel scale.

Stubbs and Tonry (2006) advocate bundling the optical apparatus and detector terms above – H and Q – into a single product representing the spectral response of each pixel on the detector. The response of each pixel i with wavelength, $R_i(\lambda)$, can then be *measured*

in-situ, in such a way as to determine the total throughput of the system *relative* to some specified metrology standard.

Current practice uses *spectrophotometric standards* – stars of measured spectral energy density – as metrology standards for flat-field measurements. But such a measurement is only good to the degree that the stellar SEDs are known – generally only to within 1-2% percent (Bohlin, 2007) . Stubbs and Tonry (2006) propose instead that the standard of flux throughput metrology should be not a celestial *source*, but instead a calibrated *detector*. The National Institute of Standards and Technology (NIST) has measured the quantum efficiency (QE) of a Silicon photodiode to the 10^{-3} level (Stubbs et al., 2010; Eppeldauer et al., 2009) – a precision better than any spectrophotometric standard. Figure 2-1 shows the measured QE and fractional uncertainty in that measurement for one such photodiode.

What we seek to build, then, is a "better" flat-field: one that allows measurement of instrumental throughput, at the resolution of a single pixel, to monochromatic light, and which is tied to a precisely determined metrology standard.

2.3 Recent work

Recent work has been done to implement, on existing telescopes, the philosophy outlined in Stubbs and Tonry (2006): to perform in-situ throughput calibration by measuring the response of each pixel with wavelength, relative to a calibrated photodiode.

2.3.1 CTIO Blanco

Stubbs et al. (2007b) reported successful implementation of a monochromatic, photodiode-standardized throughput calibration system with the CTIO Mosaic imager and 4-meter Blanco telescope. The Blanco apparatus used a tunable laser as the primary source of photons. Light from the laser was fed through an optical fiber and projected onto a diffuse reflective flat-field screen. A NIST calibrated photodiode was placed inside a pinhole camera at the telescope's prime focus. To operate the system, the flat-field screen was fed monochro-

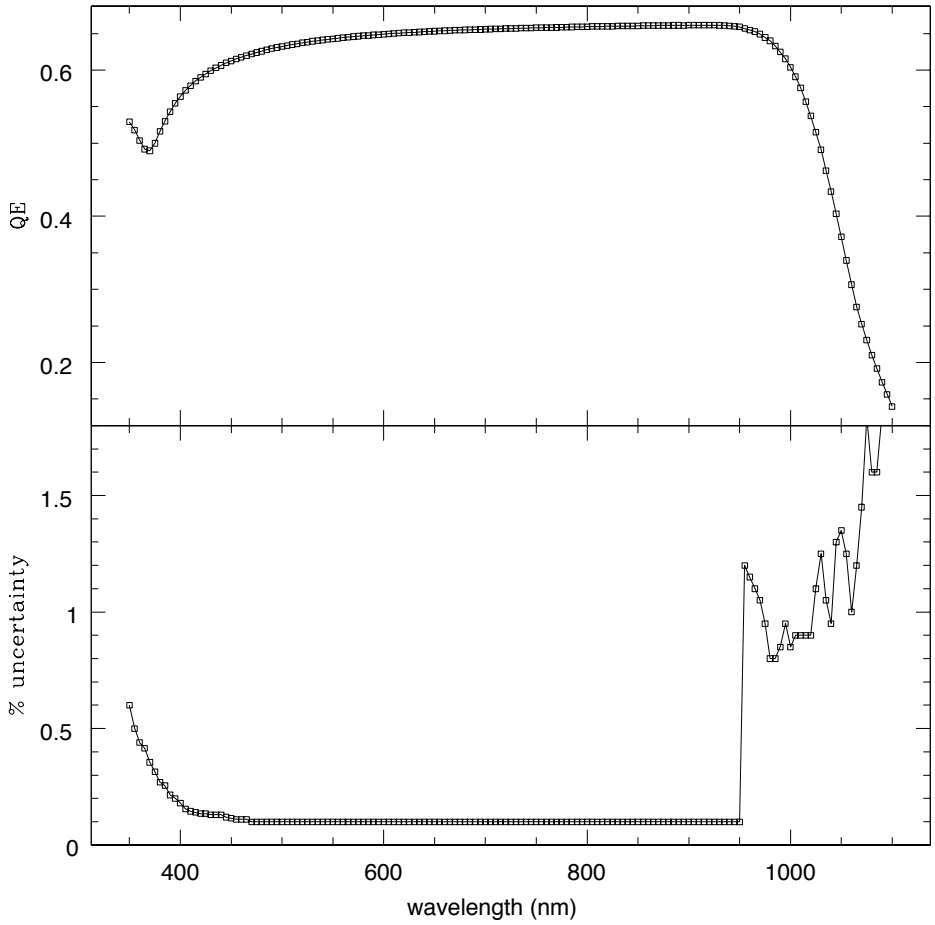

Figure 2-1: Quantum efficiency and fractional uncertainty of a NIST calibrated photodiode. The upper plot shows photon detection efficiency as a function of wavelength; the lower plot shows fractional uncertainty in QE measurements. Fractional uncertainty is at the level of 0.1% across most of the spectrum used by optical astronomy. The discontinuity in uncertainty at λ >950nm arises from a difference in metrology method used by NIST. Recent work at NIST (Eppeldauer et al., 2009) extends precision calibration of photodiodes out to 1.6μm, with the possibility of 0.01% precision. Figure from (Stubbs et al., 2010).

matic illumination, and the resulting flux detected by the Mosaic instrument was compared to that measured by the photodiode. Results were promising: throughput measurements were reproducible to better than 1%, and were in good agreement with documented values for the detector quantum efficiency and filter transmission.

Two monochromatic flat-field images from the Blanco implementation are shown in Figure 2-2.

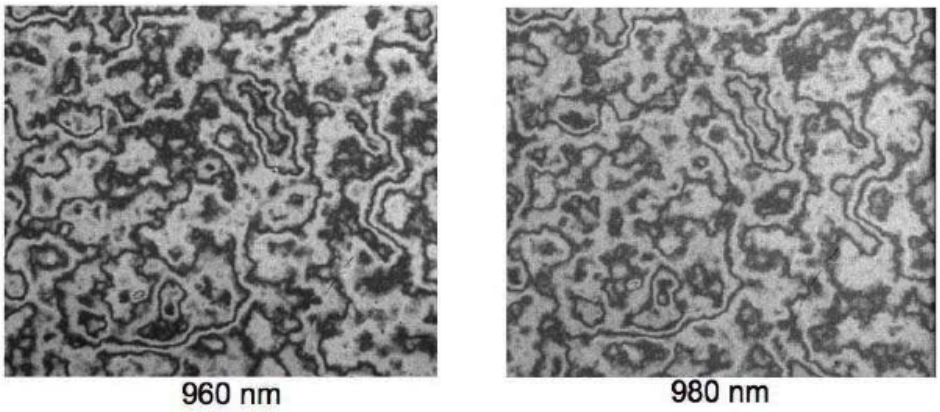

Figure 2-2: Measured fringing on a telescope detector (the CTIO Blanco) under flat monochromatic illumination. The phase shift in fringing patterns between 960 and 980nm indicates that a) interference effects can render throughput both pixel- and wavelength-dependent, and b) traditional flat-fields, which integrate over the passband of an astronomical filter, lack the wavelength resolution to account for these fringes. Figure reproduced from (Stubbs2007).

2.3.2 Pan-STARRS

A second version of the system was installed at the PanSTARRS telescope in Hawaii. Like the LSST, PanSTARRS is a survey telescope whose objective is photometric measurement of objects spanning a wide swath of sky. The PanSTARRS telescope has a 1.8-meter diameter primary mirror, in comparison to the LSST's 8.4 meters.

Space constraints in the PanSTARRS dome rendered the reflective-screen method of flat-field creation impractical. Instead, the team used a transmissive rear-projection screen. As

before, a NIST calibrated photodiode was used as reference. Figure 2-3 gives a schematic overview of the PanSTARRS setup.

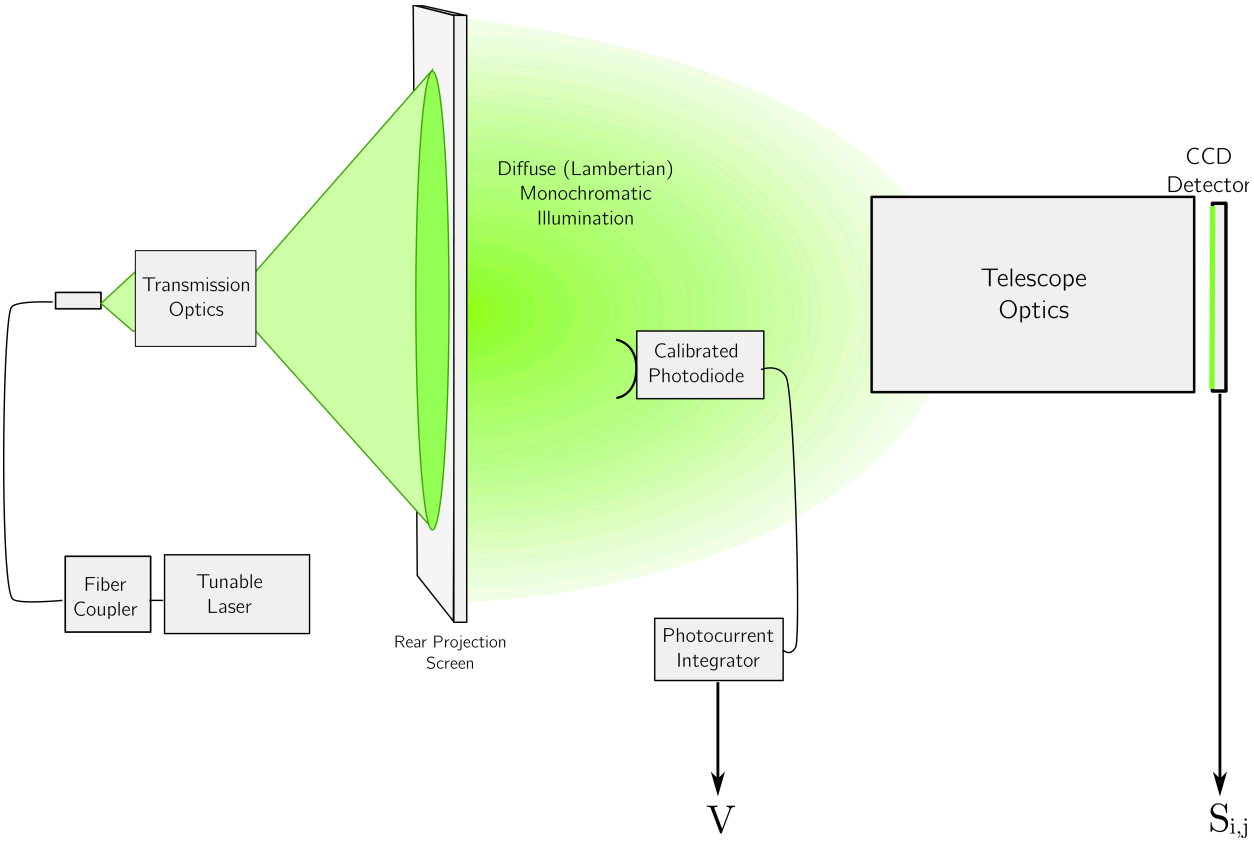

Figure 2-3: Diagram – not to scale! – of apparatus for relative system throughput calibration at PanSTARRS. Monochromatic light is rear-projected onto screen, producing Lambertian illumination. Flux from the screen is simultaneously measured by the photodiode and imaged onto the CCD detector; V and S are each measured once with the source on, and once off. The final measurement of relative system throughput is given as $R_(i,j,\lambda) = (S^{on}(i,j,\lambda) - S^{off}(i,j,\lambda)) \times \frac{QE_{diode}(\lambda)}{\Delta V_{on} - \Delta V_{off}}$, in arbitrary units.

To measure the system response function, the PanSTARRS team illuminated the screen with pulsed monochromatic laser light. Flux from the screen was simultaneously measured by the calibrated photodiode and imaged onto the CCD detector; measurements were taken once with the source on, and once with it off. The final measurement of relative system throughput R was given, in arbitrary units, as

$$R_(i,j,\lambda) = (S^{on}(i,j,\lambda) - S^{off}(i,j,\lambda)) \times \frac{QE_{diode}(\lambda)}{\Delta V_{on} - \Delta V_{off}} \tag{2.4}$$

Here S is the measured detector signal and V the voltage measured by the photodiode; i, j are the pixel coordinates on the detector, and λ is wavelength.

The PanSTARRS system has successfully demonstrated the ability to characterize full system throughput of the telescope and imager relative to a calibrated detector; their results are presented in Figure 2-4. The team was also able to measure filter transmission curves by dividing measurements taken with and without the filter (Figure 2-5).

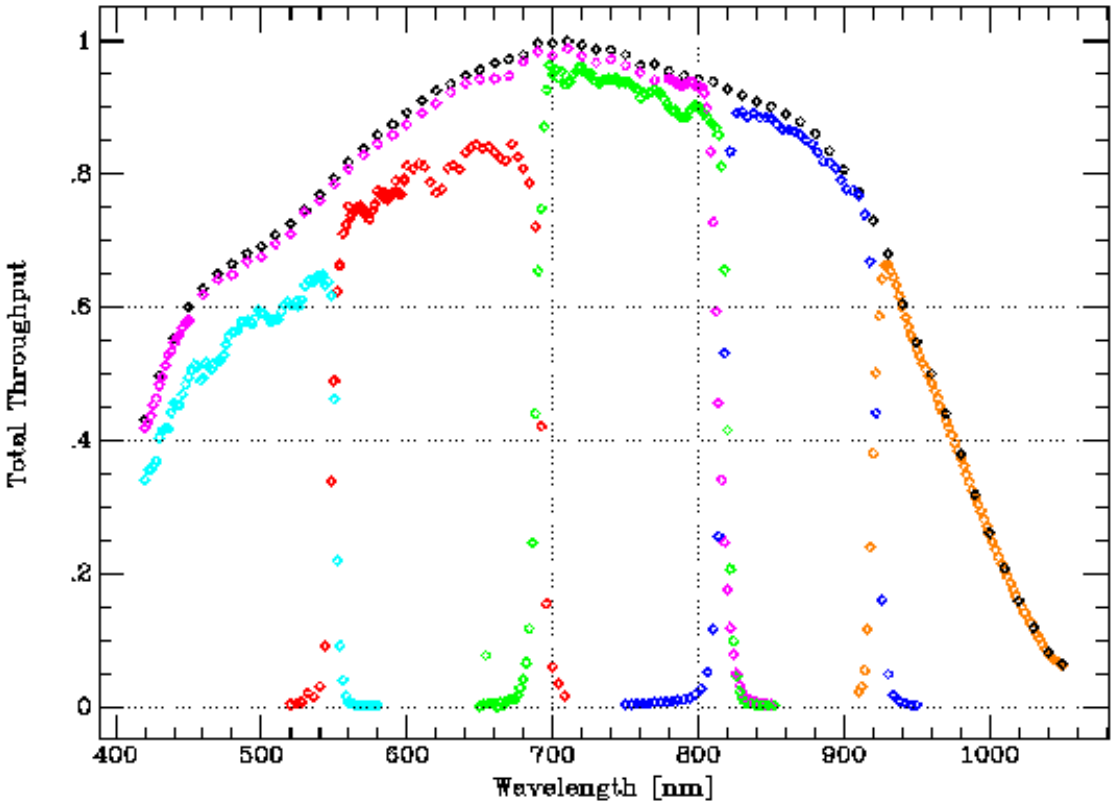

Figure 2-4: Relative system throughput calibration for the PanSTARRS telescope, using a filter set comprising g (cyan), r (red), i (green), z (blue), y (orange), w (purple) and open (black). All curves have been normalized to the peak sensitivity seen. Figure from Stubbs et al. (2010)

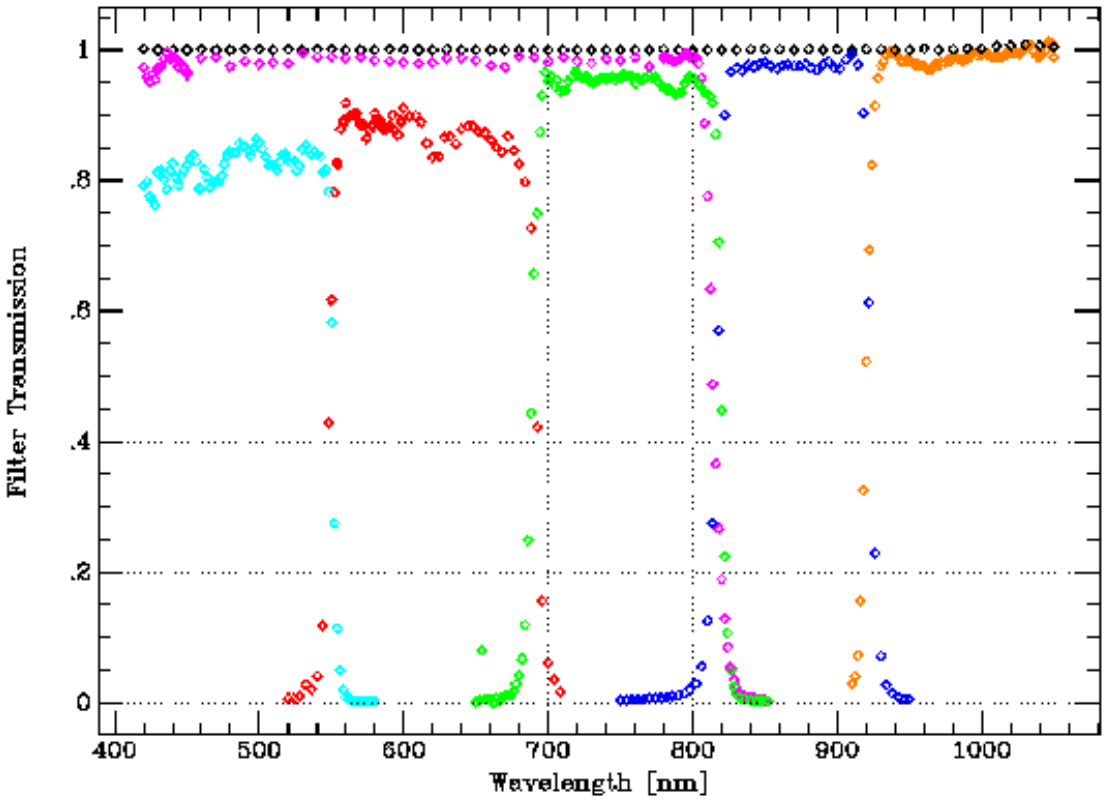

Figure 2-5: Filter-only transmission functions measured at PanSTARRS, for g (cyan), r (red), i (green), z (blue), y (orange), w (purple) and open (black). The vertical axis corresponds to absolute filter transmission. Figure from Stubbs et al. (2010).

The PanSTARRS measurements included estimates of systematic uncertainty in the calibration apparatus and technique. Of those, three arise from properties of the flat-field screen itself: the team estimates uncertainty at the 5% level arising from stray and scattered light paths, at 5% from wavelength-independent screen non-uniformity, and at 2% from wavelength-dependent screen non-uniformity.

Stray and scattered light arises from light on what would be non-focusing paths hitting the detector. Because scattered light may be wavelength-dependent – ghosting in the optics, for instance – it can introduce focal-plane variations that are then misinterpreted as variation in intrinsic sensitivity. Both the reflective flat-field screen used at the Blanco telescope and the transmissive PanSTARRS variant produced Lambertian scatter profiles, and consequently introduced a significant amount of stray light into the system.

While the ideal illumination would be completely uniform across the focal plane, a certain degree of non-uniformity can be tolerated, so long as the illumination pattern is constant with wavelength. Wavelength-independent non-uniformity can be compensated by simply rastering a celestial source across the detector. Any significant wavelength-dependent non-uniformity, though, undermines calibration efforts. If light intercepted by the photodiode has a different wavelength dependence than that incident on the detector pixels, systematic error is introduced even when comparing a single pixel's response across wavelengths.

Work presented in this thesis represents the next iteration in the cycle: from Blanco to PanSTARRS to the LSST. The design presented and tested in subsequent chapters is intended to address the major sources of uncertainty noted by the PanSTARRS team, in hope of achieving final uniformity of better than 1%. In addition, the proposed calibration scheme must conform to the particular engineering constraints imposed by the LSST itself. The next chapter introduces the LSST and outlines the calibration scheme proposed for implementation there.

Chapter 3

Calibrating the LSST

The LSST is designed for science work in four primary fields: constraining dark matter and dark energy, taking an inventory of the solar system, exploring optical transients, and mapping the Milky Way (LSST Science Collaborations et al., 2009). Each of these goals requires photometry at the 1% level across wide swaths of sky – that is, 1% photometry between images as well as within a single image. In accordance with its objectives, the LSST has been engineered to deliver precise and accurate photometry at the 1% level.

3.1 LSST overview

The LSST is a modified Paul-Baker telescope with a primary mirror diameter of 8.4 meters. Where many astronomical telescopes have two mirrors, the LSST has three; its design allows for a wide field of view which, coupled with its large collecting area, yields the exceptionally high throughput that is ideal for sky-survey work. In addition to its three mirrors, the LSST optical train includes three lenses serving as refractive correctors, a set of six astronomical filters – u,g,r,i, z, and y, with passbands similar to those of the Sloan Digital Sky Survey – and a 3.2 gigapixel CCD detector.

An in-situ calibration system at the LSST will allow monitoring of the total system throughput, measured as the combined effect of each mirror's reflectivity, each lens' trans-

Figure 3-1: Top: a model of the LSST in its enclosure. Bottom: a model of the LSST optics, including primary (bottom, outer annulus), secondary (top), and tertiary (bottom, inner annulus) mirrors, as well as refractive-correcting camera optics and detector (center). Both images credit: Todd Mason, Mason Productions, Inc. / LSST Corporation.

missivity, the filter passband shape, and the detector quantum efficiency, not only at the time of construction but also over the entire lifetime of the telescope, as frequently as desired. The instrumental calibration system is only one of several parallel calibration methods planned for concurrent use in the operational LSST. A separate telescope on the same mountain peak will constantly monitor atmospheric transmission (Stubbs et al., 2007a), and a self-calibrating algorithm applied to celestial standard observations (LSST Science Collaborations et al., 2009) will complement the precision granted by instrumental and atmospheric calibration with accuracy in final reported magnitudes.

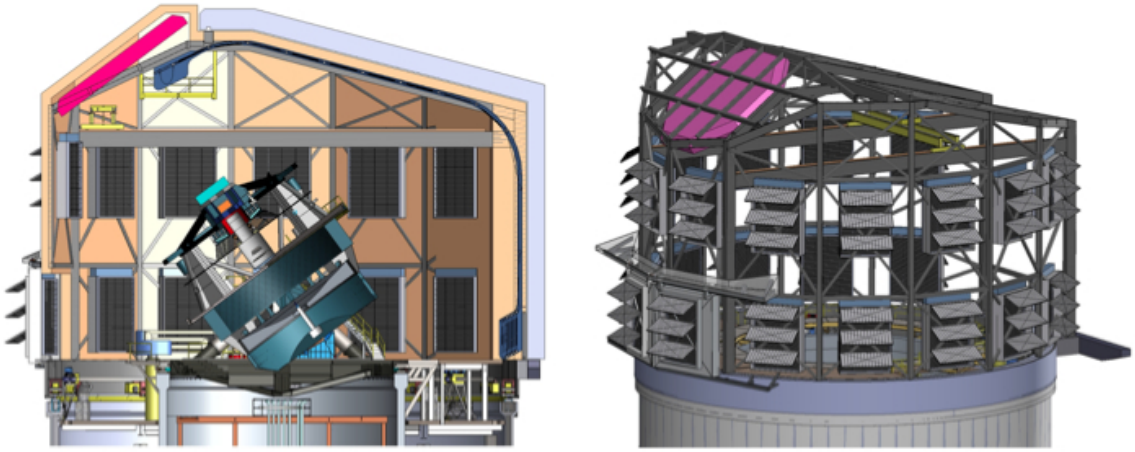

Figure 3-2: A model of the LSST within its enclosure, showing the position of the calibration projector system (pink). Image credit: LSST Corporation.

3.2 Calibration at the LSST: system design

An in-situ calibration system has been designed (Gressler et al., 2010) to satisfy the scientific as well as the engineering constraints of the LSST. It has the following characteristics:

- Like the Blanco and PanSTARRS implementations, the LSST design is intended to allow determination of the response function of the entire optical system as a function of position on the detector, wavelength, and time, relative to a calibrated photodiode.

- Unlike previous incarnations, the LSST design makes an attempt to *limit stray and scattered light* paths by matching the output from the calibration screen to the field of view of the instrument. To accomplish this, the LSST turns from a diffuse screen to an array of "headlamp" projectors.

- Ideally, the LSST system will produce focal-plane illumination that is *uniform* both spatially at a single wavelength, and across wavelengths.

- Finally, because space within the LSST dome is limited, the final system must have a depth of no more than 1 meter.

The baseline design for LSST instrumental calibration comprises an array of 162 individual projectors, each illuminating part of the telescope pupil. Each single projector produces a directed beam of light whose range of output angles is matched to the detector field of view. Together, the projectors in the array will sample the entire surface area of the primary mirror, and the entire optical train thereafter.

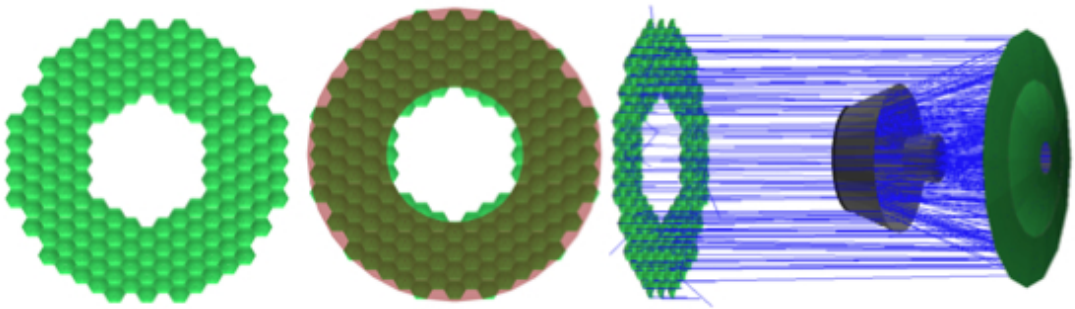

Figure 3-3: The baseline design for the LSST instrumental calibration system comprises an array of 162 individual projectors, whose combined illumination samples the entire primary mirror of the LSST.

Like the implementations at Blanco and PanSTARRS, the proposed LSST system uses a pulsed tunable laser as a monochromatic light source. Photons from an Nd:YAG laser at 1064nm are upconverted to 355nm, then fed through an Optical Parametric Oscillator, allowing for the tuning of monochromatic light over a range of 210nm to 2.3μm. Monochromatic light is then focused into an optical fiber, which in turn feeds the projector array. A

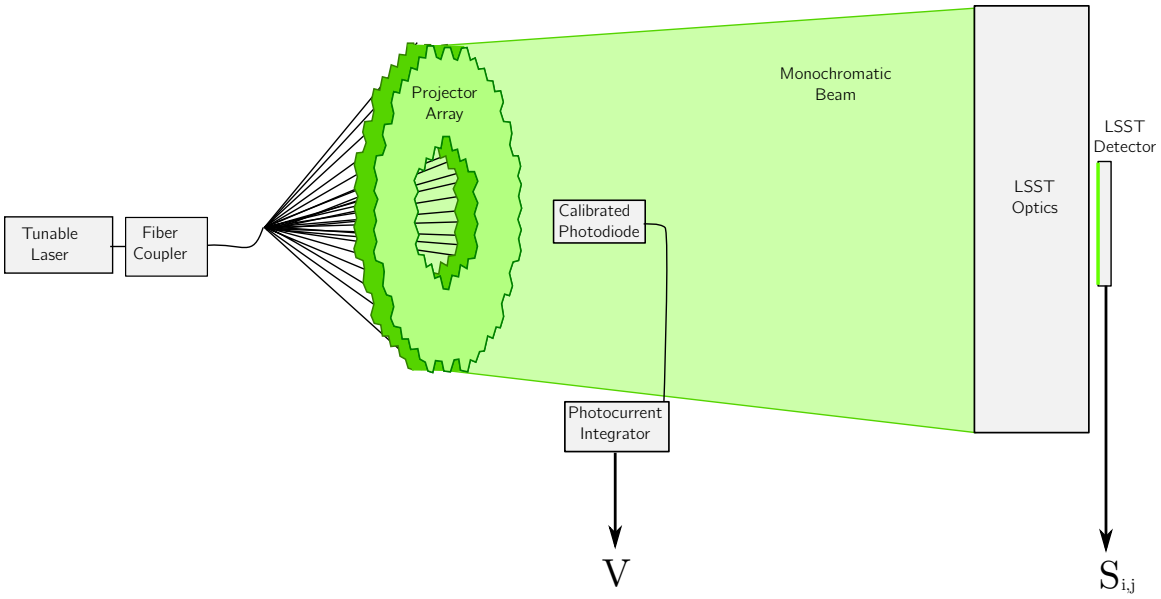

Figure 3-4: Conceptual design of the LSST calibration system. An array of projectors is fed monochromatic light from a tunable laser, and produces a beam constrained in angle that floods the telescope entrance pupil. Light from the projector array simultaneously illuminates a calibrated photodiode. The photodiode itself, with its precisely known quantum efficiency curve, serves as the reference standard for relative flux calibration of the system. As with earlier implementations, simultaneous measurements are taken of the photodiode reading V and the detector response S and pixel (i, j).

calibrated photodiode is placed so as to sample the combined beam of the projector array before it enters the telescope. The monochromatic flux imaged by each pixel of the detector can be compared to that measured by the photodiode to produce a relative value for the response of each pixel versus wavelength and over time. Figure 3-4 illustrates the conceptual layout of the LSST system.

3.3 Single projector requirements and schematic design

This thesis concerns benchtop testing of designs for a single module within the projector array. The objective of a single projector in the array is to convert light from the tunable

laser source into a beam with the particular optical properties required by the LSST design: the light should ideally be *spatially flat* at the focal plane, must be *matched in angle* to the LSST's field-of-view, and must produce a focal plane illumination pattern that is *independent of wavelength*.

3.3.1 Design elements

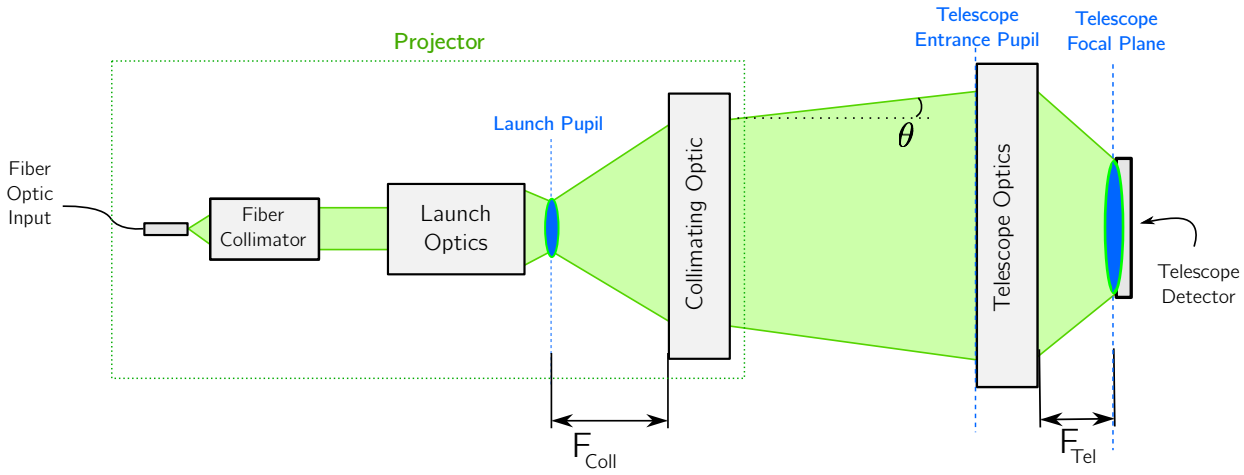

Figure 3-5: Black-box optical design of a single projector. An optical fiber feeds light from the tunable laser through a lens to produce a collimated beam. The *launch optics* turn this collimated beam into a circular, evenly illuminated image at the launch pupil; the pupil is in turn placed at the focus of a *collimating optic*, thereby mapping spatial distribution at the launch pupil into angular distribution at the telescope's entrance pupil. The collimating optic projects a beam whose divergence half-angle θ is a function of the size of the launch pupil image. At the telescope, the angular distribution of this beam is mapped back into position at the focal plane. The end result is to form an image of the launch pupil on the detector, and the spatial and chromatic properties of the 'flat-field' thus created are those of the launch pupil image.

A functional diagram of a single projector is given in Figure 3-5. For clarity of discussion and of analysis, we divide the projector into three functional components:

- **Source and Fiber Collimation**: By "source" we mean the optical train necessary to produce monochromatic light; "fiber collimation" then denotes the means by which the

light is made into a collimated beam. The source optics are common to all projector designs, and the specific scheme we adopt is further discussed in Chapter 4.

- **The Launch Optics**: The purpose of the launch optics is to produce, given a collimated monochromatic beam, an *image* at a predetermined pupil plane. This pupil image must be of finite extent, tolerably uniform in brightness across its surface, and more strictly uniform in pattern from one wavelength to another.

- **The Collimation Optic**: Given a pupil image produced by the launch optics, the collimation optic both collimates that image – produces an image at infinity, to be viewed by the telescope – and matches the projected beam to field of view of the instrument.

Launch optics

The launch optics produce, from a collimated beam, a spatially flat image. The optical setup within the launch optics is comprised of two main elements: first, a diffuser that spreads collimated light into a range of angles; and second, a set of lenses that map that range of angles onto spatial coordinates at the launch pupil.

If we remove the diffuser from the launch optic setup, the entire projector becomes a very straightforward series of elements cycling a single beam through collimation, focusing, and back, as in Figure 3-6.

Ideally, the pattern of irradiance at the focal plane should be independent of the particular irradiance entering the launch optic. Figure 3-7, reproduced from (Gressler et al., 2010), shows a Zemax simulation of desired intensity patterns at the telescope entrance pupil and focal plane. Note that the focal plane pattern is independent of the irradiance on the diffuser.

Collimating optic

The launch optics place an image at the focus of the collimating optic; the collimator, in turn, maps spatial intensity distribution at the launch pupil onto angular intensity distribution at

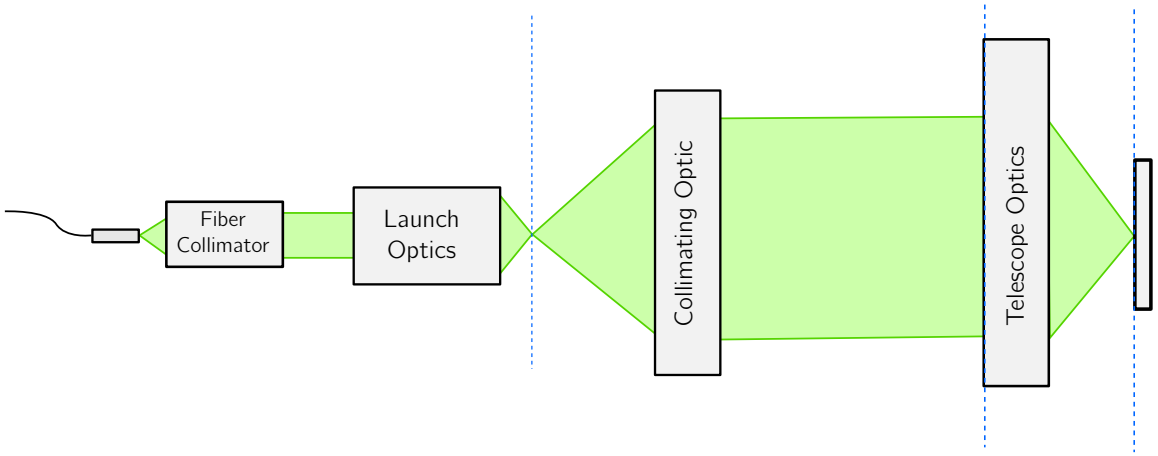

Figure 3-6: Black-box optical design of a single projector *without* its diffusive element, as an illustration of its optical properties. In the absence of a diffuser, the optical system simply maps back and forth between *angles* (the collimated beams) and *positions* (the focused points).

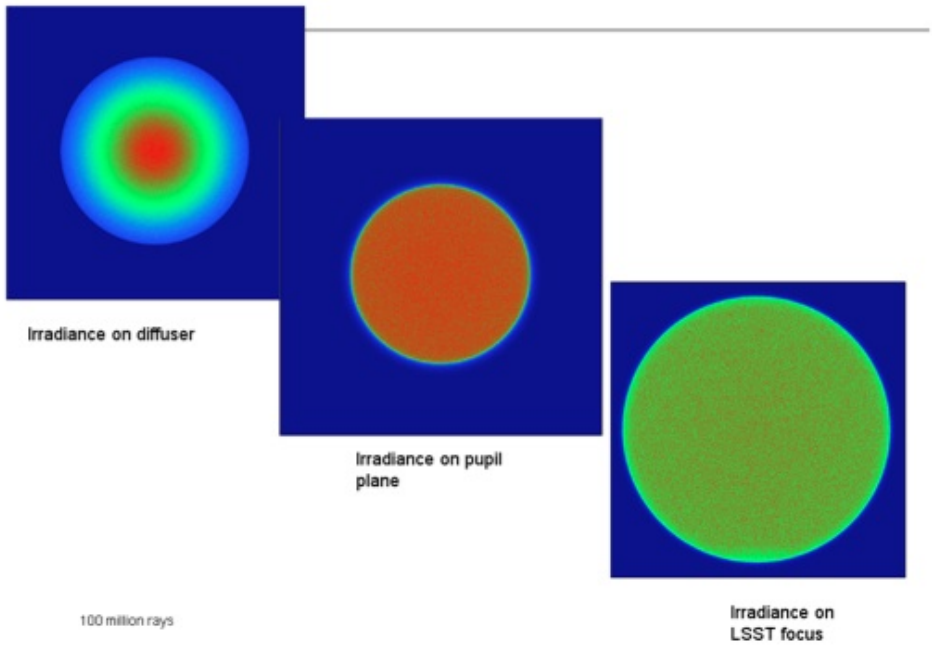

Figure 3-7: Zemax model of desired illumination patterns at the telescope pupil and at the LSST focal plane. Figure from (Gressler et al., 2010).

the telescope's entrance pupil. In practice, there are two general categories of the collimating optic: reflective or transmissive. The relative benefits of each will be addressed in more detail in Chapter 6. For now, we note that although the choice of collimating optic impacts the setup of the projector – Figure 3-8 shows a schematic of each – the optical properties remain the same.

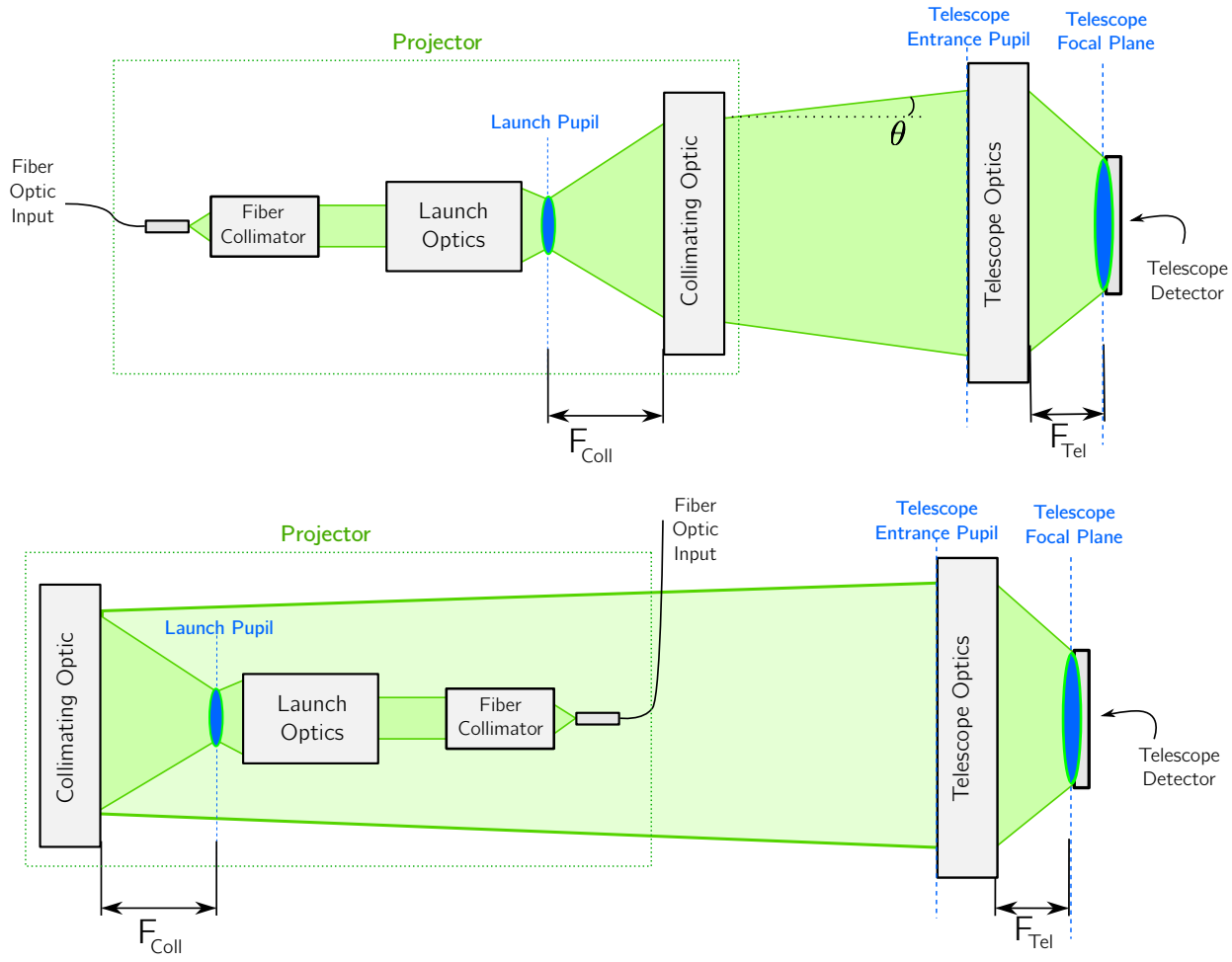

Figure 3-8: Comparison of projector designs using transmissive (top) and reflective (bottom) collimating optics. The optical principles of the projector system are the same in each case.

Chapter 4

Optical Testing Methodology for Single Projector Prototype

Laboratory testing of projector prototypes, and of the elements that comprise each projector, cannot be done on the LSST itself – not least because the telescope has yet to be built. Instead, we have constructed a testbench system to serve as a surrogate. We have designed this system to parallel the LSST in its optical function: in light source, telescope and camera optics, and detector.

4.1 Light source: range and monochromaticity

The LSST design calls for each projector to be fed by monochromatic light through an optical fiber. In the final implementation, the source of this light will be a tunable laser. The laser produces light with the following features:

- **Range:** An Ekspla laser can be tuned to produce light anywhere between 210 and 2600nm. Although optical fiber transmission in the UV is low, the available wavelengths more than span the LSST's range of 320 to 1080nm.
- **Monochromaticity:** The tunable laser produces highly monochromatic light: the model planned for use at the LSST has a spectral breadth on the order of 0.1 - 0.5nm

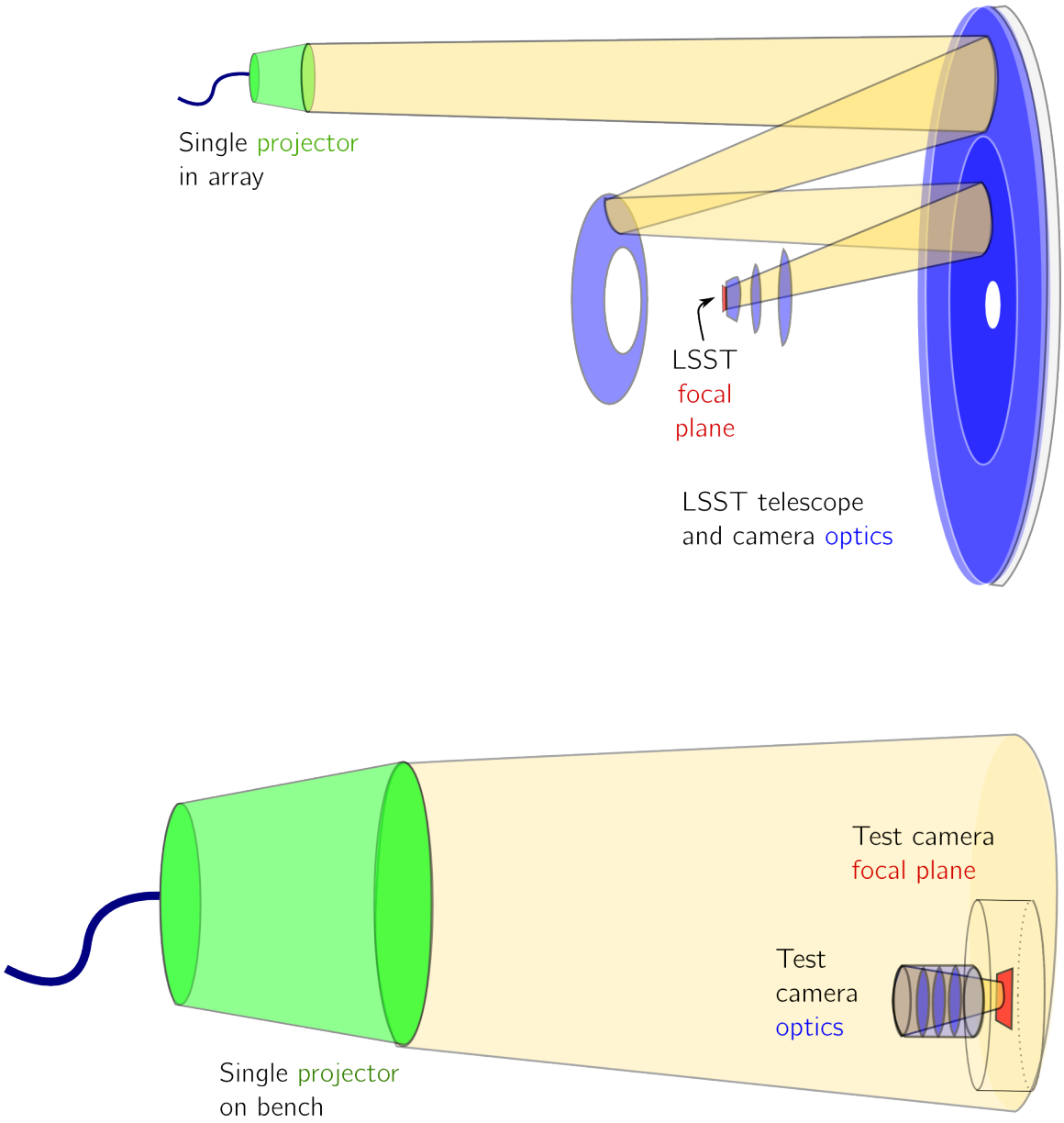

Figure 4-1: Functional diagram of a representative projector in the LSST system (top) as compared to the benchtop setup (bottom)

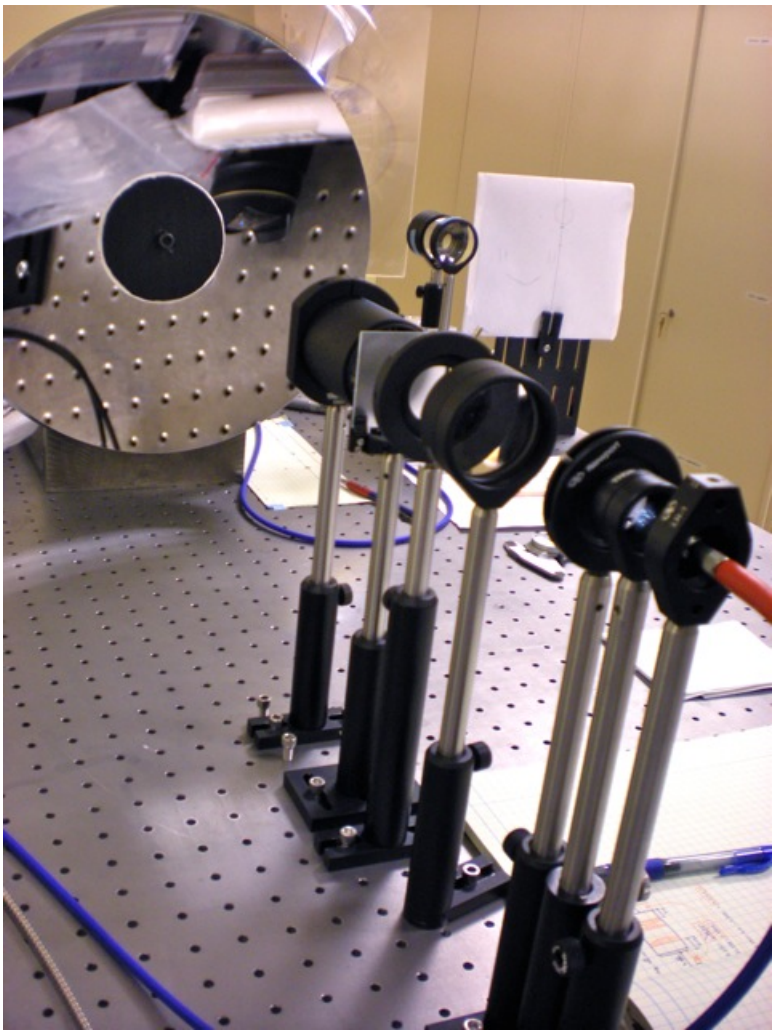

Figure 4-2: Photo of a representative projector prototype on the optical bench. Mounted elements from right to left include source fiber, neutral density filter, variable iris, achromatic doublet, iris, Engineered Diffuser, three-lens relay, and parabolic mirror.

(Stubbs et al., 2010).

- **Short coherence length** The Ekspla is a pulsed laser with 5nsec pulse times. Such a short pulse length implies a correspondingly short *coherence length* – because the pulses are so short, waves can only remain "in step" for so long before the pulse decays. The short coherence length, in turn, avoids the issue of laser speckle – self-interference effects possible when the path-length differences in a system are within the source's coherence length. Interference patterns can quickly turn flat illumination into a tangle of light and dark fringes, with exactly the kind of amplitude variation we seek to avoid.

The light source on our testbench needs to adequately represent the LSST source with regard to the same criteria: it must sample the LSST's range, be monochromatic, and avoid speckle effects.

As a primary broadband light source, we used a tungsten halogen lamp housed in a fiber illuminator. The halogen bulb is by nature an incoherent source, so no speckle effects are present. The bulb has a quartz envelope, allowing some transmission of near-UV light that would be blocked by glass. In practice, even with the quartz envelope, the source was very weak below 400nm. It did produce ample light in the visible and near infrared.

The broadband source was band-limited by either a Newport 74055 monochromator, or by narrow bandpass filters. The monochromator uses a reflective grating to disperse broadband light, and a slit to select a narrow wavelength range. Light within the monochromator, though, is dispersed into multiple orders, which leads to two problems. First, the monochromator is inefficient because light at a given wavelength is distributed among many orders, but only sampled at one. Second, there is overlap between orders such that when the monochromator is set to light at wavelength λ, some light at $\lambda/2$ is also selected. An order-blocking filter – a longpass filter that imposes a lower bound on wavelengths transmitted – must be used for wavelengths above 600nm, but removed below. The extra filter creates an asymmetry in the optical train between, for instance, data taken at 500nm and at 700nm. For data taken with the monochromator, we used an Edmund Optics 600nm longpass filter.

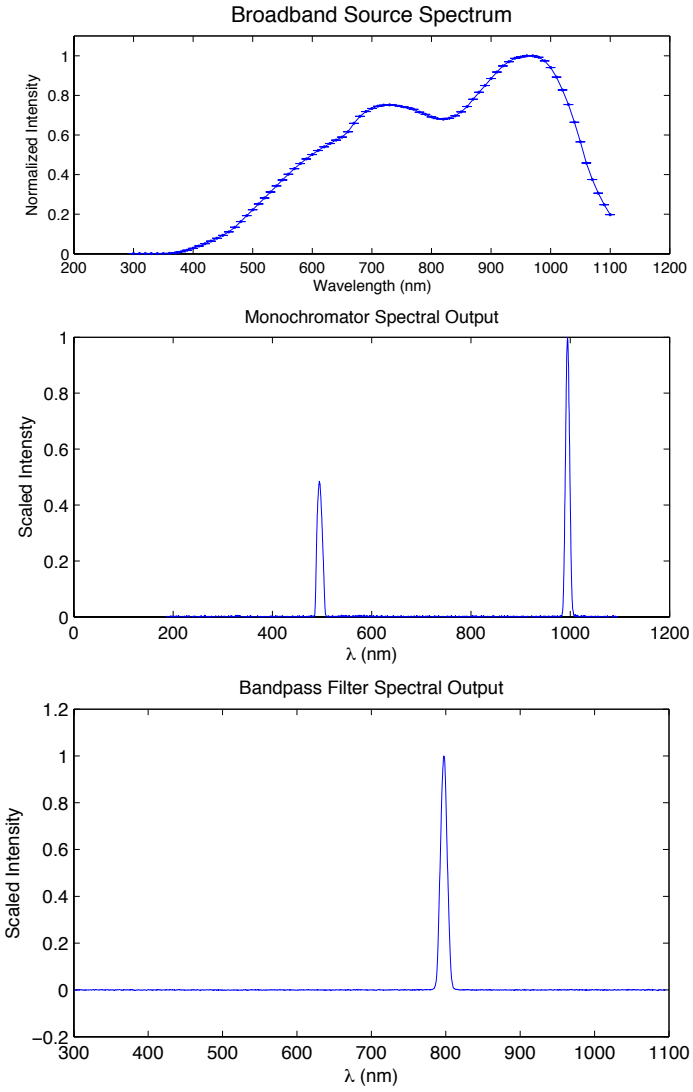

Figure 4-3: Spectra of various light sources illustrating their range and monochromaticity. Top: spectrum of tungsten halogen "white" light source. The steep falloff above 1000nm is most likely an artifact of spectrograph detector quantum efficiency, rather than a true indication of available light. Center: the spectrum of a white light source through a monochromator with 5-mm output slit with no order-blocking filter in place. The monochromator was set to 1000nm; note the peak at 500nm, corresponding to order overlap. Bottom: the spectrum of a white light source through a 10-nm FWHM bandpass filter.

In order to get appreciable light from the monochromator through the projector system, we used the widest available slit (5mm). The tradeoff for the wide slit is correspondingly wider linewidths: "monochromatic" light in fact had a full-width at half-max (FWHM) of 10nm.

Narrow bandpass filters can also produce light that is monochromatic at the 10nm FWHM level, and can do so with much improved efficiency. Bandpass filters work by thin-film interference, rather than by dispersion. Consequently, they lose no light to multiple dispersive orders, nor do they require order-blocking optics. A set of bandpass filters spanning the range of available wavelengths allowed us to gauge chromatic variation across the wavelength range. Bandpass filters sample a discrete selection of wavelengths, one per filter. Unlike the monochromator, they cannot make a continuous scan across the wavelength range. Nevertheless, since we are only looking to probe variation across the range, we decided that the bandpass filters would suffice. The bandpass filters were, in all cases, inserted into the optical train before light hit any element of the projector itself. In later trials, so as to most effectively limit any reflection artifacts, they were inserted into a filter slide built into the fiber illuminator.

Calibration and throughput of the monochromator and bandpass filters were verified using an Ocean Optics HR-2000 spectrometer, which was in turn wavelength-calibrated to the emission lines of a HgAr lamp. Figure 4-3 presents representative spectra illustrating broadband and monochromatic properties of the light source.

4.2 Simulating the LSST optical train

The optical train of the LSST is complex. Light entering the telescope must reflect off of the primary, secondary, and tertiary mirrors, pass through the a set of refractive corrector lenses as well as one of the LSST broadband filters, and finally hit a CCD detector at the focal plane. But despite this complexity, the LSST's main optical objective is straightforward: to bring an image of an infinitely distant point source to a focus at the plane of the detector. Building an optically congruent system on the bench is as straightforward as obtaining a

suitable camera and focusing it at infinity.

We used a small astronomical camera, the Santa Barbara Instruments Group 10XME, which is equipped with a 3.2 megapixel CCD detector measuring 10mm by 14.9mm. The detector was thermoelectrically cooled to between -10 and -15 C in order to limit dark current.

The LSST has a field of view whose diameter is limited to 3.5 degrees of arc. When designing its benchtop surrogate, we opted to construct a slightly larger field of view. The extra area around the edges allowed us to evaluate the presence and magnitude of what would, in the LSST, be non-focusing light paths. To that end, we equipped the SBIG camera with a 105mm Nikon lens, which yielded a field of view of approximately 5.2 by 7.8 degrees.

Every detector has an intrinsic quantum efficiency (QE) defined as the ratio of incident photons to detected photoelectrons at a given wavelength. We measured the wavelength-relative QE of the combined detector-plus-lens system using a large integrating sphere. We placed the end of the lens at one of the sphere's output ports and fed monochromatic light into the sphere, then made simultaneous measurements of the total flux incident on the detector and the power incident on a sphere-mounted photodiode. A diagram of the setup and the resulting QE curve are presented in Figure 4-5. The QE has been scaled relative to its peak at 600nm. The measured curve makes it evident that the efficiency of the camera-plus-lens system drops dramatically at longer wavelengths. Above 1000nm, data collection becomes difficult to the point of impracticality.

We expect the test camera CCD itself to be subject to the same principles of pixel-to-pixel and color-to-color variation as the LSST detector. In order to minimize uncertainty introduced by the test camera, we performed flatfield calibration using the same integrating sphere setup as above. A stack of 3 to 10 flat fields were taken at each wavelength between 400nm and 1000nm, in 50-nm increments, using the monochromator with wide slit as the input source. At each wavelength, flat fields were median combined into a single master flat, which we used to reduce all subsequent data taken at that wavelength.

Finally, in accordance with the principles of telescope optics, we focused the lens at infinity.

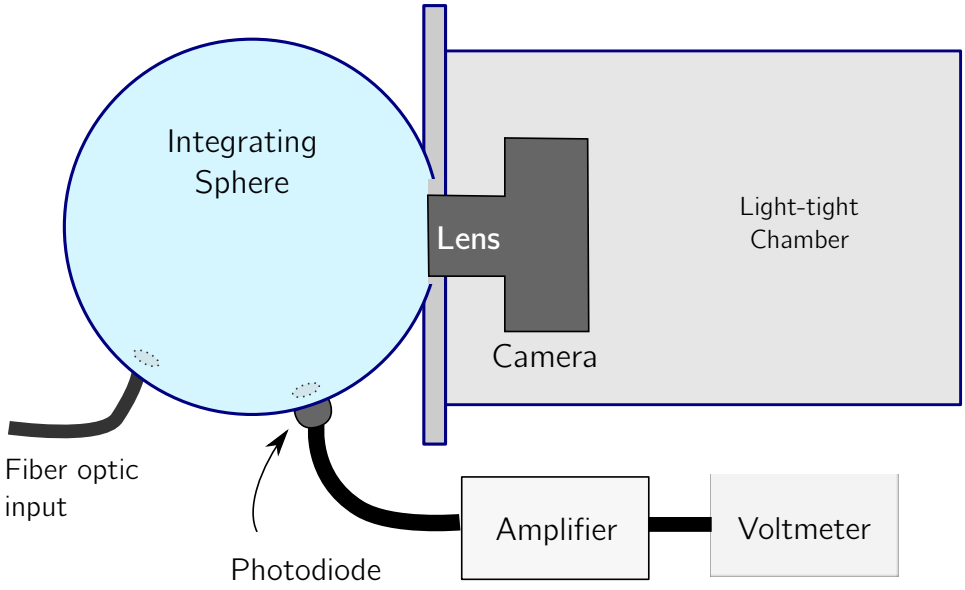

Figure 4-4: Schematic of quantum efficiency and flat-field calibration procedure for the test camera.

4.3 Focus, alignment, and collimation procedures

The Nikon lens we used did have focus positions marked; however, because we used a mount adapter to affix the lens to the SBIG body, we determined focus positions optically. To do so, we placed an object – usually a US Air Force test plate – at the focus of a lens, creating an image of the plate at infinity. The camera was then pointed through the lens, and its focus adjusted manually until the image was sharpest. A schematic of the procedure is given in Figure 4-6.

Alignment of the optical elements comprising the launch and collimation optics was important both in reducing stray light and in avoiding aberrations and edge effects in the lenses. In all diffuser setups, optics were first aligned without the diffuser, and the diffuser was added only later. Without the diffuser, the behavior of many of the systems could be

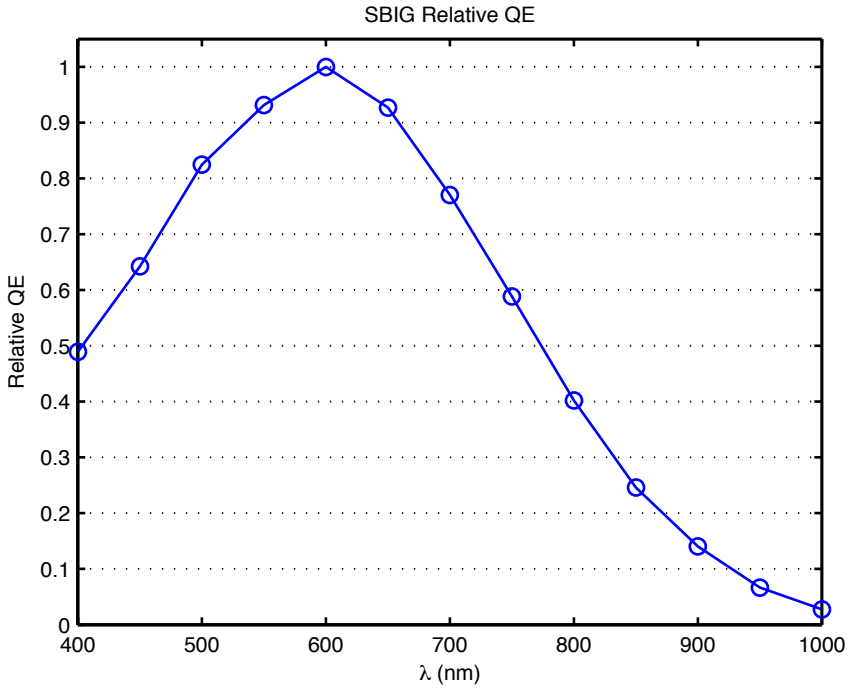

Figure 4-5: Quantum efficiency of the SBIG camera with Nikon lens, as measured relative to a calibrated photodiode.

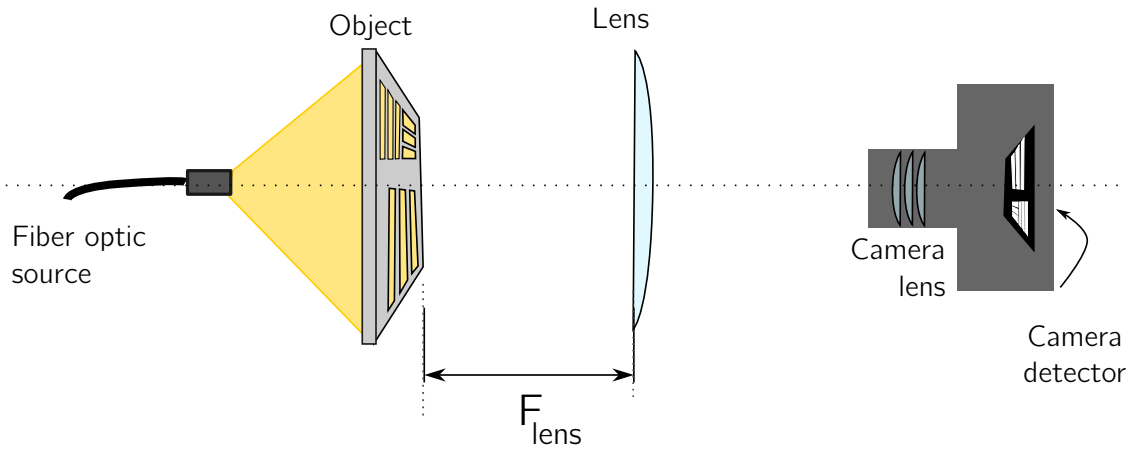

Figure 4-6: Schematic of camera focusing at infinity. An object, illuminated either in reflection or, as here, in transmission, was placed at the focus of a lens to create an image at infinity. The test camera lens was then adjusted to produce the sharpest possible image on the detector.

reduced to a series of either collimated beams, or beams which were to come to a focus at a specified point. Both conditions are easily verified optically. Once alignment had been checked, the diffuser was added.

All Engineered Diffusers are specified for use with a collimated incident beam. Light exiting an optical fiber is, of course, not collimated. We collimated the beam using an achromatic doublet lens. The fiber aperture was placed at the focus of the achromat, where it would yield a collimated beam on the other side. We verified the fiber positioning, and thus the collimation of the beam, by retroreflecting the collimated beam through the achromat using a small flat mirror. A well-collimated beam will produce a point-source image in the plane of the original source. Figure 4-7 illustrates this procedure.

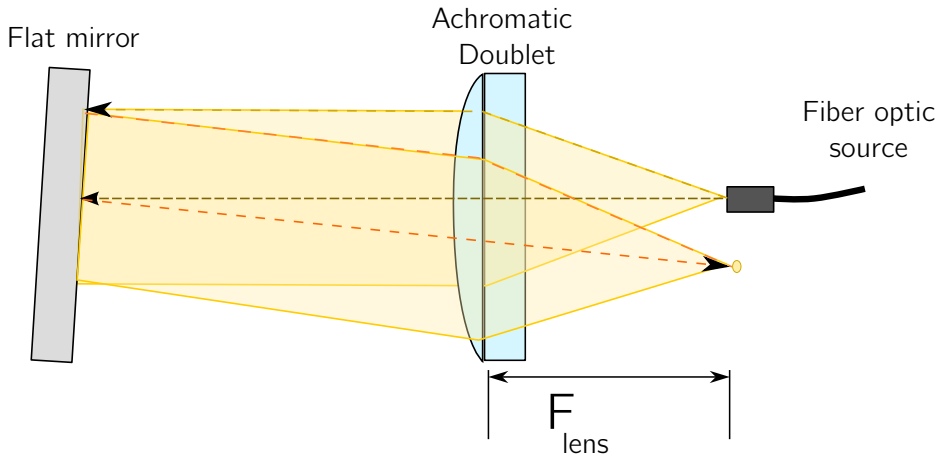

Figure 4-7: Diagram illustrating beam collimation procedure. The aperture of the fiber optic was placed at the focus of an achromatic doublet lens. The resulting collimated beam was retroreflected back through the achromat by a flat mirror. Symmetry in optical systems demands that a collimated beam retroreflect to produce an image of the original aperture in the same plane as the source.

4.4 Stray light control

One of the objectives of the projector method of flatfielding is the reduction of systematic error introduced by stray or scattered light – that is, by focal-plane detection of photons

that were not, when they entered the telescope pupil, on focusing light paths. We made some effort to minimize stray light from optical elements in the testing setup:

- All spherical lenses used in beam collimation and in relay optics were coated with a broadband antireflective coating to minimize reflections.
- Baffles in the form of adjustable irises were placed in the optical train at points where light might otherwise overfill an element, or produce unwanted scatter: between the fiber and the achromatic doublet, for instance. The position of these irises is indicated in the schematic drawings for each setup tested.
- The irises themselves are matte black elements.
- The computer running the data acquisition software was placed behind a wall and was facing away from the camera and optics, to minimize ambient light and unwanted reflections arising from its screen.

4.5 Data acquisition, reduction, and analysis methodology

4.5.1 Data acquisition and reduction

With the test bench set up as outlined above, we acquired data for each element and prototype under investigation. Each round of data acquisition included a series of checks: verification of alignment; of camera focus; of CCD temperature; of stray light in the lab; and of camera position. The camera was rotated as necessary to center the data on the CCD, to minimize any edge effects or vignetting.

Each data image was taken as a double exposure using SBIG's CCDOps software: first a combined dark and bias frame, then a data frame. The dark/bias frame, which measures the detector's dark current and readout noise, was automatically subtracted upon readout and

display. Data images were reduced by subtracting the master flatfield at the corresponding wavelength.

4.5.2 Data analysis

Because the test camera is engineered to serve as the LSST's optical surrogate, what we image on the testbed detector is what would be seen at the LSST focal plane, but with the extra area granted by our wider field of view. We judge each data image according to how well it satisfies the projector criteria laid out in Chapter 3:

- **Defined angular range**: The image should be circular, symmetric, and have a sharp cutoff at the edges. There should be minimal light outside the circle.
- **Spatial Uniformity**: A flat image will show minimal variation in brightness at either high or low spatial frequency, nor will it have evidence of non-random structure.
- **Chromatic Uniformity**: The illumination pattern, extent, and flatness of the image should not vary with wavelength.

The ideal projector, imaged by the test camera, would produce a circle of perfectly even illumination, identical at every wavelength, with only darkness beyond.

In the chapters that follow, each set of data is presented both as reduced images and as one-dimensional plots made by averaging a ten-pixel horizontal slice across the data circle. The images allow for visual inspection of radially symmetric structure, while the plots give a quantitative measure of any variation or aberration present. A sample data image and plot are shown in Figure 4-8, with relevant features – things to look for – highlighted.

To quantify the performance of each element and projector system according to the parameters specified above, we applied statistical analysis to the data images.

Stray light

In measuring stray light, we considered, in a one-dimensional profile of the data image, both the sharpness of the cutoff and the ratio between counts within the projected area to those

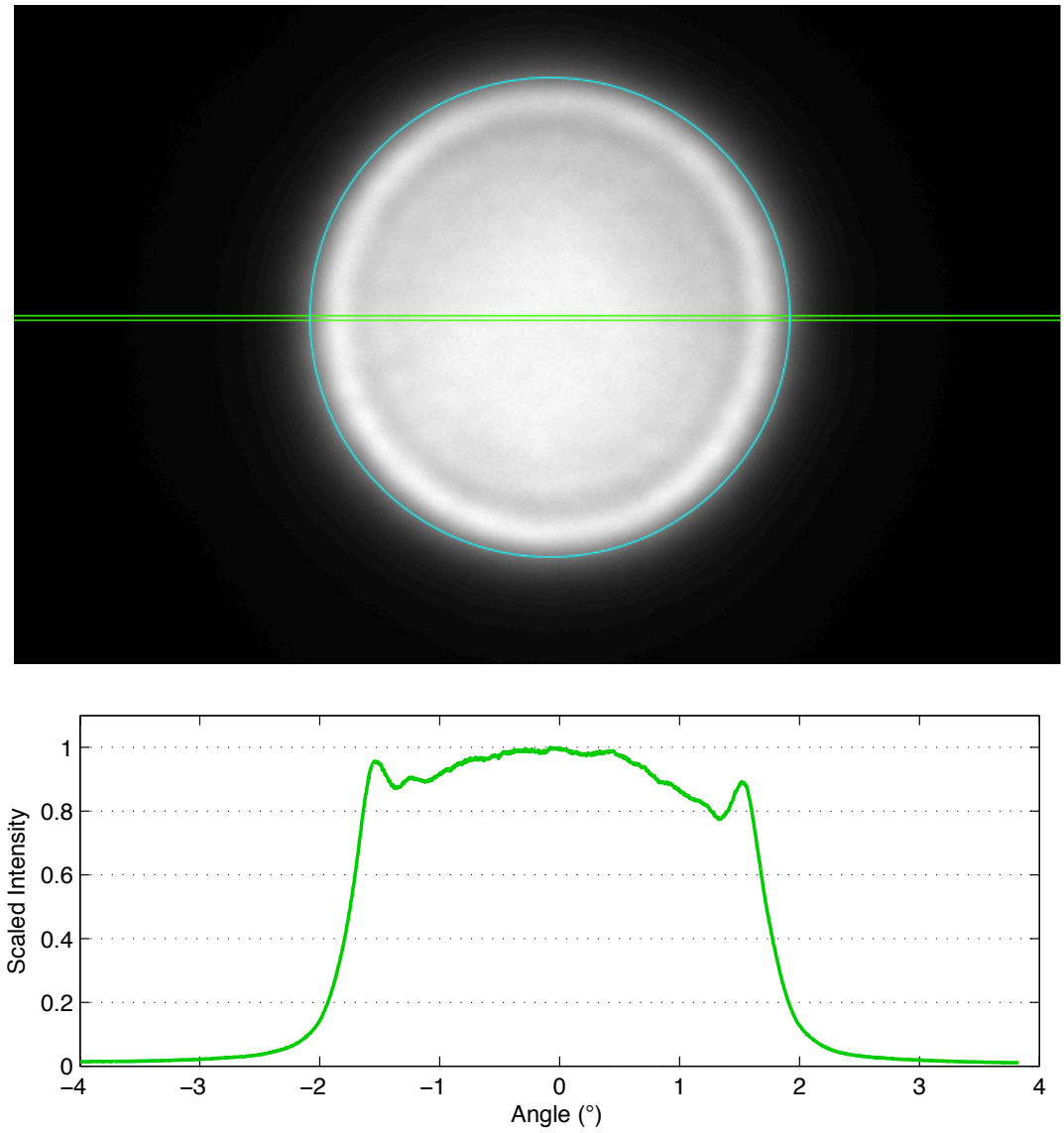

Figure 4-8: Sample data image and one-dimensional plot, with relevant features highlighed. The blue circle overlaid on the data image shows the limits of the LSST's 3.5° field of view; the green line across the center denotes the ten-pixel strip that was averaged to produce the one-dimensional profile.

without. Because stray light control in the lab was not absolute, numbers given for stray light should be taken as conservative estimates of projector behavior rather than as ideal system performance.

Spatial and chromatic uniformity

We quantified spatial uniformity by examining a series of concentric circular regions in each reduced data image. Within each circle, we calculated the "flatness" by measuring, for counts at each pixel within that circle, the standard deviation divided by the mean (σ/μ), expressed as a percentage. With this data we can say, for instance, that a particular image showed uniformity at the 5% level within the central 0.5 degrees, but only at 10% within a 1.5 degree circle.

To measure uniformity across wavelengths, we divided two images taken using the same setup but at different wavelengths. If the illumination pattern were achromatic, we would expect the ratio of two images to be constant within the projected circle. We quantify chromatic non-uniformity as variation from flatness in the divided images, and we calculate, for each divided frame, σ/μ as above.

4.6 Limitations of testing methodology

Our testing results are estimates of projector behavior, and are subject to the limitations of testing methodology. Here we note a few of the limitations and potential sources of error in our testing setup.

The test camera system was not a perfect match for the LSST. Because the light source was faint in the blue, and because the CCD QE was low in the red, we restricted the vast majority of test data to wavelengths between 400 and 1000nm. This range does not quite extend to the edges of the LSST's 320-1080nm band, but does allow us to sample colors across the central 80% of the range. Even the narrower range suffices, though, to allow us to test the concepts behind each projector, and to eliminate those options that are clearly infeasible.

Perfect stray light control in the lab was not achieved. Light sources included the computer running the tests, light leak from the fiber illuminator, and light from indicators on other instrumentation in the shared space. We can quantify the effect of this stray light by examining "ambient" images, taken by closing the shutter on the fiber illuminator but leaving the setup otherwise untouched. Figure 4-9 shows a side-by-side example of a data frame and its corresponding ambient image. Maximum counts in the ambient image are on the order of 200; the illuminated data pixels are on the order of 20000: ambient light in this case introduces a systematic uncertainty of 1%.

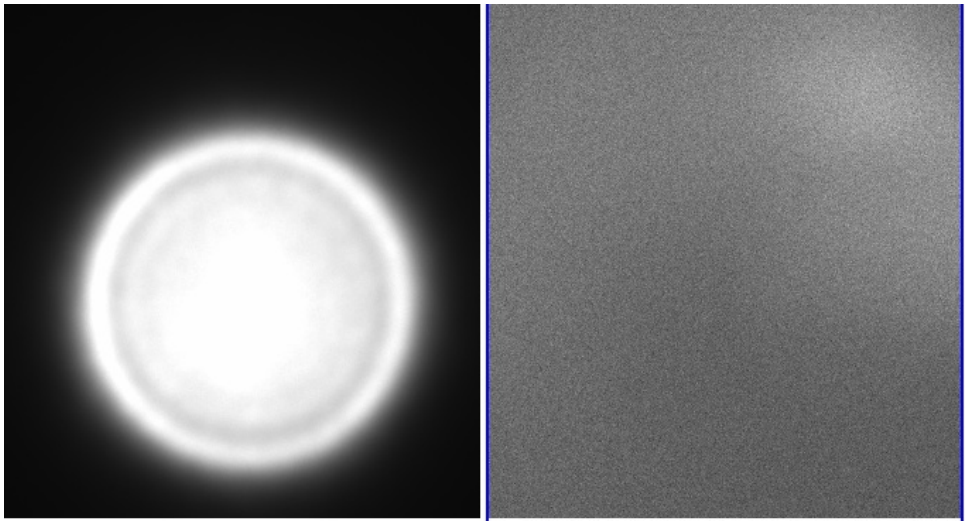

Figure 4-9: Side-by-side comparison of a data image (left) and the ambient light image (right) taken immediately afterwards. In the ambient light setup, the shutter on the monochromatic source has been closed, so that no light is fed into the optical train. Maximum count levels in the ambient image are on the order of 1% of those in the data frame.

Because the beam produced by each projector is much wider than the test camera's lens, not all of the beam could be sampled at once. In relevant cases, we sampled the projector beam by translating the test camera.

Finally, the cost of simplifying the LSST's optical train to a small camera lens is increased optical aberration. The Nikon lens we used was not, itself, perfectly achromatic. In each case, we focused the Nikon lens at infinity as gauged by the sharpest image produced at 550nm.

The chapters that follow present the results from laboratory tests first on the individual components proposed for use as launch (Chapter 5) and for collimating (Chapter 6) optics, and then on prototypes of the full projector (Chapter 7).

Chapter 5

Analysis of Launch Optics

The purpose of the calibration projector as a whole is to produce an achromatic beam whose rays span a range of solid angles matching the LSST field of view, and which has equal energy in each unit of solid angle within that range. Within that projector, the launch optic takes as input collimated monochromatic light – monochromatic from the source; collimated as outlined in Section 4.3, by an achromatic doublet – and outputs an angularly flat diverging beam. In order to satisfy our requirements, the launch optic must first prove capable of this kind of angular radiance. Then we must show that the pattern of light it produces does not vary with color across the range of testable wavelengths.

5.1 Engineered Diffusers

The diffusive element used as launch optic in most of the projector designs is an Engineered Diffuser^{TM}(ED) made by RPC Photonics. The ED is fabricated as an array of microlens structures on a flat, transparent substrate. In essence, it is a beam shaper: it spreads a collimated beam into a tightly specified range of angles.

An Engineered Diffuser is specified by its substrate materal, glass or film; its physical size; and by the shape and angular dispersion of light. The manufacturer's convention is to give angular dispersion as full angle at 90% maximum intensity – analogous to the FWHM used

for spectral lines – and I have retained that convention here. Thus when I write "30-degree ED", I mean one which sends light from every point on its surface into an angular range of plus or minus 15 degrees from the optical axis. The EDs I have tested are manufactured on glass, are 2" square, and have been designed to spread light evenly into a specified cone of angles, so that the illumination pattern they produce is circular. A photo of a representative ED mounted in a filter holder – this one is a 2" square, glass, 30-degree circular diffuser – is shown in Figure 5-1.

Figure 5-1: Photo of a 30-degree circular Engineered Diffuser on a glass substrate.

The defining characteristic of the Engineered Diffuser is its ability to take as input a collimated beam, and output a beam whose angular radiance is tightly defined. EDs designed to produce a flat circle of light are often called "top hat" diffusers: the ideal three-dimensional surface plot of intensity versus scatter angle would look very much like a top hat. A one-dimensional plot of ideal setup and performance is shown in Figure 5-2, with a demonstrative photo of the ED in action in Figure 5-3. Note that the helium-neon laser shown in the photo

is used for illustration only – its coherence length is too long, and laser speckle consequently too prevalent, for use in testing.

The ideal tophat Engineered Diffuser minimizes stray and scattered light, because its range of output angles is limited. It produces a flat illumination pattern. If patterned on an appropriate substrate, the ED can easily transmit light over the required wavelength range. The ideal characteristics of the ED, then, seem promising.

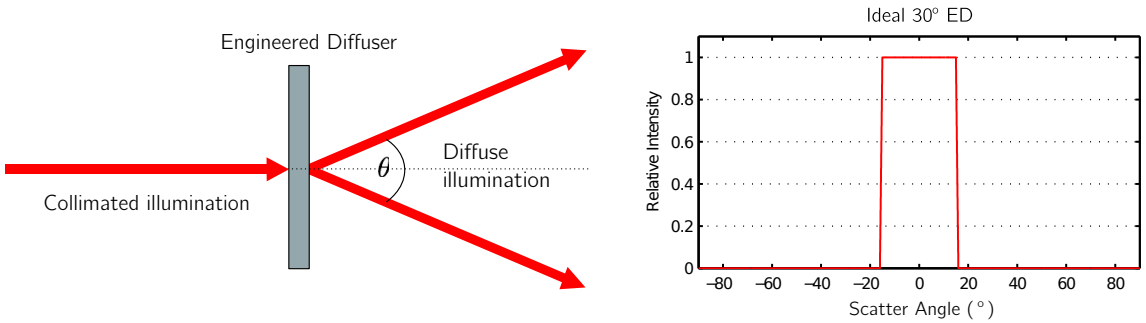

Figure 5-2: Optical properties of an ideal Engineered Diffuser. Left: the ED transforms incident collimated light into a diffuse beam with a sharply defined angular spread. Right: Ideal profile of angular scatter in the beam produced by a 30° ED. Diagrams after those published by RPC Photonics (cite website).

5.2 Measured behavior of the 4° and 30° Engineered Diffusers

A first set of measurements was taken of 4° and 30° circular tophat EDs. The diffusers are off-the-shelf components two inches square, and are replicated on glass substrates. The 4° diffuser's output was measured by simply illuminating the diffuser with a collimated monochromatic beam, and imaging the resulting light with the test camera focused at infinity; because the 30° output was wider than the Nikon lens's field of view, we instead measured it by sweeping a photodiode through its range of scatter angles.

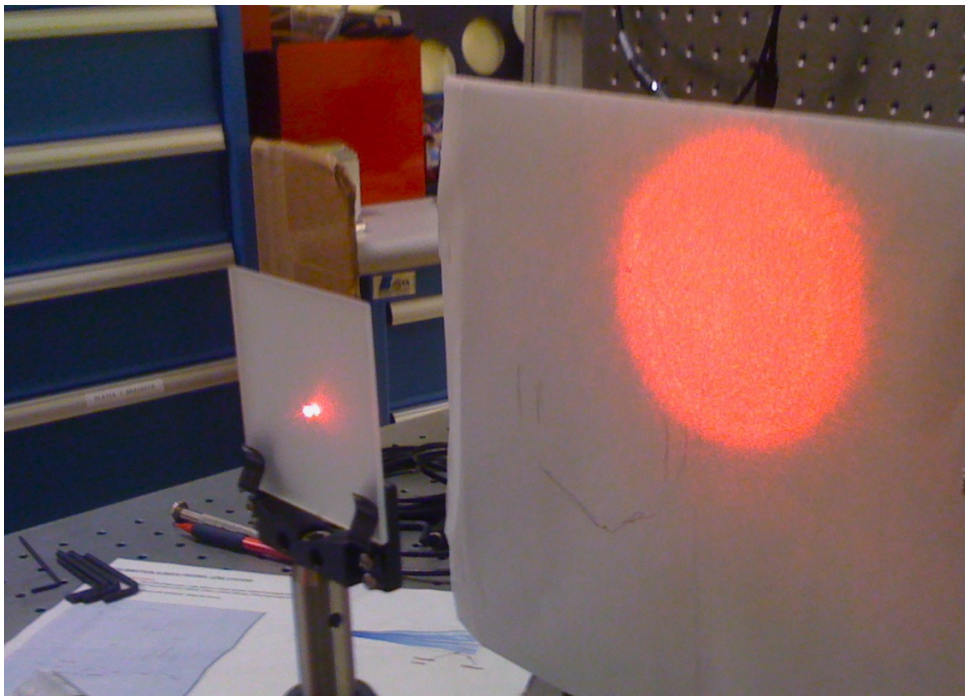

Figure 5-3: Photo of a 30° Engineered Diffuser illuminated with a helium-neon laser. Note that the helium-neon laser shown is used for illustration only – it is unsuitable for testing due to its long coherence length and consequent speckle effects.

5.2.1 Stray light control

Both the 4° and 30° EDs were efficient at minimizing stray and scattered light. Figure 5-4 shows a sample one-dimensional profile of a 4° Engineered Diffuser illuminated with 500nm light, compared to the Lambertian profile of a typical reflective screen. For the 4-degree diffuser, the 90%-to-10% fall distance, as measured in degrees from the center of the projected beam, was 0.5°. The fractional intensity of counts well outside the projected beam – further than 2.5° from the center of the bright region – was on the order of 2%-5%.

5.2.2 Spatial uniformity

We found that, although both EDs are a tophat-type diffusers, their profiles are not perfectly uniform. As measured at the detector, both ED produced brighter and dimmer regions with peak-to-peak variation on the order of 10 to 20%. We ran several tests to determine which

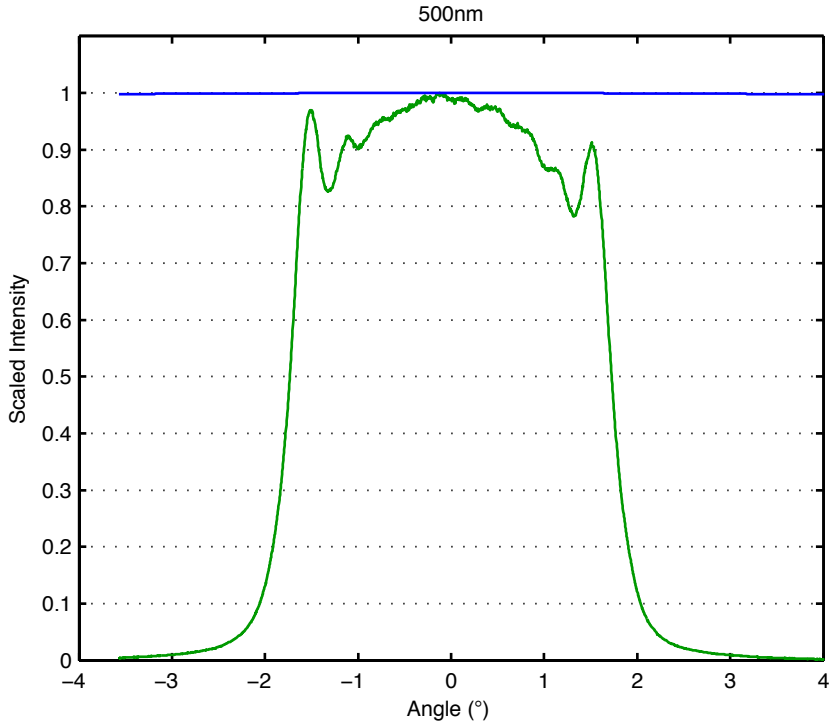

Figure 5-4: One-dimensional angular profile of 4-degree Engineered Diffuser illuminated with collimated monochromatic light at 500nm. Green data in the plot indicates 4-degree diffuser data; for comparison, a Lambertian cosine profile is plotted in blue. On the scale plotted here, the Lambertian profile is nearly flat: Lambertian screens scatter light much more widely and do not control stray light. By contrast, the ED constrains its angular output.

elements of the observed brightness variation might be random, and which persistent.

First, to establish that variation at this scale was not due to the light source or to any time-dependent factor in the setup, we took a sequence of control images using the 4° at 400nm without altering the setup in any way. We then took a sequence of images with the same diffuser and wavelength, this time translating the diffuser perpendicular to the optical axis, so that each image was made with the collimated beam striking a different area on the diffuser's surface. Results from these tests are shown in Figure 5-6. The first series establishes that the brightness variation in the diffuser profile is time-invariant: the magnitude of variation in the diffuser profiles is only what we might expect for variation in the camera readout noise. The second series of images establishes that the pattern of

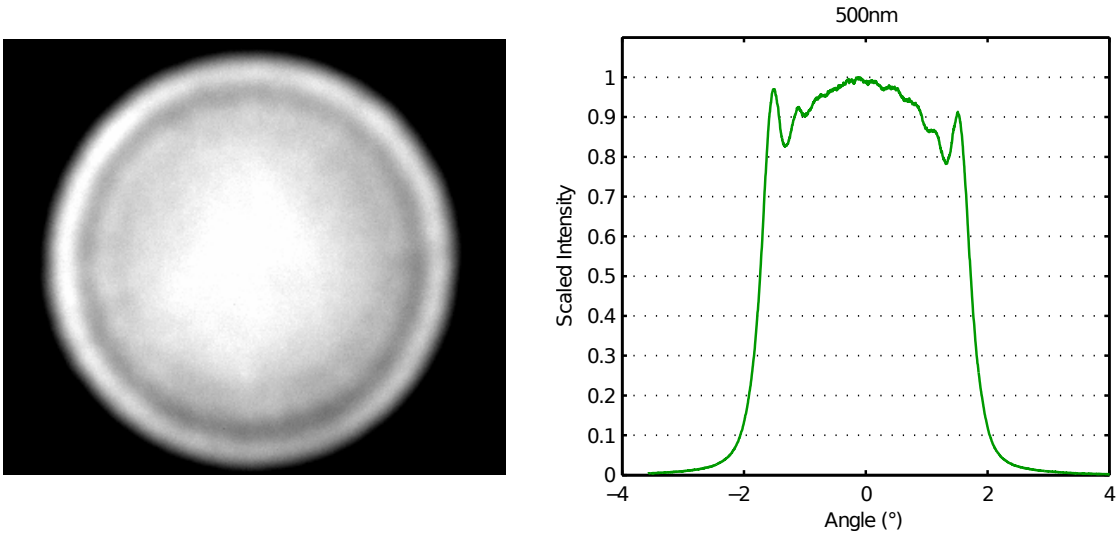

Figure 5-5: Data image and angular profile for a 4-degree top-hat Engineered Diffuser as measured on the lab bench.

brightness variation at high spatial frequency is dependent on diffuser position, and that high-frequency variation can therefore be averaged out – but nevertheless, a characteristic shape remains at the detector plane. This particular ED produces not a perfect top-hat, but something more like a fedora: a central dome or peak, and a bright outer ring.

To make sure that the radially symmetric structure evident in the 4° ED measurements was no artifact of my circular Nikon lens, we measured the 30° ED profiles with a completely different setup. Instead of imaging with the camera, we mounted a photodiode on an arm affixed to a motorized rotary stage, centered the rotation of the axis of the stage under a diffuser, and swept the photodiode in an arc through the desired range of angles. A diagram of this setup and a comparison of profiles made using the two methods are shown in Figure 5-7. Although variation in the 4° diffuser is more pronounced, the consistent overall shape between profiles made with photodiode and camera, two completely different setups, indicates that the shape itself is not an artifact of measurement methodology.

Finally, we attempted to determine whether the ring structure might be specific to one of the parameters in the testbench setup. We compared diffusers specified for different angular ranges; we varied the diameter of the collimated beam incident on the ED; we moved the

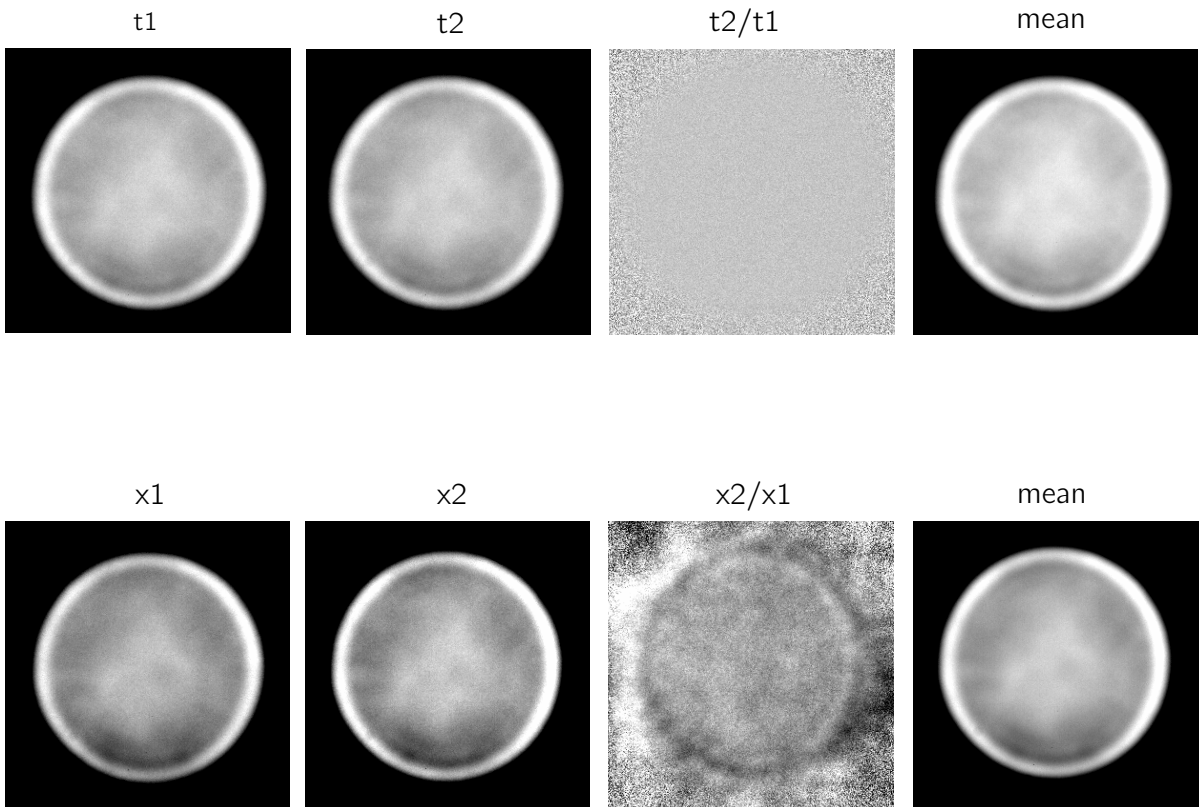

Figure 5-6: Time and position dependence of 4° ED output. Top: a series of 400nm images taken sequentially without altering the setup. Of the ten images taken, two are shown above (t1 and t2); a ratio of the two (t2/t1) is very flat, indicating minimal time variation; and an average of all ten images is not markedly smoother. Bottom: a series of 400nm images taken with the collimated beam illuminating different areas of the 4° diffuser surface. Again, two representative images are shown (x1 and x2), and there is some visible change in high-frequency pattern between them; a ratio of the two (x2/x1) clearly shows high-frequency variation; the average of ten images is smoother at high spatial frequency than either of the individual images, but retains the larger-scale central dome and outer ring.

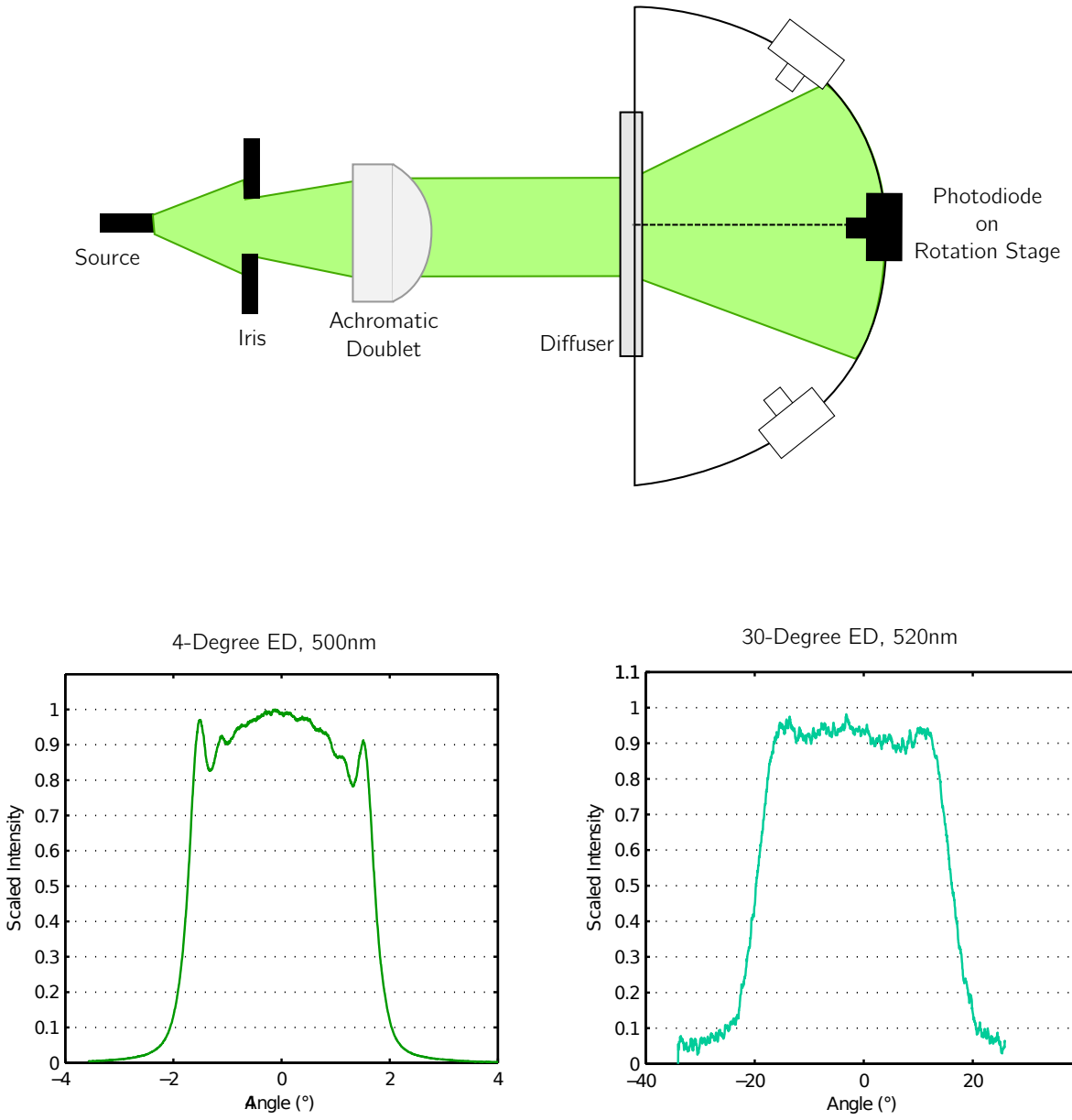

Figure 5-7: Top: diagram of alternate scheme for measuring angular profile of an Engineered Diffuser^{TM}. Bottom left: one-dimensional plot of 4° ED output, made with the camera imaging setup. Bottom right: Plot produced using the photodiode scheme with a 30° ED. Although the 30° profile shows a smaller amplitude in variation, and although the photodiode trace is noisier than the camera, the persistence of the *shape* of the profile is evident.

collimating lens to make the incident beam other than collimated. Results are presented in Figure 5-8 as one-dimensional profiles. In each case, although their relative positions and amplitudes vary, the same dome-and-ring structures persist. Large scale variation in brightness with angle seems to be an optical characteristic of the Engineered Diffuser itself.

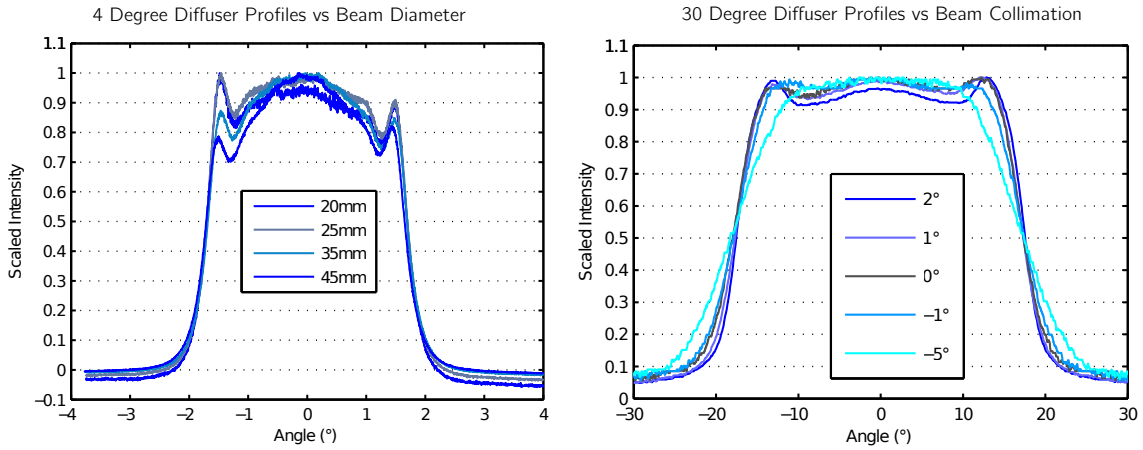

Figure 5-8: Profiles showing the persistence of angular structure in Engineered Diffusers. Left: a series of 4° diffuser profiles made by varying the diameter of the beam incident on the diffuser surface. Right: a series of 30° profiles made by varying the divergence angle of light incident on the diffuser.

We can further quantify the amount of variation in the 4° ED by analysis of data images. Figure 5-9 presents a statistical analysis of intensity variation at single wavelengths, expressed as the ratio of standard deviation to mean (σ/μ) for points within circular regions at radii from 0.5° to 2.0°, and at 400, 500, and 800nm. By this measure, spatial uniformity falls between 5 and 10% at all colors within the central 1.5°.

The ED, then, is not quite flat in angle: the amount of light output into various angular ranges varies by as much as 20% peak-to-peak. But it might be possible to engineer a system that would compensate for this angular variation – and although spatial uniformity at a single wavelength is ideal, it is not an absolute necessity. In a telescope calibration setup, as long as the uniformity is *known* and *stable*, we can compensate for single-wavelength intensity variation by rastering a single celestial source across the detector to "flatten" the flat-field.

The Engineered Diffuser might not be *ideal*, then, but there is still hope that it is ad-

equate. The ED does produce a beam which is already well-constrained, and which thus produces little stray or scattered light. Also, because little light is lost into unusable angles, the ED is an efficient element. What is crucial, though, is that any intensity variation be independent of wavelength: a fedora at 400nm must match a fedora at 1000nm to within 1%.

We turned then to examine the behavior of the Engineered Diffuser with wavelength.

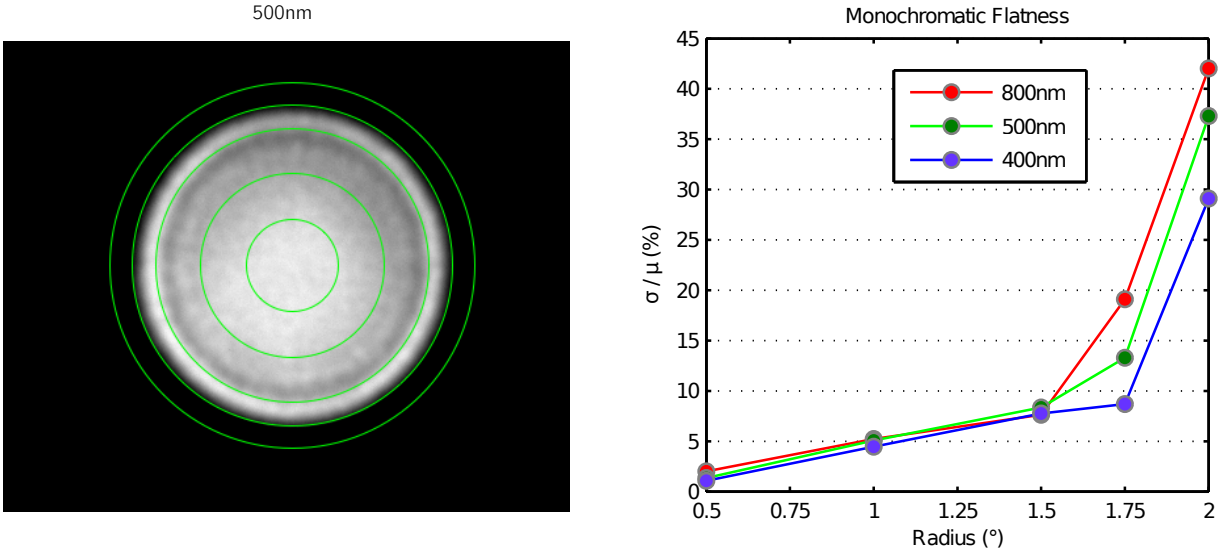

Figure 5-9: Quantitative evaluation of the flatness of monochromatic 4-degree Engineered Diffuser output. Left: data image at 500nm, with circular regions marked: the innermost green circle denotes an 0.5° radius, while the outermost is 2° from the center. Right: "flatness" plotted as σ/μ for all pixels within each circle. Spatial uniformity at all colors is below 10% within the central 1.5°.

Chromatic uniformity

Tests to determine the chromatic behavior of the Engineered Diffuser were run using the test camera setup. We found that the particular angular distribution of light off of the ED was indeed dependent on wavelength. While the general shape is constant – a central dome and a surrounding ring – the radius of the bright ring shifts inward with longer wavelength. Figure 5-10 depicts this result in data images and in one-dimensional profiles.

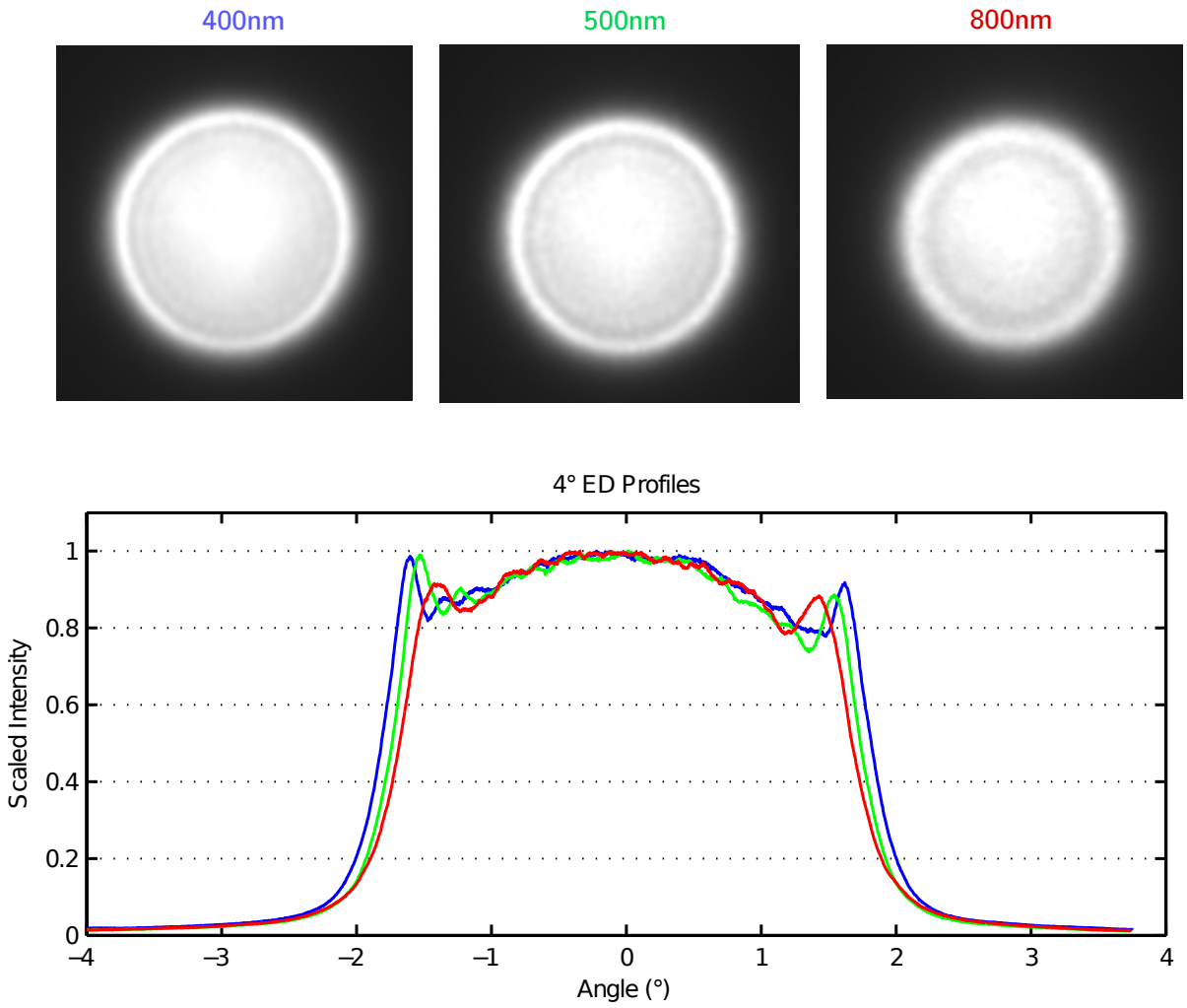

Figure 5-10: Top: a series of images taken at three wavelengths, without moving the camera or diffuser. Bottom: 1-dimensional angular profiles at the same three wavelengths. Note that both the overall diameter of the bright circle and the radius of the dimmest annular region shift inward with longer wavelength.

We evaluated the magnitude of chromatic variation by taking ratios of pairs of single-wavelength images: 800nm/400nm, 800nm/500nm, and 500nm/400nm.

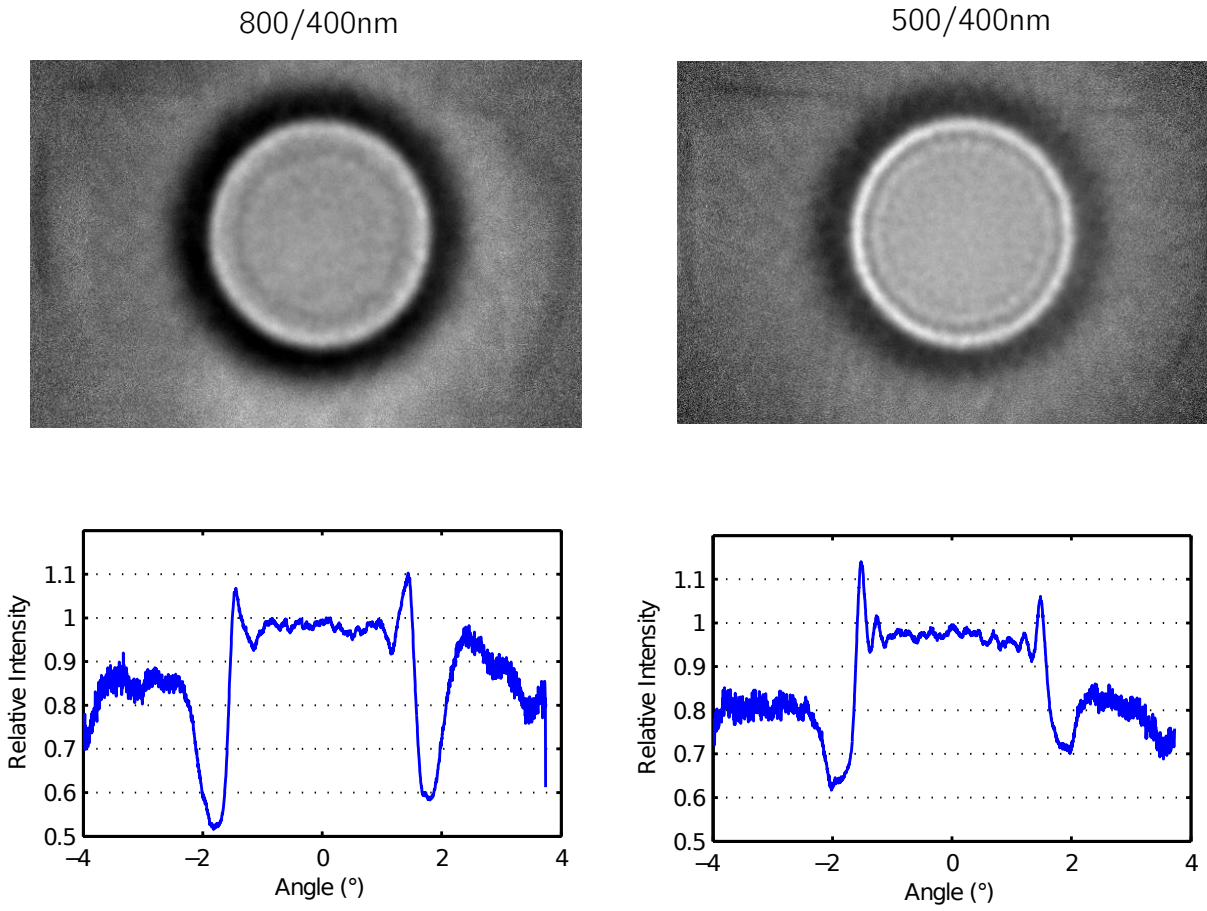

Figure 5-11: Ratios between angular radiance patterns of a 4° Engineered Diffuser at 400, 500, and 800nm. The presence of ring structures in the ratio images indicates systematic chromatic variation with angle.

We noted that, as in Figure 5-8 above the shape of the profiles changed as incident light was moved away from perfect collimation. Figure 5-13 shows a series of images taken at the same wavelength, while collimation of the incident beam was changed. Effects of this "defocus" are apparent even in simple inspection of the images.

We attempted to use the variation of profile shape with defocus to "align" profiles at different wavelengths, by selectively defocusing at each wavelength such that the profiles

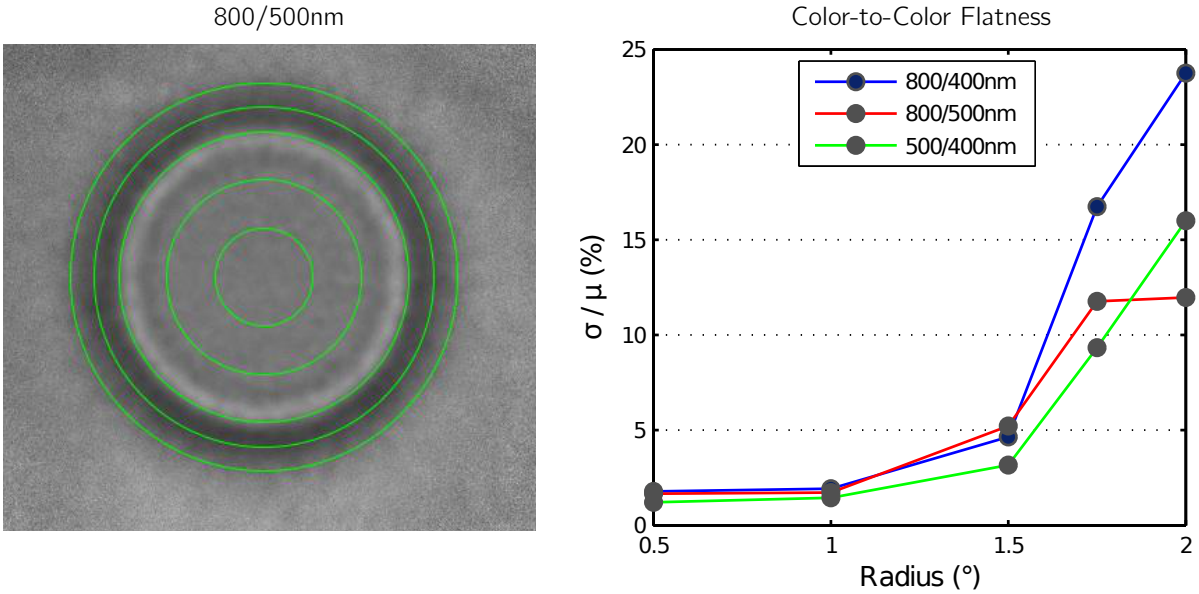

Figure 5-12: Quantitative evaluation of the color-to-color flatness of monochromatic 4-degree Engineered Diffuser output. Chromatic uniformity is approximately 2% near the peak, but rises sharply outside 1.5°.

matched. However, even for significant defocus – accomplished by moving the source fiber back and forth along the optical axis – the radial positions of the profile peaks and troughs do not vary enough to accomplish perfect overlap. Even at what we calculated to be the optimal defocus values, the one-dimensional profiles did not align. Results from the defocus tests are shown in Figure 5-14.

We conclude that the Engineered Diffusers^{TM}have persistent chromatic effects, which cannot be compensated by defocus alone. We note, however, that they are efficient at constraining stray light, and so we do not entirely discount their use.

Projector designs that make use of the 30-degree ED do not use it alone as the launch optic, but instead combine it with a three-lens relay system that acts as an optical reimager.

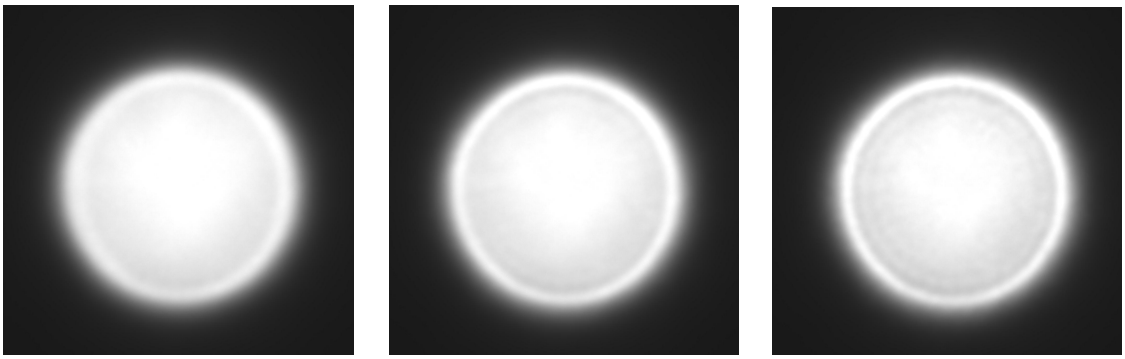

Figure 5-13: A series of images taken at a single wavelength (400nm), displacing the source by -10cm (left), -5cm (center), and 0cm (right) from optimal focus. The position of the bright ring changes slightly with focus.

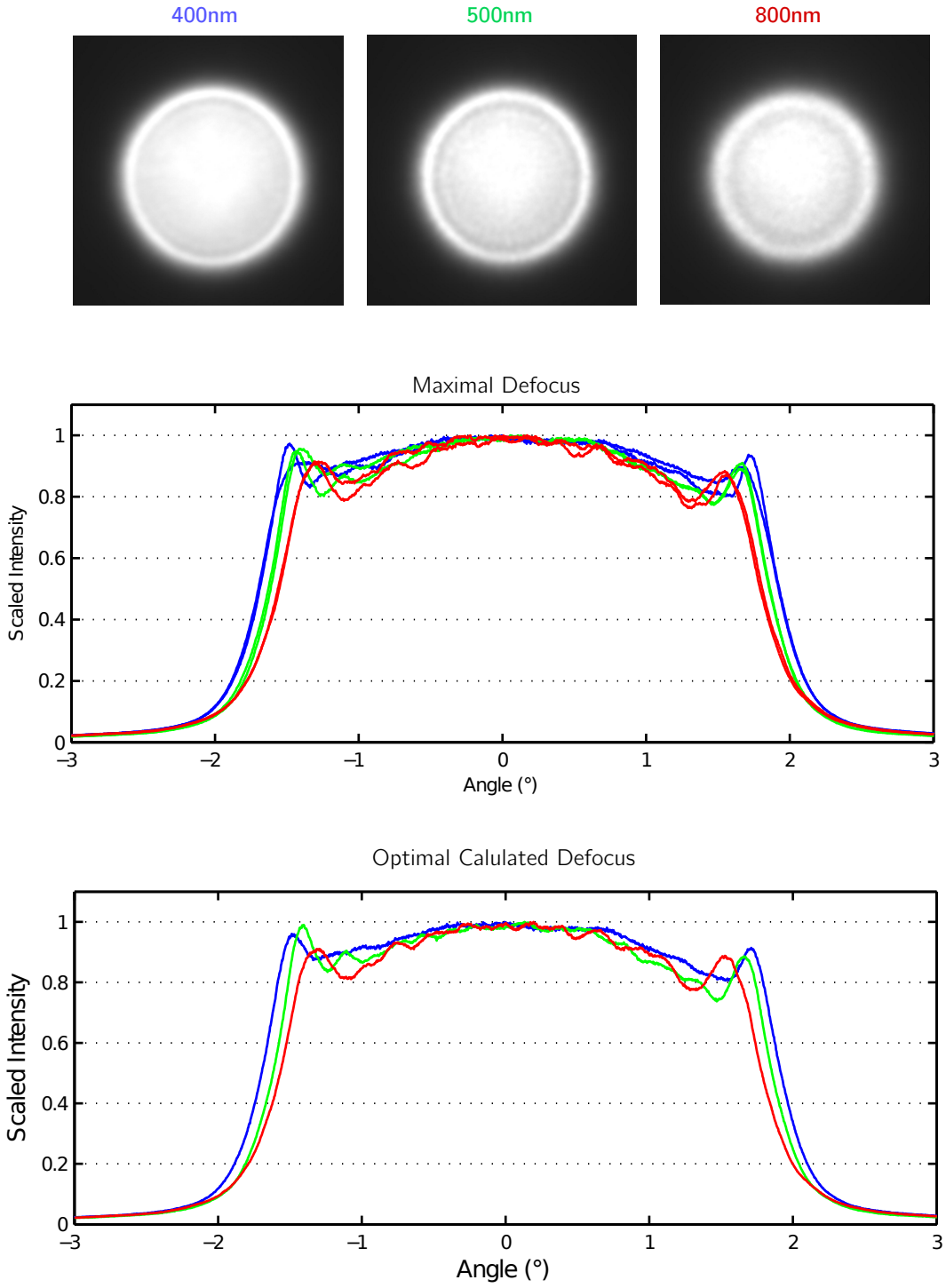

Figure 5-14: Attempts to force cross-color alignment of 4° ED profiles by selective defocusing. Top: images taken at three wavelengths, with images defocused to the calculated ideal. Center: a plot showing measured change in angular profiles with defocus for three colors. Bottom: one-dimensional angular profiles at three wavelengths, adjusted to "best" defocus.

5.3 Engineered Diffusers with an optical reimager

We tested two different ways of setting up the Engineered Diffusers in the projector: either by projecting light from the diffuser directly into the telescope pupil; or by using an optical relay system to produce an intermediate image.

The first of these two options is conceptually simpler, and would allow us to do away with the pre-collimating achromat and the collimating optic entirely. Instead, we would use only the single launch optic which, with a large pre-collimating Fresnel lens, is sufficient to produce light of the desired form. In this design, the aperture of the source fiber is placed at the focus of a fast Fresnel lens. A beam of collimated light exits the Fresnel and is incident on a 4-degree ED. Light then exits the ED as, ideally, a cone of light spread evenly across a half-angle of two degrees. The LSST's field of view is also circular, and has a half-angle of 1.75 degrees. Even without any additional elements, the 4-degree ED matches the requirements well.

The advantage of this design is its simplicity. Fewer elements are needed to create a final projector using this design than others, and consequently there are fewer elements to introduce unwanted reflections, to become misaligned, to accumulate dust over time. However, in this design, illumination at the telescope pupil plane would depend on the pattern of irradiance at the engineered diffuser, which may not be uniform. An optical fiber, for instance, might have transverse mode structure which can introduce significant brightness variation across the beam profile and thereby produce nonuniform irradiance at the diffuser. The diffuser and Fresnel lenses may themselves suffer from dust spots or other degradation.

We can avoid these issues entirely with a slightly more complex design: a system of relay lenses that produces an image at an intermediate pupil which is optically engineered to be the Fourier transform of rays leaving the diffuser. In other words, the intermediate image is a map of the angular distribution of rays produced by the diffuser.

With the optical relay in place, every point on the diffuser produces an image at the pupil plane, and the images produced by every point on the diffuser overlap. Given any two points, one in the pupil plane and one on the diffuser, there exists a ray connecting them.

Essentially, then, the optical relay averages over all points on the diffuser surface. The distribution of light at the pupil plane is entirely independent of irradiance on the diffuser: if one were to obscure one part of the diffuser, the pupil image would dim, but would not change shape. Figure 5-16 illustrates the design and benchtop realization of the optical relay launch optic.

With the optical relay system, the angular extent of the flatfield light on the detector is governed by the spatial size of the pupil. We ensure that the pupil is an appropriate size, and that stray light is minimized, by placing an iris at the exact plane of the pupil to serve as a baffle. Unlike the direct system, the optical relay system does require a collimating optic between the intermediate pupil and the telescope pupil.

In the next chapter we present an analysis of the two main options available for use as the collimating optic.

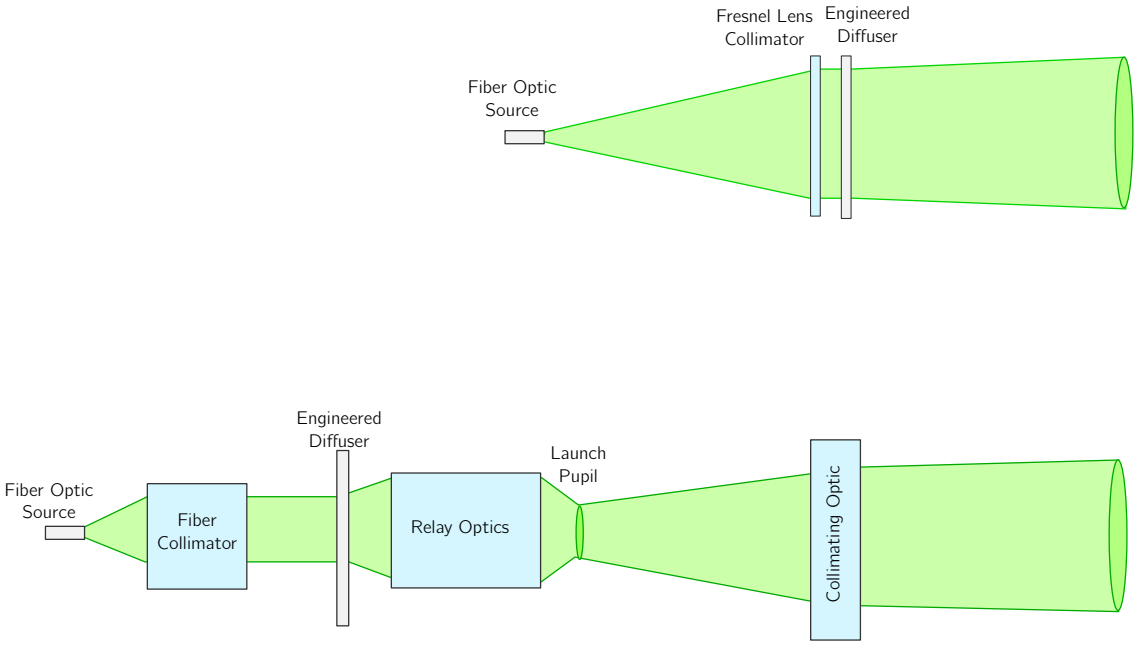

Figure 5-15: Schematic comparing the direct imaging to reimaging systems.

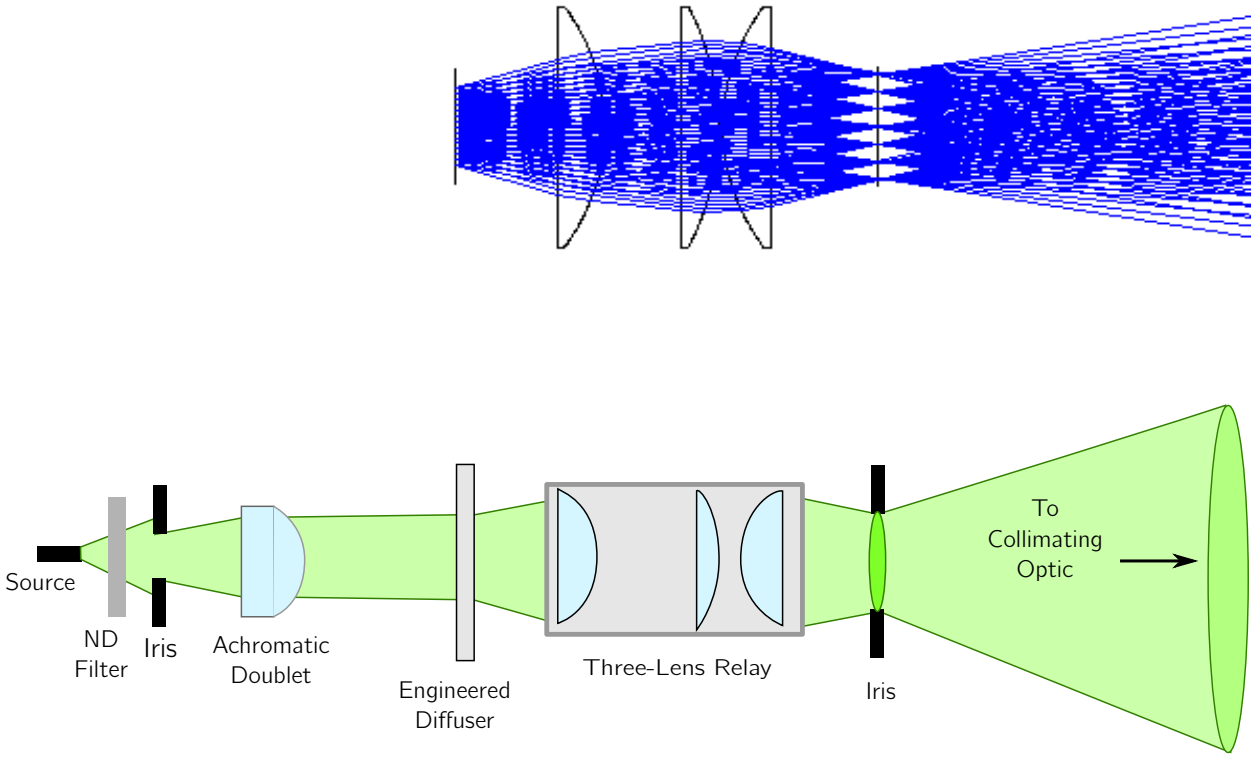

Figure 5-16: Schematic showing the design (top) and setup (bottom) of the optical relay launch optic. Collimated light is incident on an Engineered Diffuser; divergent light leaving the diffuser enters a three-lens relay system. The relay lenses are designed to map the angular distribution of rays leaving the diffuser onto a spatial distribution at the pupil plane. This pupil image must then be placed at the focus of a collimating optic for projection into the telescope and onto the detector. Design by Ming Liang (personal communication, July 2010).

Chapter 6

Analysis of collimation optics

The collimating optic is responsible for converting the launch optic's pupil image into a beam with the appropriate angular span at the entrance pupil of the telescope. We require that the collimating optic adequately collimate light; that it transmit or reflect light over the relevant wavelength range; and that it introduce minimal wavelength-dependent chromatic variation into the system.

We have a choice between two families of collimating optic: the transmissive lens and the reflective mirror. In principle, it is possible to obtain Fresnel lenses or parabolic mirrors of suitable diameter and focal length, so either option is viable for fabrication. The choice of a reflective or transmissive system will, however, dramatically impact the design of the final projector. If we choose a transmissive optic, the direction of propagation is constant: light enters the projector from one end, and exits from the other. A transmissive collimator would also allow us to enclose the entire system and better protect the optics from buildup of dust, grime, and any interference from inquisitive local fauna. If, on the other hand, we choose a reflective optic, the source fiber and launch optic will block some of the reflected light from reaching the telescope pupil. Additional support "spiders" or other structures will be required to hold the components in place while obscuring at little reflecting area as possible, and an enclosure is less practical with a reflective collimator. A schematic of the design selected by each type of collimator is shown in Figure 6-1.

From a structural standpoint, then, we might prefer the transmissive setup for its simplicity. The main concern of a refractive system, as opposed to a reflective one, is *chromatic aberration*: variation in an optic's focal length or magnification with wavelength.

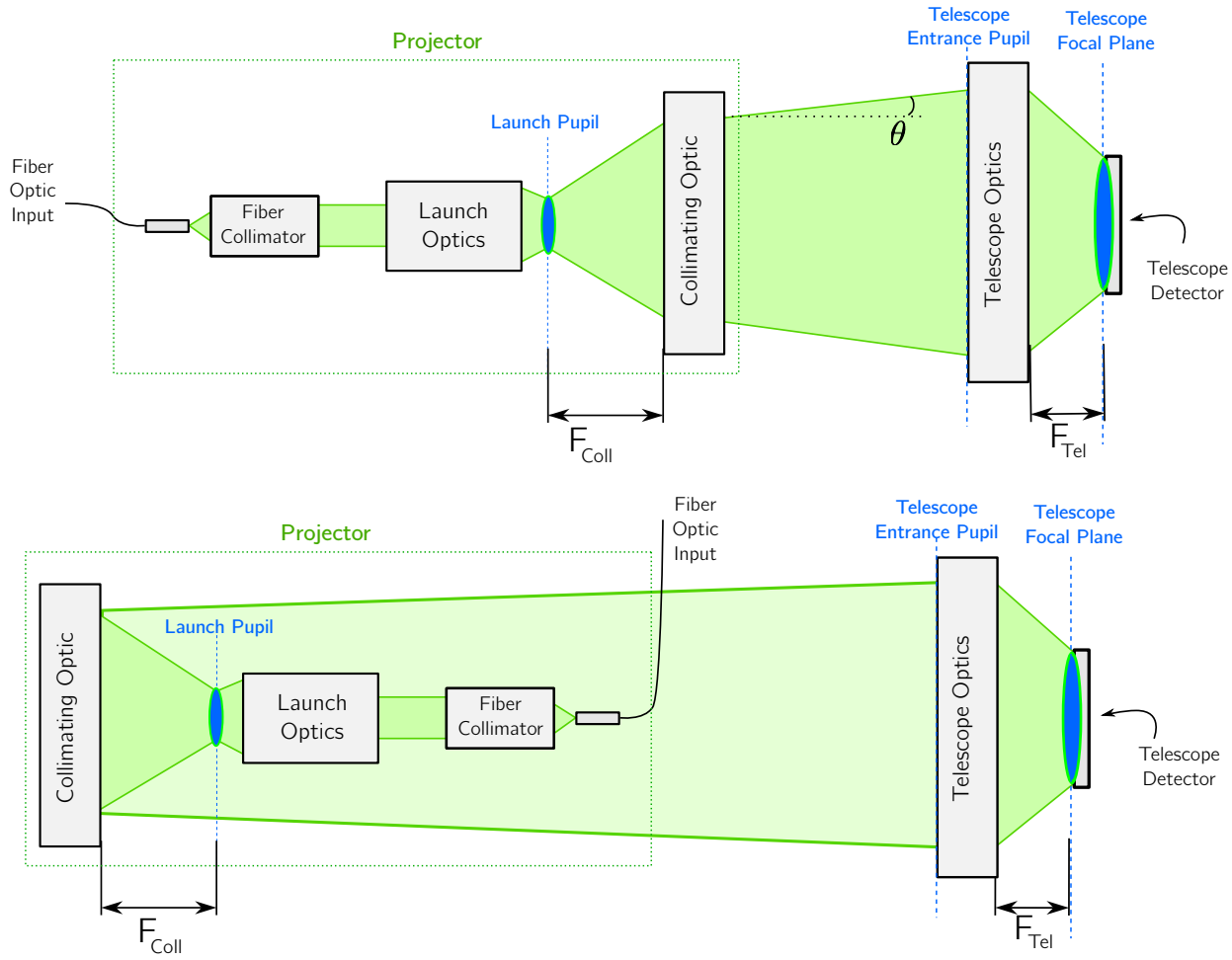

Figure 6-1: Comparison of projector designs using transmissive (top) and reflective (bottom) collimating optics.

6.1 Transmissive collimator: the Fresnel lens

We hope, in the full LSST design, to limit the number of individual projectors in the array. In the scheme with 162 projectors, the collimating optic must have a diameter on the order

of 1-2 feet. Constructing a solid convex lens on this scale is difficult and, for our purposes, impractical. Instead, we use a Fresnel lens. The Fresnel lens is made of a transmissive substrate into which concentric annular rings have been carved, granting it the focusing properties of a lens. Fresnel lenses of a given size are lighter weight and less bulky than their spherical counterparts, and can be straightforwardly manufactured on scales up to a meter diameter. As compared to a conventional spherical lens, though, the imaging quality of a Fresnel lens suffers. We evaluated several Fresnel lenses made out of various types of acrylic, as well as some flat (unetched) samples of material that might serve as suitable Fresnel lens substrates.

The lenses were first examined for transmittance across the wavelength range. We took transmittance spectra with the broadband light source and an Ocean Optics HR-2000 spectrometer. All lenses tested transmitted well between 400-1000nm. Limitations of the spectrometer grating made testing above 1000nm difficult, but we were able to verify that the flat samples of material transmitted well in the near-UV by using a Hg-Ar calibration lamp, which has strong near-UV output, as a light source. Transmission between 400-1000nm seems not to be a problem, and even if available off-the-shelf Fresnel lenses suffer in the UV, materials do exist that transmit adequately, and which can be made into Fresnel lenses for the final iteration of LSST projectors. Fresnel lenses are therefore suitable to transmit the required light.

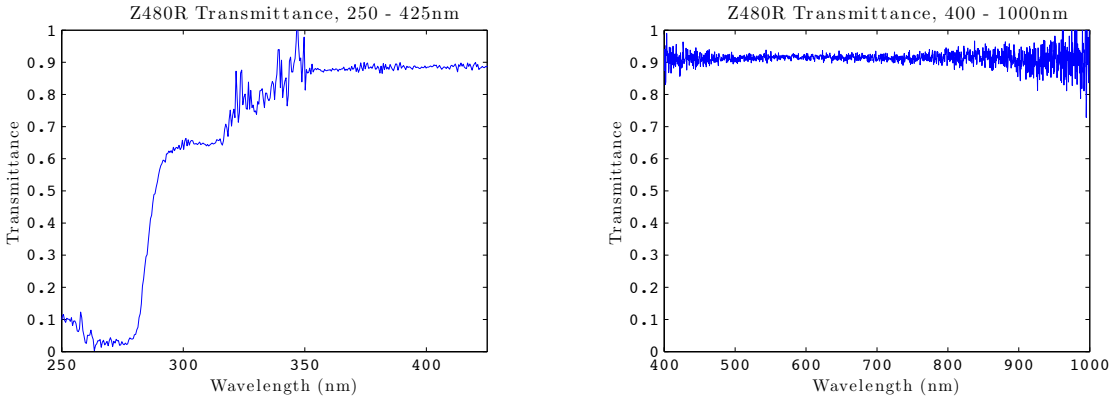

Figure 6-2: Transmittance of a potential Fresnel lens substrate, Zeonex Z480R, from 250-1000nm.

Figure 6-3: Photos of Fresnel lenses on the lab bench. Note the "rainbow" effects at the edges of imaged objects, indicating chromatic aberration.

Chromatic behavior, though, was another question. All of the Fresnel lenses tested showed obvious chromatic aberration on inspection: objects seen through the lens produced the "rainbows" characteristic of dispersive effects. Photos of a few of the lenses are given in Figure 6-3.

Chromatic aberration in an optical system can be either axial or lateral. Axial chromatic aberration manifests as on-axis light coming to a wavelength-dependent focus: there may be measurable differences in focal distances, or visible colored rings when focusing white light. Lateral chromatic aberration results in off-axis light being deflected by different amounts depending on wavelength, so that *magnification* is different across wavelengths. Figure 6-4 illustrates the difference between the two varieties of chromatic aberration. I attempted to measure both axial and lateral chromatic aberration in the Fresnel lenses.

We measured axial color effects by feeding monochromatic light through an optical fiber, collimating it with the achromatic doublet, and shining it through the Fresnel lens along the lens' optical axis. We used a card mounted on a micrometer stage to gauge lateral deviation in focus. For every Fresnel lens we tested, though, axial chromatic aberration was so small as to be undetectable by manual methods. White light brought to a focus showed no evidence

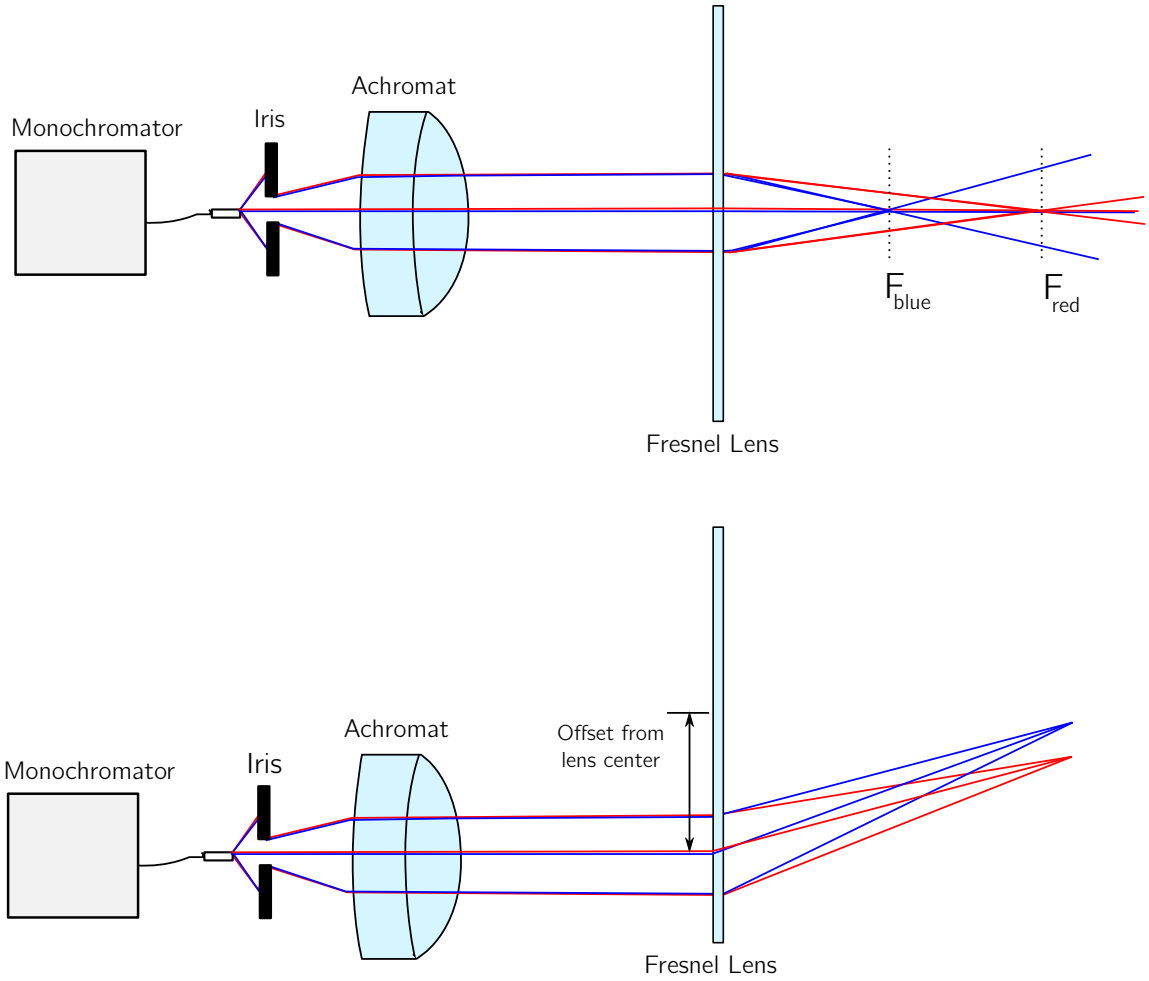

Figure 6-4: Diagram illustrating measurements of axial (top) and lateral (bottom) chromatic aberration.

of color rings; measuring the focal length of monochromatic light indicated that any focus difference was well inside the measurement error.

We measured lateral chromatic aberration with a similar setup. This time, though, we translated the collimated beam off the optical axis, so that it shone through an off-center region of the Fresnel. We then measured the lateral distance between light at wavelengths from 400 to 650nm. Because measurements were taken by eye, the wavelength range was limited to visible light. Figure 6-5 depicts a representative sample of lateral chromatic aberration measurements in Fresnel lenses.

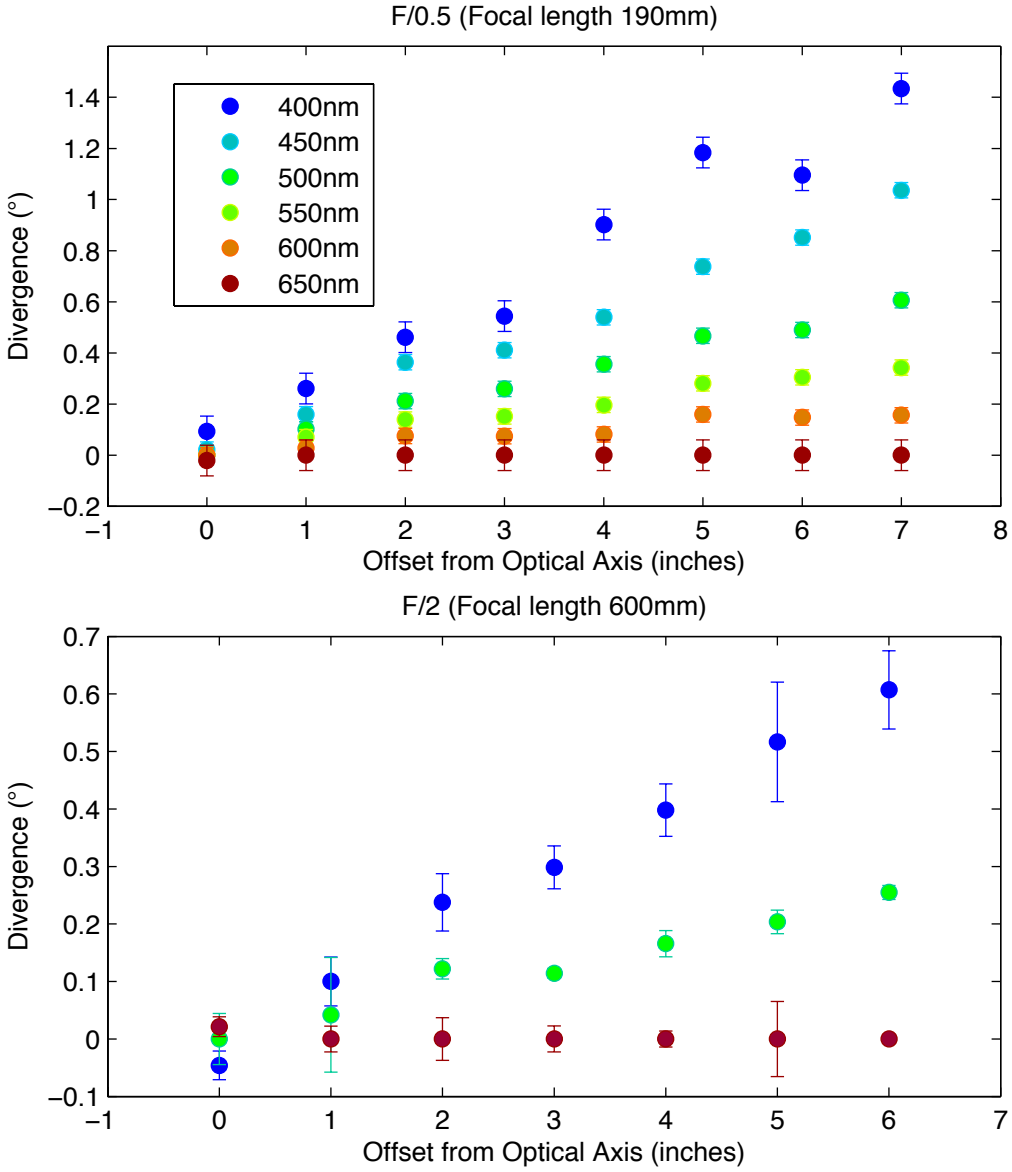

Figure 6-5: Plot of lateral chromatic aberration between 400 and 650nm in two Fresnel lenses. These values were determined by sending a collimated monochromatic beam through a region of the lens offset from center, and measuring the resulting offset of the focal points. For clarity of visualization, all offsets have been plotted relative to 650nm. The faster lens shows greater chromatic aberration, but even the slower lens, which has a focal length of 60cm, shows significant aberration in light transmitted even a few inches off-center.

Transmissive optical elements show chromatic aberration because they are made of materials whose refractive index varies with wavelength. Different colors of light are differently refracted as they pass through the material. A few of the Fresnel lenses tested were made from a material, Reflexite, whose manufacturer provided information on refractive index. A plot of the dispersion curve is shown in Figure 6-6. There is significant change in refractive index between 400 and 1000nm.

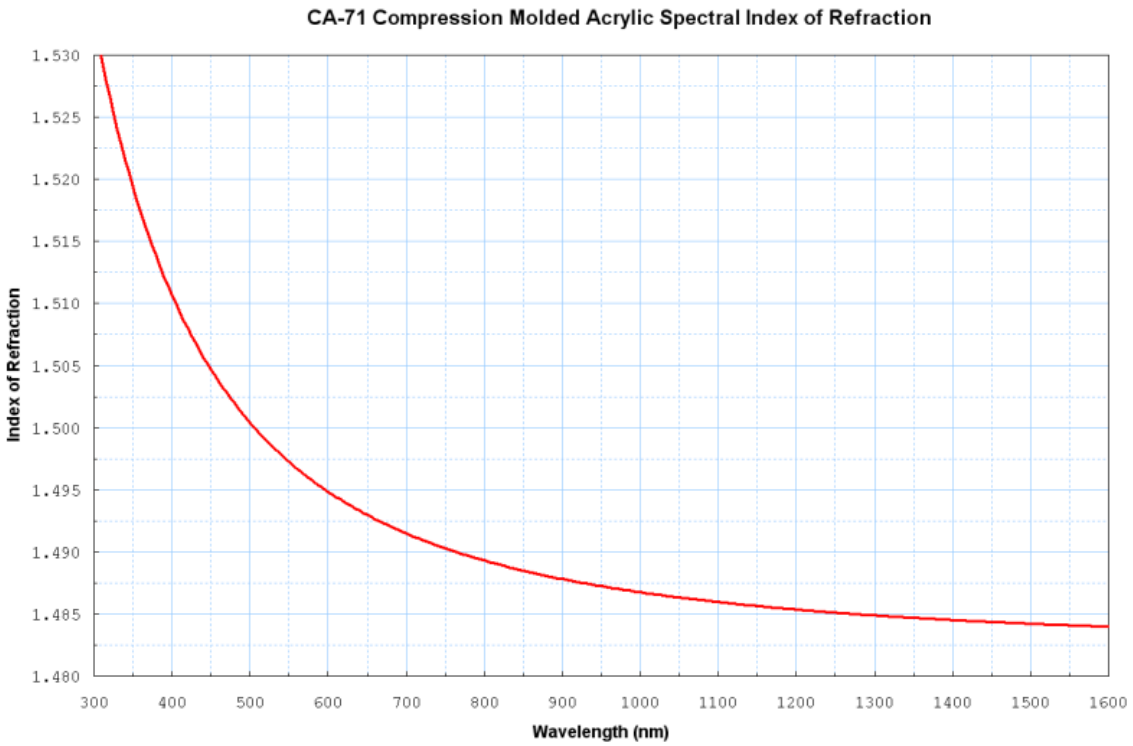

Figure 6-6: Manufacturer's dispersion curve for a Reflexite Fresnel lens.

The magnitude of observed chromatic aberration in the Fresnel lenses suggests that we not discard the reflective option, despite its added complexity and obscuration.

6.2 Reflective collimator: the parabolic mirror

The reflective element under consideration was a concave parabolic mirror. A reflective collimator in the projector system must have a diameter large enough to capture all the light from the pupil, while also having a short enough focal length that the entire system can fit with the specified 1-meter depth. In other words, we require a relatively large, fast mirror. Such mirrors, although they can certainly be manufactured, are more expensive and more difficult to obtain than a Fresnel lens of comparable size. For testing, we used a 16-inch diameter F/1.1 aluminum front-surfaced mirror. The mirror is mounted vertically on the optical table. It has a central mounting bracket with a diameter of 5 inches. The usable reflective surface, therefore, is limited to an annular region with radius $\Delta r = r_{mirror} - r_{mount} =$ 5.5 inches. A photo of the mirror is presented in Figure 6-7.

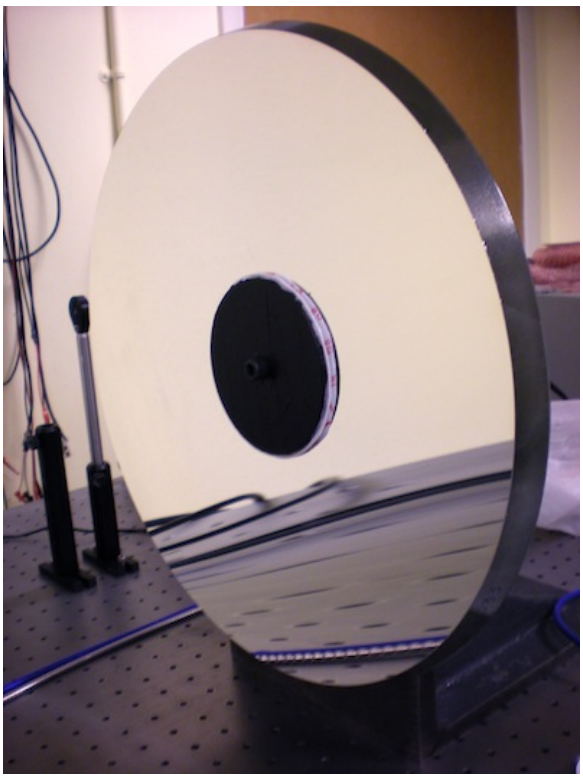

Figure 6-7: Photo of concave parabolic mirror as mounted on the lab bench. The central mounting bracket was covered in matte black tape to minimize stray light.

Mirror reflectance was measured with the spectrometer and the broadband source. Again, data is limited to the range between 400-1000nm. At these wavelengths, the mirror's reflectance is adequate for our purposes: it reflects enough light that projector properties can be measured across the color range.

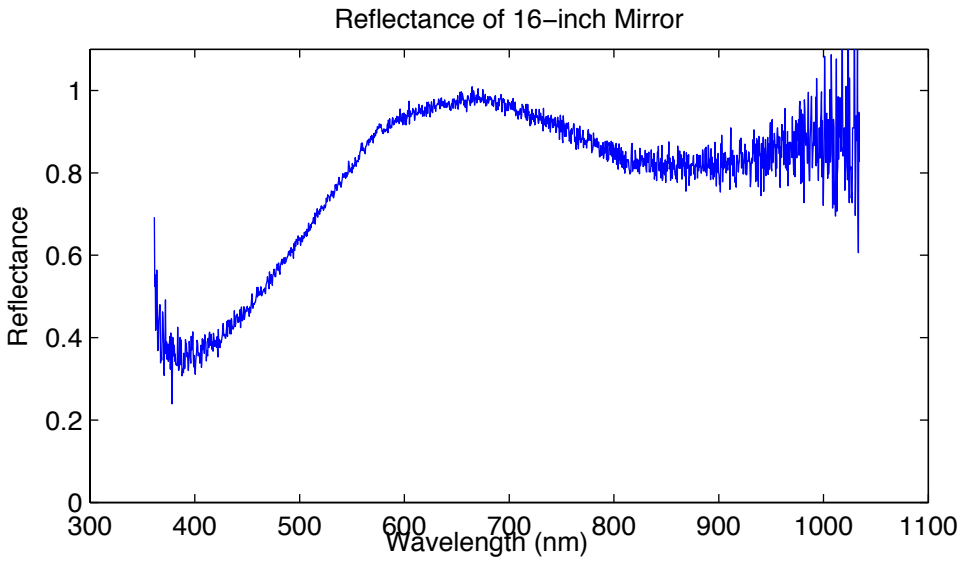

Figure 6-8: Reflectance of aluminum-coated parabolic mirror from 400-1000nm.

Because reflection does not involve a material's refractive index, no chromatic aberration is expected with a reflective element, and, indeed, none was seen either by inspection of the mirror itself– the photo in Figure 6-7 shows no rainbows – or by observing the focal properties of a white-light beam. We conclude that the optical properties of the mirror make it suitable for use as a collimating optic.

Chapter 7

Analysis of the combined calibration system

The launch and collimation optics together comprise the full projector. Having determined the characteristics of each component separately, we built full single-projector prototypes in the lab and tested each. This chapter presents tests on functional prototypes of a full calibration projector, and quantitative measurements of the desired flat-field attributes: detector-plane flatness, constrained angular extent, and achromaticity of detector-plane patterns.

7.1 Engineered diffuser with Fresnel lens

Chapter 5 discussed the two possible designs that use an Engineered Diffuser with a Fresnel lens. The simpler design uses the Fresnel as a large-area lens to collimate light from the fiber optic, producing a wide collimated beam incident on a large-diameter 4° diffuser. While conceptually the simpler, this design has the disadvantage of susceptibility to variation in illumination pattern exiting the source fiber. The second option is the one tested here. It uses a three-lens relay to produce a pupil image whose brightness distribution is independent of irradiance at the diffuser surface. This pupil image is then reimaged onto the detector at the focal plane, where the spatial extent of the image at the pupil plane translates into

spatial size of the bright circle on the detector.

7.1.1 30° ED with relay

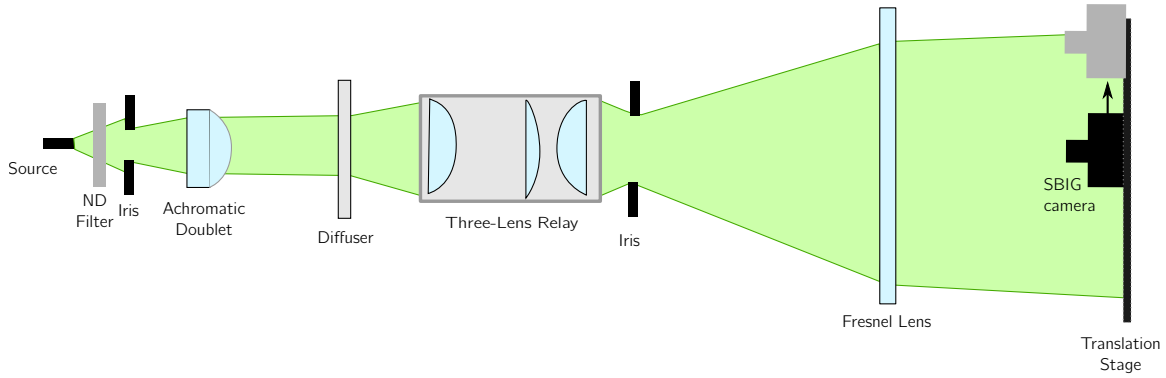

Figure 7-1: Benchtop setup for testing of a projector system comprising an Engineered Dffuser with optical reimager as launch optic and a Fresnel lens collimator. The camera can be translated along the stage shown above, as well as another that runs perpendicular (in and out of the page).

We first tested a projector system that used a 30° circular tophat Engineered Diffuser with an optical reimager as launch optic and a Fresnel lens as collimator: Figure 7-1 shows the full system setup. A neutral density filter was used to avoid saturating the CCD, and adjustable irises were put in place to minimize stray light.

Figure 7-2 shows representative data images and one-dimensional plots for an on-axis measurement, i.e., when the camera and Fresnel lens were positioned on and aimed along the projector's optical axis. As expected, the data resembles that for the diffuser alone. The same overall dome-and-ring shape is present, and the ring moves inward with longer wavelength.

To simply observe the persistent structure, though, doesn't give us a sense of how much variation there is in either spatial or wavelength regimes: we proceed to a more quantitative analysis.

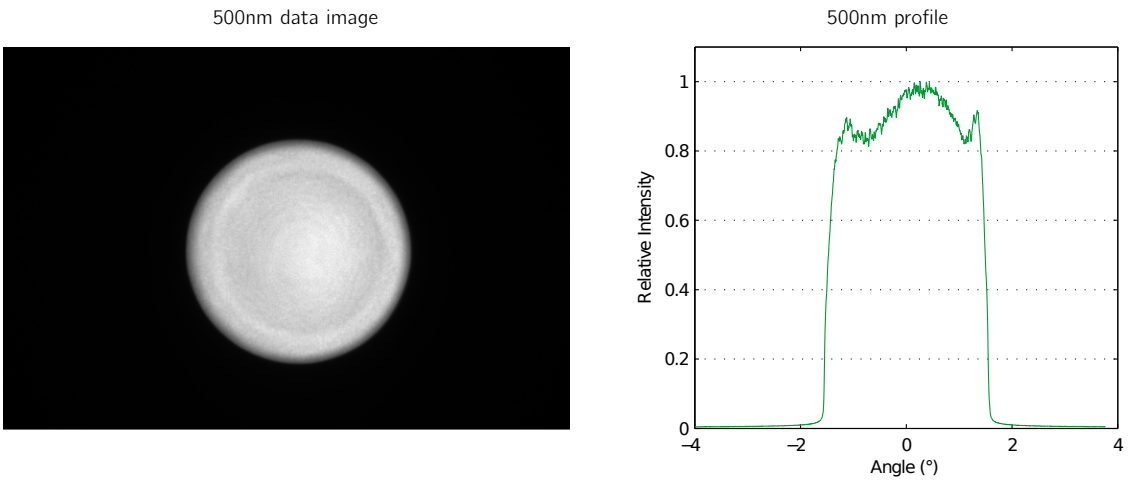

Figure 7-2: Sample data image and one-dimensional plot showing the angular profile of a reimaged 30° ED.

Stray Light

As compared to the 4° diffuser alone, the reimaged 30° ED has even better suppression of stray light, due to the presence of a launch-pupil baffle that blocks scatter at unwanted angles. The sample profile in Figure 7-2 confirms the success of this projector at minimizing stray light: outside a 2° radius, the levels of light incident on the detector fall well below 5%, and approach the 1% level of ambient light in the lab.

Spatial uniformity

Spatial uniformity – variation in intensity between pixels of the detector at a single wavelength – was measured by statistical analysis of counts within concentric circular regions of the beam as measured on the CCD. At single wavelengths from 400nm to 800nm, intensity variation was on the order of 5-10%. Results are presented graphically in Figure 7-3.

Chromatic uniformity

In quantifying the chromatic flatness, we first examined images at each color when the Fresnel lens and camera are aligned with optical axis of the optical relay lenses. Such an analysis

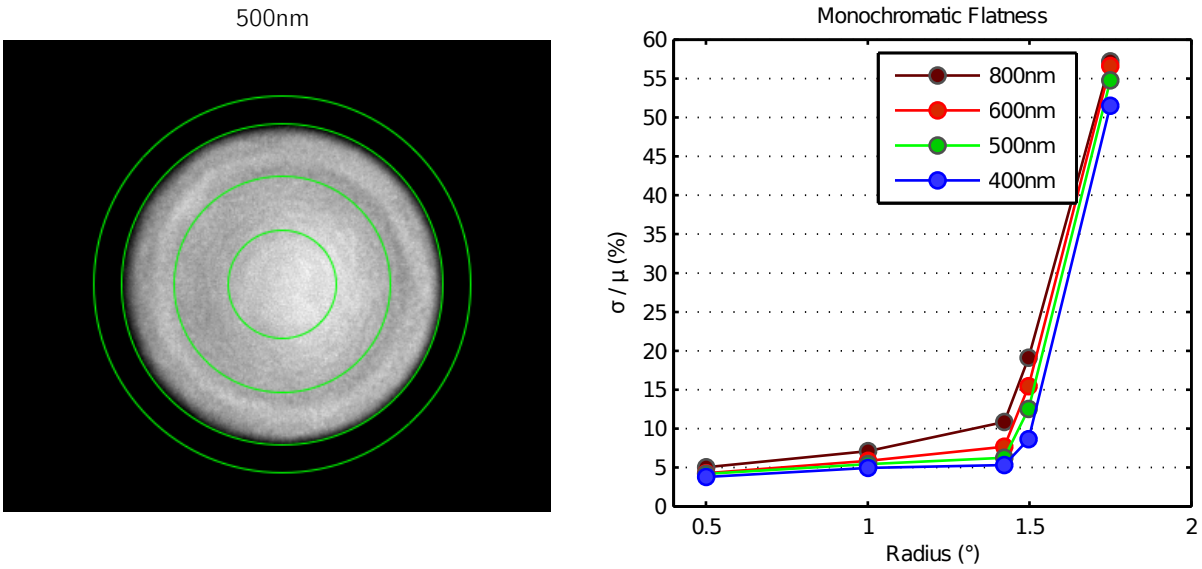

Figure 7-3: Quantitative analysis of flatness of illumination produced by a 30° ED, relay optic system, and Fresnel lens.

should ideally suffer only minimally from lateral chromatic aberration in the lens, and thus allows us to examine chromatic variation intrinsic to the 30° ED. A plot is shown in Figure 7-4.

Statistical analysis again allowed us to quantify variation between colors, and again we did so by dividing monochromatic images. Sample divided images and profiles are presented in Figure 7-5. Figure 7-6 shows results of flatness analysis performed on divided monochromatic data. Percentage variation is on the order of 5-15% across the projected circle.

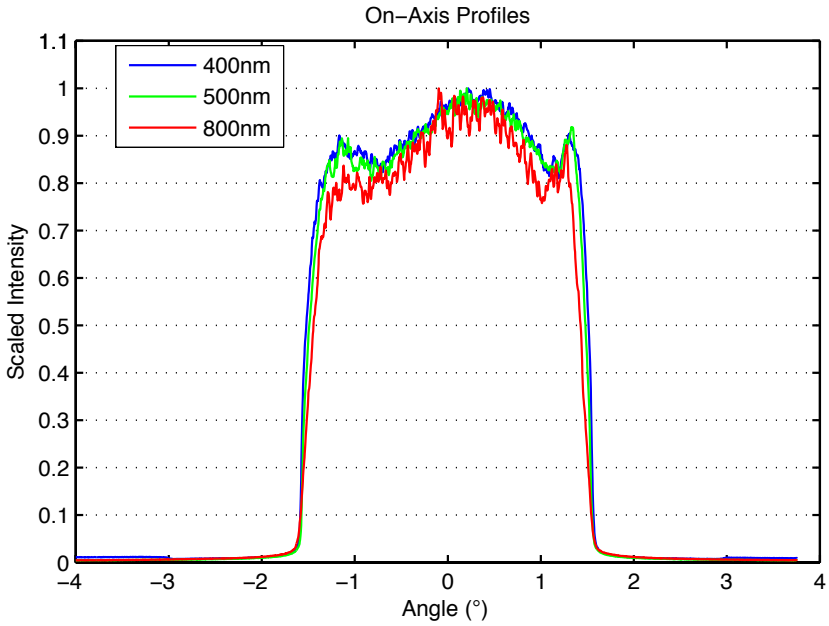

Figure 7-4: On-axis monochromatic profiles produced by a 30° ED, optical reimager, and Fresnel lens projector.

It is evident from the diagram in Figure 7-1 that the test camera cannot capture all of the projected light at once. Instead, the camera was mounted on motorized linear stages, one horizontal and one vertical, which allowed us to freely position it within the plane perpendicular to the optical axis. When the camera is translated off axis in this manner, it gathers light that has passed through the Fresnel lens off center. We can then gauge the effects of combined effects of chromatic aberration in the Fresnel lens and intrinsic variation in the ED by looking for variation between images taken at different colors.

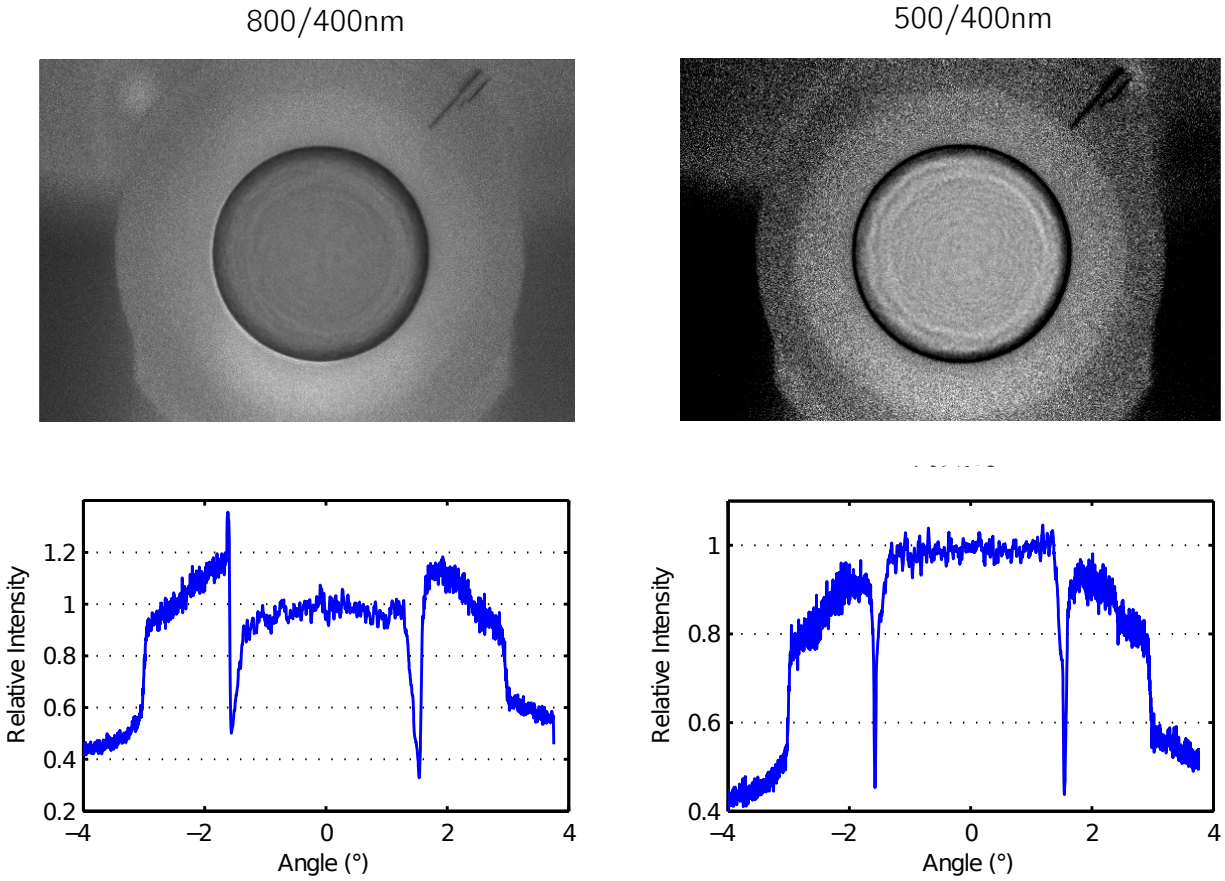

Figure 7-5: Sample images and one-dimensional profiles of color-to-color ratios produced by a 30° ED, optical reimager, and Fresnel lens projector.

We find that, with this projector prototype, moving the test camera across the projected beam does have significant effect on the pattern of light at the detector: effects of motion

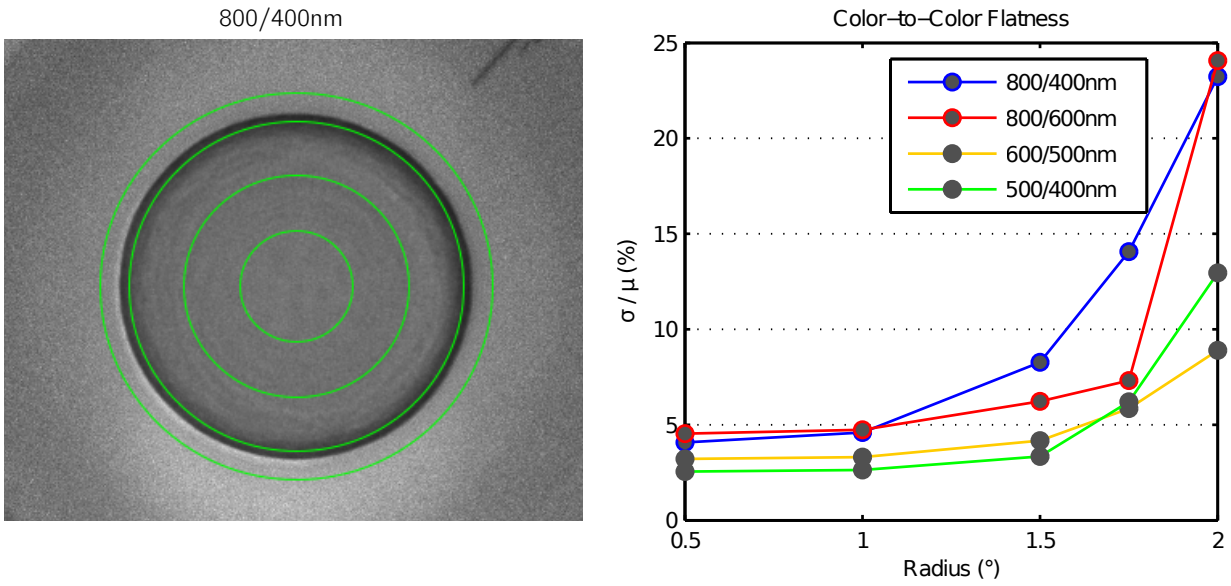

Figure 7-6: Quantitative analysis of color-to-color uniformity of light from a 30° ED, relay optic system, and Fresnel lens.

are readily apparent by inspection of successive images. In Figure 7-7 we have made them yet more apparent by synthetically (if arbitrarily) coloring frames by computer. Each frame was assigned a color roughly corresponding to its wavelength (i.e., 500nm was colored green). Colored frames were then stacked to illustrate chromatic effects. The top image in Fig 7-7 shows a stack of on-axis frames. Frames at all colors are concentric, and the image appears white, with the telltale blue ring along the outer edge to indicate the ED's characteristic widening of bluer profiles. The middle image shows a set of images taken with the camera 2.5" off axis – approximately 2/3 of the way from the optical axis to the edge of the projected beam. This region is severely afflicted by chromatic aberration: the colors are misaligned. Finally, the bottom image shows a series of frames taken at 400nm, as the camera moved from on-axis to 2.5" off axis. The position of the 400nm profiles on the detector varies as the camera moves.

Figures 7-8 and 7-9 present the second and third images of 7-7 as one-dimensional plots. First, Figure 7-8 demonstrates the effect of cycling through the available filters while holding the camera fixed at a particular off-axis position. Each plot in the series shows one-

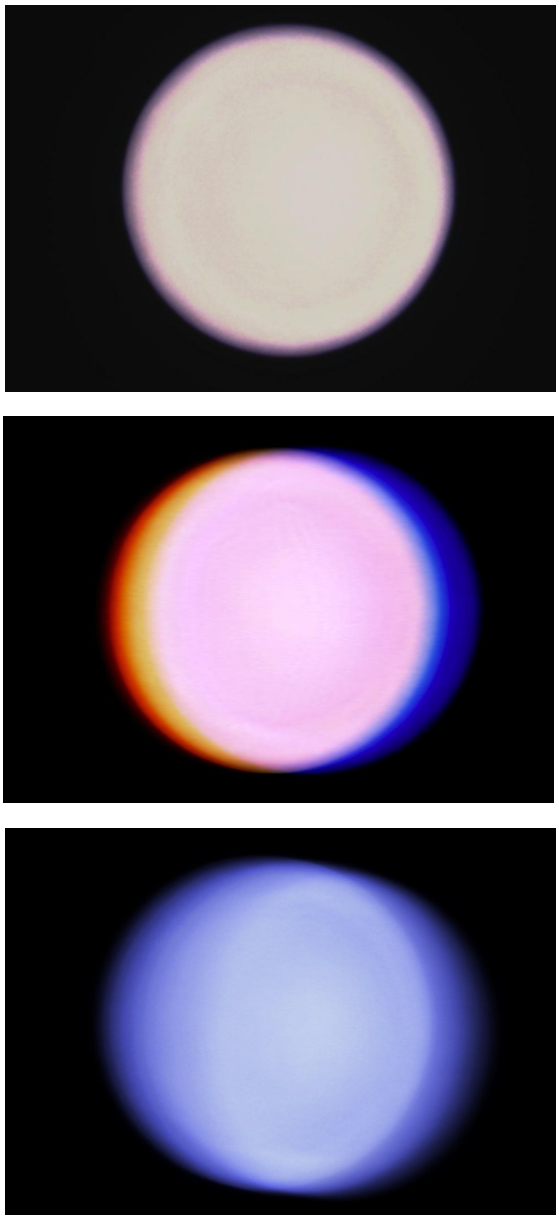

Figure 7-7: Synthetically colored images illustrating chromatic effects in the Fresnel lens system. Top: synthetic-color image of on-axis light at 400, 500, 600, and 800nm; single-color frames have been stacked and assigned colors by computer. Note the blue ring around the edge of the circle, indicating the persistence of chromatic variation in the ED itself. Middle: a synthesized image of multiple filters, showing the displacement of images at one color relative to another as detected by a fixed camera. Bottom: a synthesized image made of individual data images, all at 400nm, showing displacement and distortion between images at the same wavelength as the test camera is translated off axis.

dimensional profiles at 4 wavelengths from 400 to 800nm. It is evident that as the camera moves off-axis, the spread between wavelengths increases. Figure 7-9 shows an alternate presentation. Here, we first selected a filter, then moved the camera from the optical axis to the edge of the projected beam, in half-inch increments. Each plot in Figure 7-9 represents a single one of the bandpass filters – 400, 500, 600 and 800nm. This series makes it clear that chromatic aberration is worst at 400nm, and minimal at 800nm.

We attempted to further quantify the chromatic behavior by making dispersion curves. The curve shown in Figure 7-10 depicts displacement of the image center on the focal plane, in degrees, as a function of camera translation in inches. Note that even a few inches' displacement across the beam shifts the 400nm image by a substantial fraction of a degree – a 2" displacement, which is approximately midway between the beam center and its edge, represents an angular displacement equal to 1/10 of the LSST field of view.

The projector with the optical reimager system is designed to image the launch pupil onto the detector plane. The size of the pupil image determines the spatial extent of focal plane illumination: simple raytracing indicates that an image of height h will produce a beam from the collimator with divergence half-angle $\theta = \tan^{-1}(h/F)$, whre F is the focal length of the collimator. But the pupil image is a map of angles leaving the Engineered Diffuser. If we were to use an ED with a *wider* angular spread to produce a *larger* pupil image, we could then baffle out all but the center of the ED's angular response pattern, thereby clipping the "wings" of the ED profile.

We attempted this variation using a 50° ED.

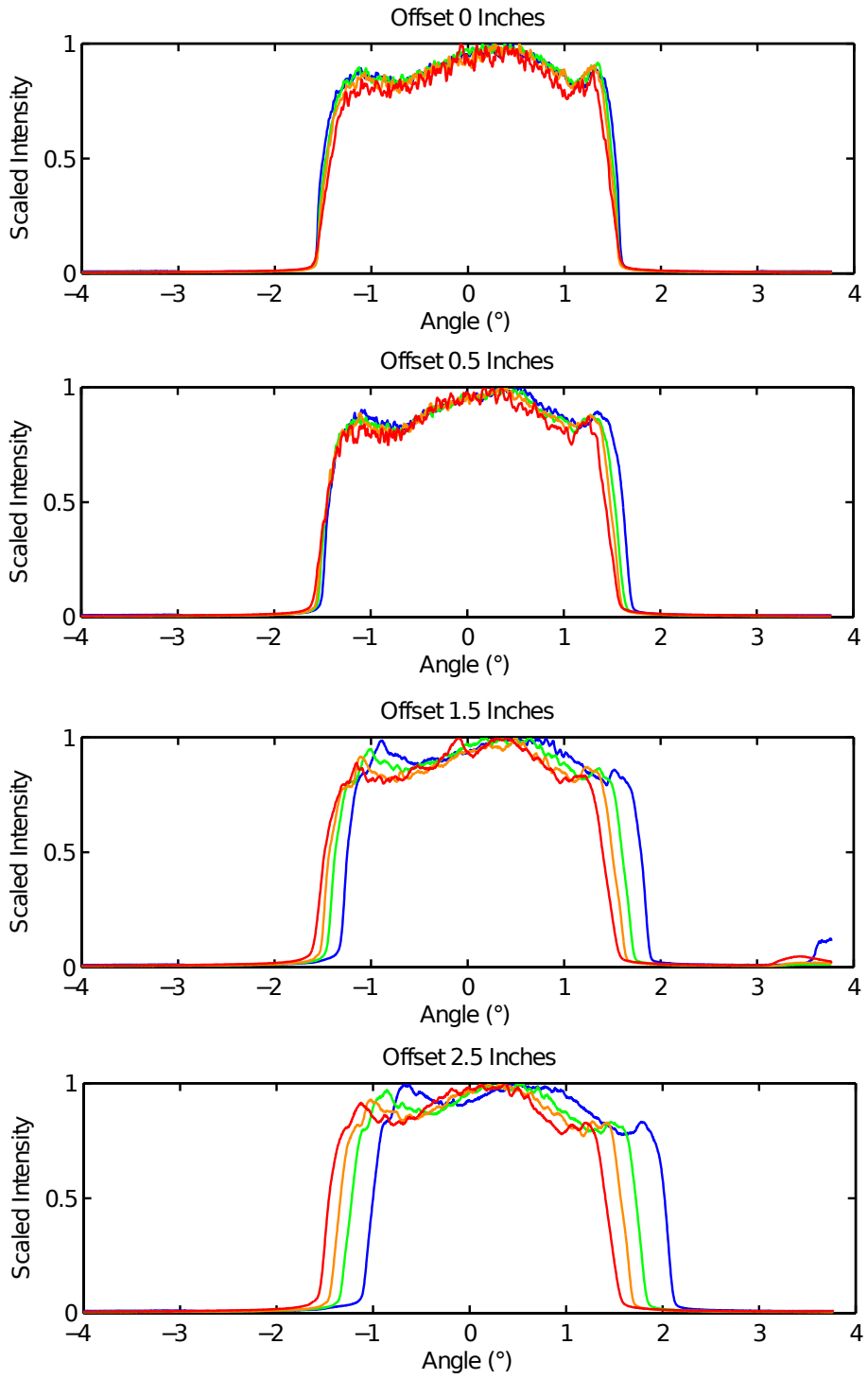

Figure 7-8: Plots corresponding to the second image in 7-7 at camera positions from on-axis to 2.5 inches off axis. Note that as the camera moves farther off axis, the spread between wavelengths increases. 2.5" off axis is approximately 2/3 of the way from the beam center to its edge. Thus a single projector using this setup might result in patterns offset by as much as 0.5-1° between 400 and 800nm.

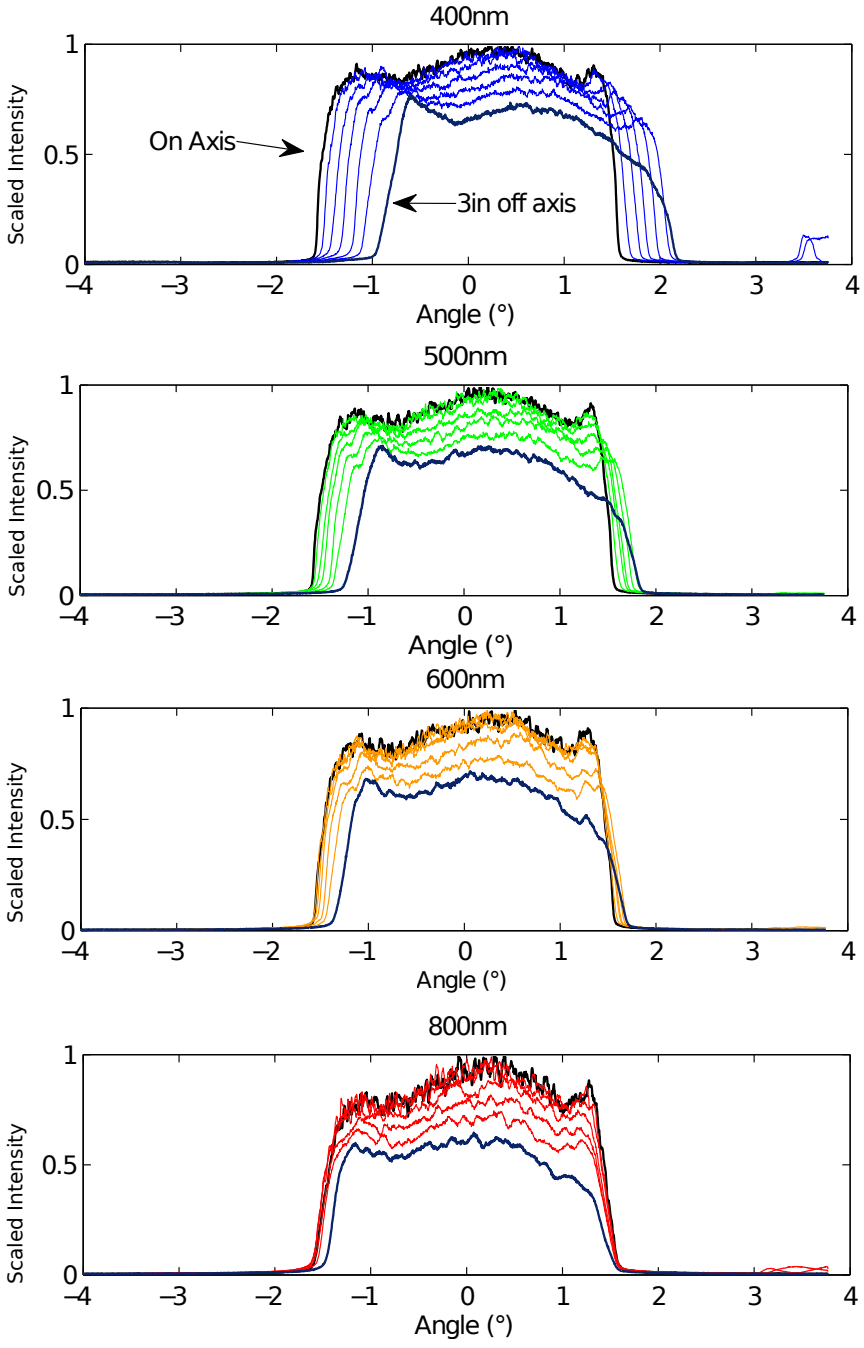

Figure 7-9: Plots corresponding to the third image in 7-7 at wavelengths from 400 to 800nm. In each subplot, the upper black trace is the on-axis trace, while the lower represents 2.5" off axis. Note that the profiles at 800nm are aligned, but the spread becomes progressively worse at shorter wavelengths.

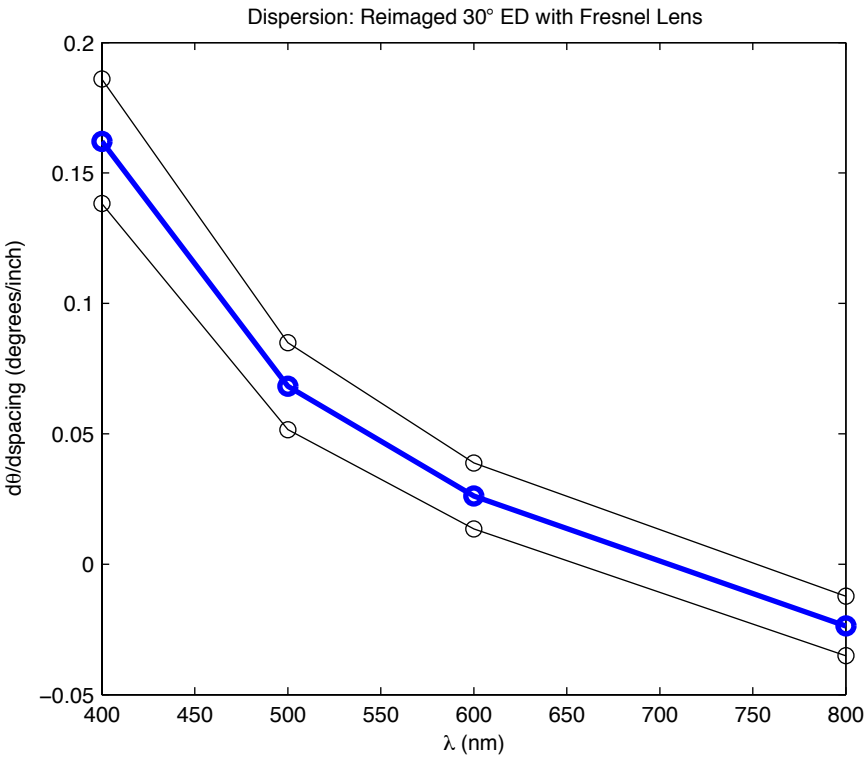

Figure 7-10: "Dispersion" curve for projector system comprising 30° ED, optical reimager, and Fresnel. Values plotted represent the mean angular shift of the center of the profile at each wavelength seen per inch of camera motion. The gray curves denote 1-σ errors.

7.1.2 50° ED with relay

The benchtop setup for a 50° ED with Fresnel lens collimator is nearly identical to the 30° ED setup, with the exception of the particular diffuser used. The iris at the pupil image is crucial to this setup, because it allows baffling of the outer ring as well as stray light and edge sharpness control. Sample data and one-dimensional profile are given in Figure 7-11.

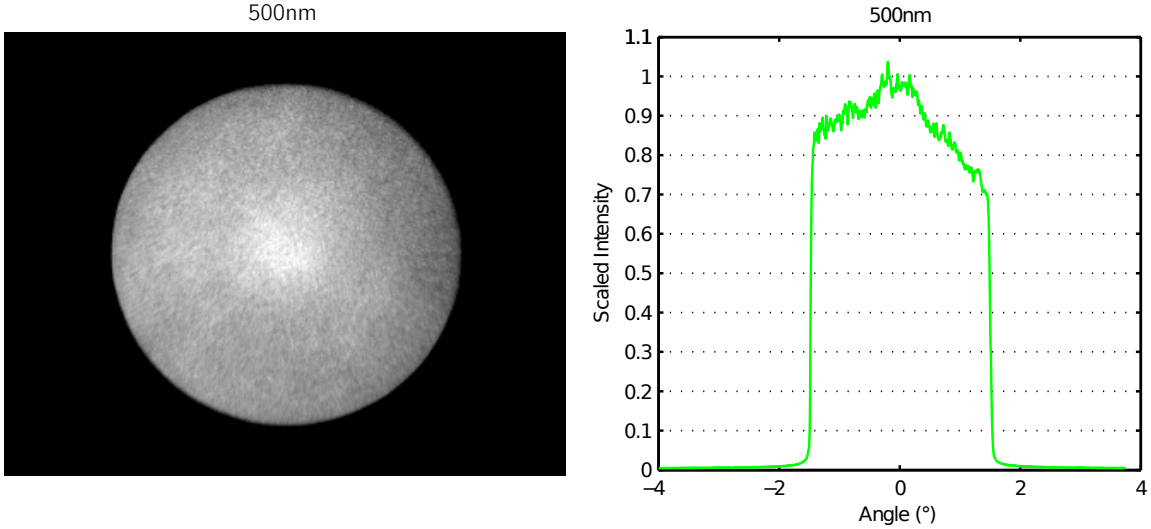

Figure 7-11: Sample image and one-dimensional profile for a projector using a 50° ED with optical reimager and Fresnel lens. Note that the bright ring in the image, and the "shoulder" peaks in the profile, have been clipped by the launch-pupil baffle.

Stray light

As with its 30° counterpart, the efficacy of this projector's stray light suppression depends on the launch-pupil baffle. Here, the iris is again sufficient to cut the light sharply, so that stray light levels are consistently below 2%, and approach ambient light level in the lab.

Spatial uniformity

We had hoped to flatten the profile shape by selecting only the central angles emitted by the Engineered Diffuser. While we did successfully clip the edges, we still had to contend with

the central peak. We found that overall results were on par with those using the 30° ED: σ/μ flatness hovered around 5-15%. Additionally, because light is lost to the baffle, this 50° ED system is less efficient than its 30° counterpart.

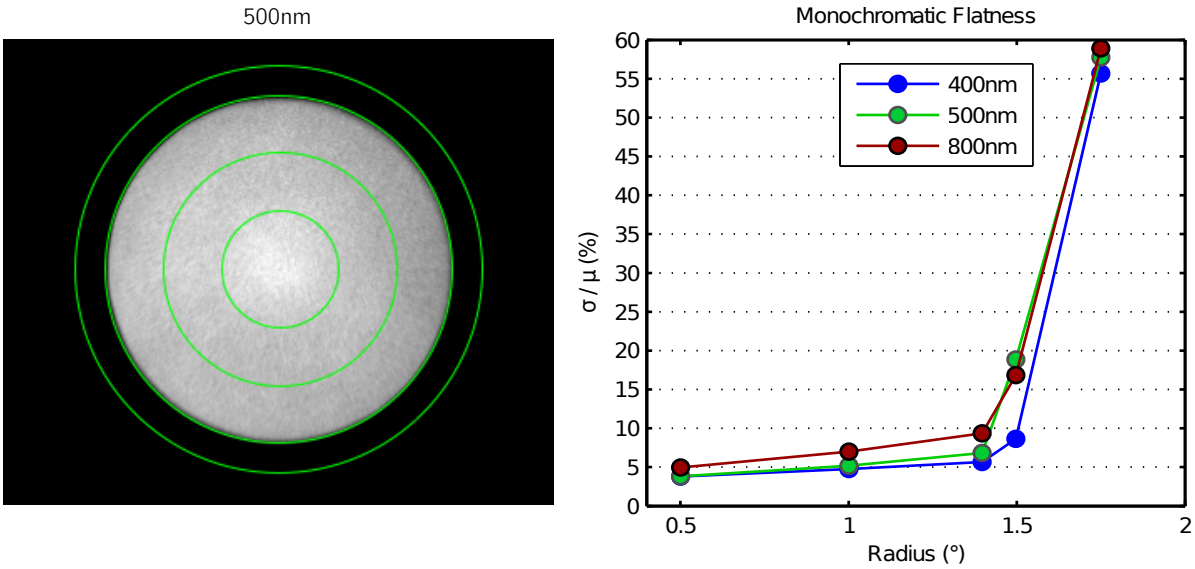

Figure 7-12: Quantitative analysis of flatness of light from a 50° ED, relay optic system, and Fresnel lens.

7.1.3 Chromatic uniformity

Chromatic uniformity with the 50° system was again roughly equal to the 30° version. On axis, color-to-color variation, as measured statistically from ratio images, was on the order of 5%. And again, translating the camera off-axis skewed the color profiles. The 50°-projector equivalent of Figure 7-9 is given in Figure 7-13. Once again, the 400nm profiles are splayed widest.

7.2 Engineered diffuser with parabolic mirror

The prevalence and magnitude of chromatic effects in all Fresnel lens projectors returned us to the reflective collimator option.

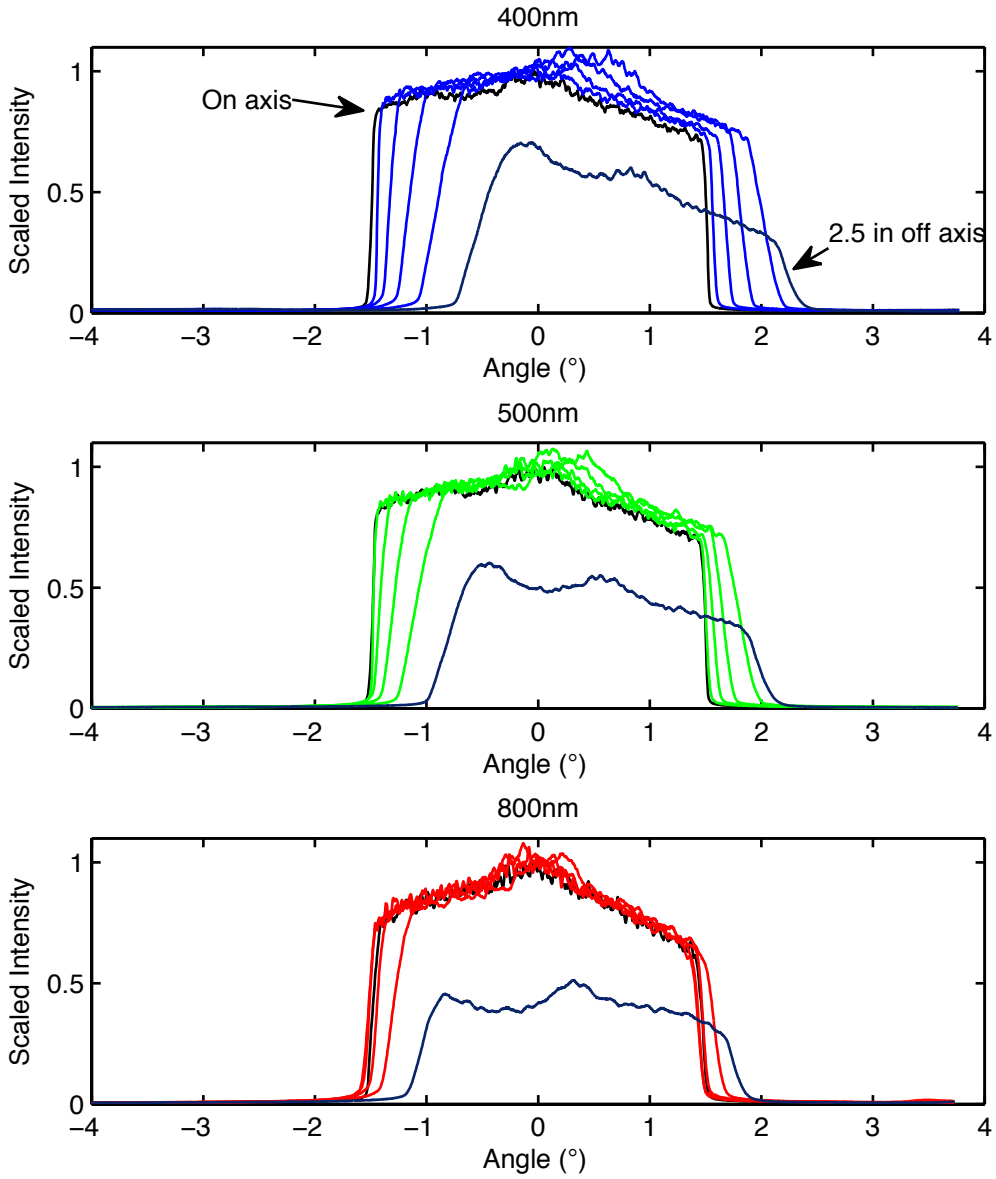

Figure 7-13: One-dimensional single-color plots demonstrating wavelength-dependent shift of off-axis light on the detector, using a 50° ED, optical reimager, and Fresnel lens projector.

7.2.1 30° Engineered Diffuser with optical reimager and parabolic mirror

An alternative projector setup uses the same Engineered Diffusers as above, with the same optical reimaging system, but this time with a parabolic mirror as the collimator. A diagram of this setup is given in Figure 7-14, and representative data in Figure 7-15. The choice of collimating optic should not affect the shape of an on-axis diffuser profile; we attribute the observed edge-dimming to the mirror itself. Because only an annular section of the mirror was reflective, the projection of the pupil image onto the mirror was too wide to be imaged without vignetting. We can get a better idea of the actual one-dimensional profile by taking, instead of a horizontal strip, one that slices through at an unvignetted angle. An illustrative image and its corresponding angular plot are given in Figure 7-16.

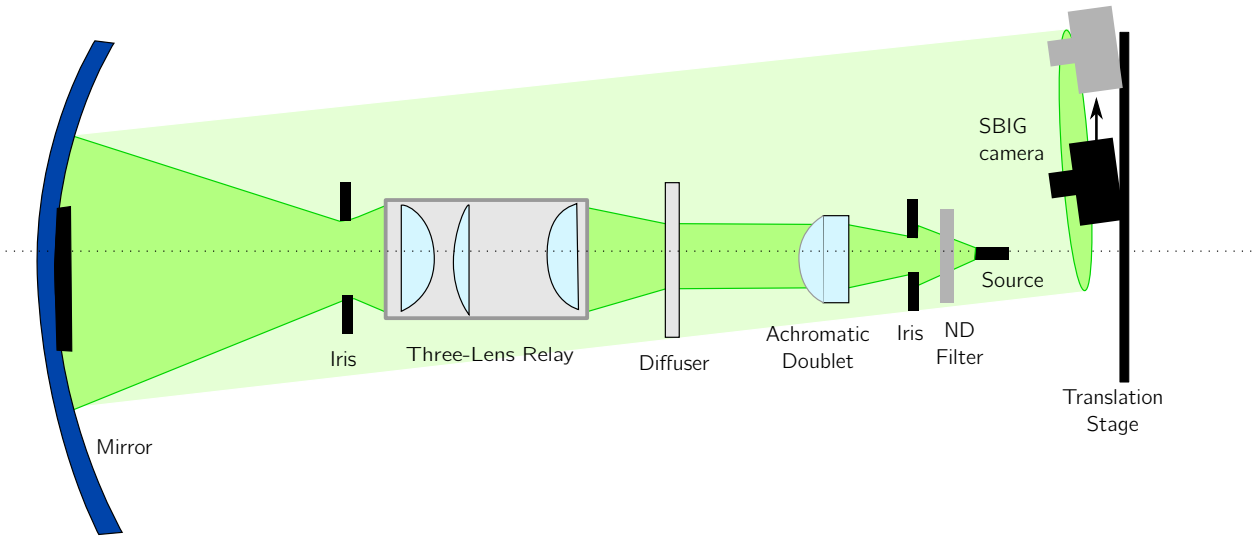

Figure 7-14: Schematic of Engineered Diffuser with reimaging system and parabolic mirror collimator, again showing the camera on translation stages.

Stray light

The stray light characteristics of the projector are largely dependent on baffling at the launch pupil. Stray light in the reflective projector considered here are very similar to those in the

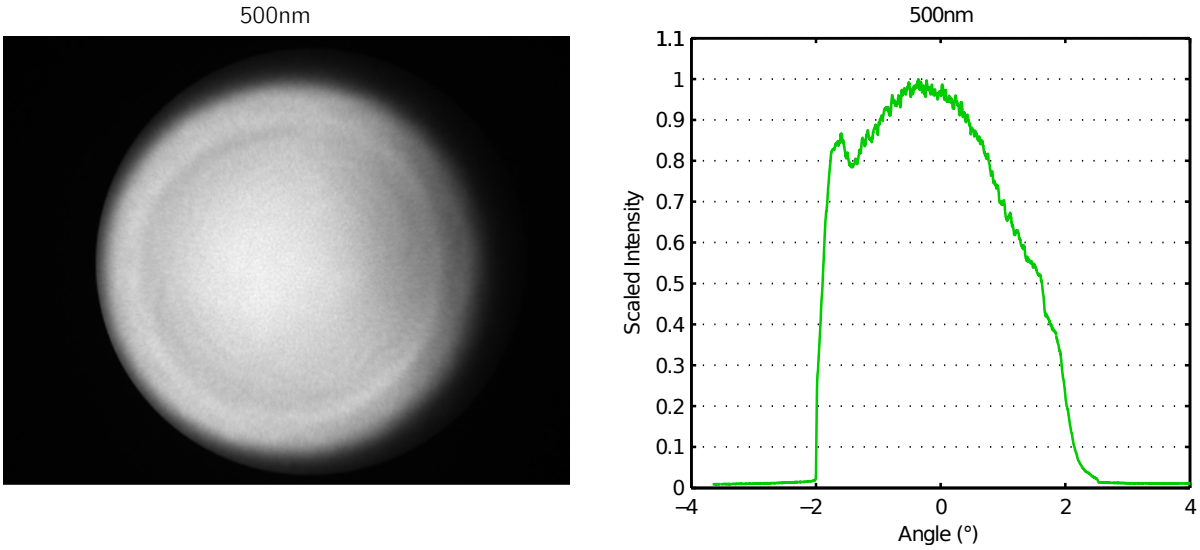

Figure 7-15: Image and plot showing the angular profile of a 30° ED collimated by the mirror, with vignetting due to limited mirror surface area. Because of the relative focal lengths of the particular mirror and Fresnel lens used, the angular dimensions of the bright spot on the detector are larger with the mirror than with the lens collimator. Nevertheless, similarity in the projected pattern is apparent in both the image – note the ring structure – and the brighter side of the profile.

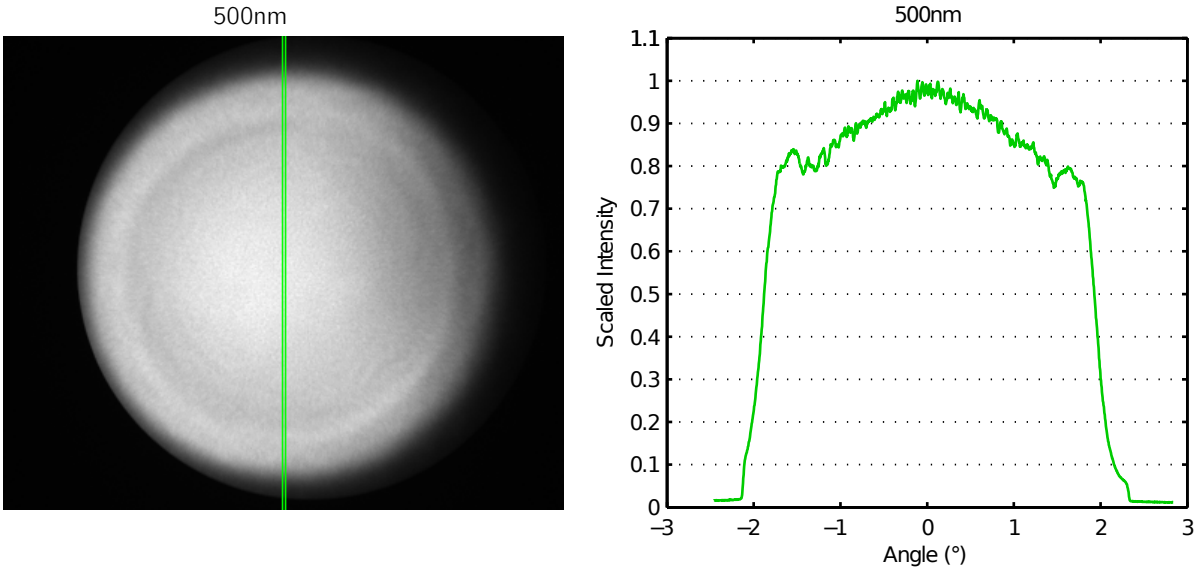

Figure 7-16: Image and plot showing the angular profile of 30° ED with mirror collimator taken across an unvignetted strip (green rectangle in image). Note the similarity to earlier profiles made with the same diffuser and Fresnel lens collimator.

transmissive-collimator variant considered above. As before, light falloff is sharp, and counts outside the projected beam are on the order of 1-2%.

Spatial uniformity

Single-wavelength spatial uniformity, too, is similar to that seen with the transmissive collimator. Although vignetting made statistical analysis difficult, inspection of profiles indicates that σ/μ variation is again on the order of 5-15%. We take the pixel-to-pixel uniformity of an on-axis image made with a reflective collimator to be approximately equal to that of its Fresnel lens-collimator counterpart. More critical is any possible gain in chromatic uniformity achieved by choosing the mirror.

Chromatic uniformity

Because the mirror is an entirely reflective optic, we expect that it contribute no dispersive effects. Any chromatic variation, then, should be limited to what is intrinsic to the diffuser. To verify the achromatic nature of this system, we repeated the process of translating the camera laterally, as with the Fresnel lens system: a diagram of the procedure is given in Figure **??**.

Figure 7-17 repeats the earlier experiment of Figure 7-7, once again coloring individual frames with representative RGB values. The top image, as before, shows on-axis profiles, the middle a series of frames taken at various wavelengths with the camera fixed off-axis, and the bottom a stack of frames at 400nm as the camera moves from on-axis to off-axis positions. Note that, in contrast to the Fresnel lens system presented in Figure 7-7, no chromatic spread is evident by inspection.

The severity of mirror vignetting makes close analysis a little more complex. We can, however, construct the analog to 7-9 by plotting even the vignetted profiles at a single wavelength as the camera is translated. Figure 7-18 presents these results at 400nm, which was the most dramatically affected of the tested wavelengths in the Fresnel lens trials.

We conclude that although the mirror eliminates chromatic aberration seen in the Fresnel

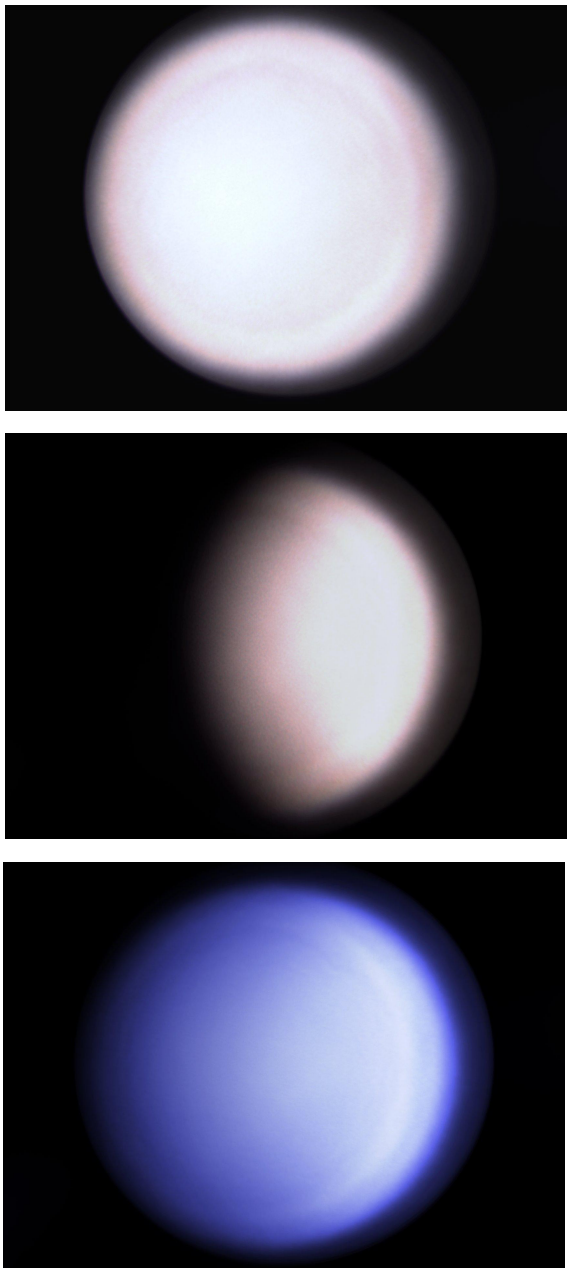

Figure 7-17: Synthetically colored images demonstrating lack of chromatic effects in the mirror system. Top: synthetic-color image of on-axis light at 400, 500, 600, and 800nm; single-color frames have been stacked and colored by computer. Again, colors are arbitrarily chosen; images here are for illustration only. Middle: a synthesized image of multiple filters with off-axis camera. Images are vignetted due to mirror size, but frames at different filters are not displaced relative to one another. Bottom: a synthesized image made of individual data images, all at 400nm, showing neither displacement nor distortion beyond simple vignetting.

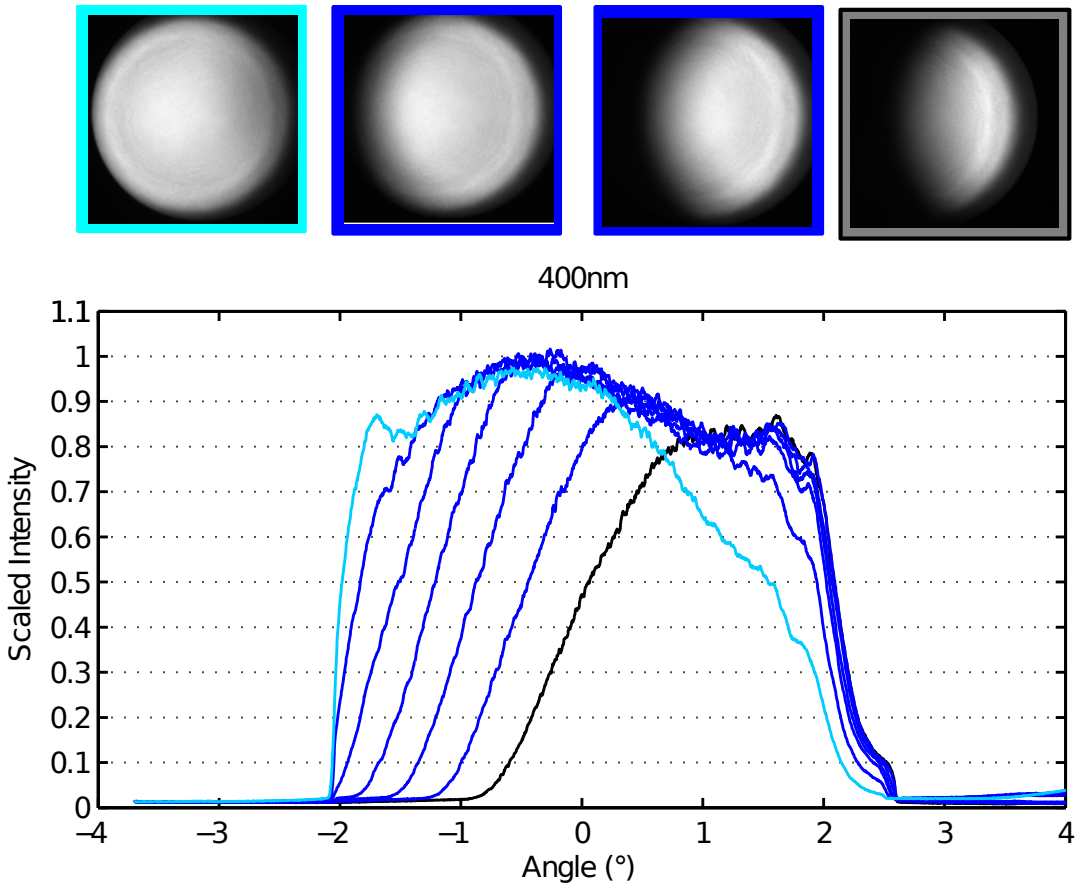

Figure 7-18: As a mirror-collimator analog to Figure 7-9, we plot 400nm profiles versus camera translation. Limited surface area of the mirror causes vignetting of the images (top), but no relative translation – where the profiles overlap, their shapes align well (bottom).

lens systems, color-to-color wavelength variation intrinsic to the Engineered Diffuser is still present, and is on the order of 5-15%.

7.3 Proof of concept

Thus far, no system evaluated here has been either completely flat or completely achromatic. The Engineered Diffusers introduce intensity variation both between pixels at a single color, and between colors at a single pixel. The Fresnel lens collimator introduces further chromatic effects. One might wonder whether it is at all feasible to construct a projected image that is flat, constrained, and achromatic. This section will demonstrate that such a system is, in fact, possible: that the concept is sound and can be constructed in the lab.

7.3.1 The integrating sphere projector

For the proof-of-concept system, we choose the mirror as collimating optic. All tested Fresnel lenses were simply too chromatic. As launch optic, we abandon the Engineered Diffuser and instead turn to an element that has often been used as a standard of uniform irradiance, and which we used earlier to calibrate the test camera: the integrating sphere.

An integrating sphere is a hollow spherical element whose inner surface is coated with broadband scattering material. Several ports are cut into the sphere to allow light in, via an optical fiber, and out, via an aperture.For our purposes, the crucial property of an integrating sphere is this: given an output port much smaller than the diameter of the sphere, irradiance seen across that port is approximately flat. More specifically, for angles less than 10°, irradiance follows a $\cos^4$ falloff Lab. Thus, light viewed10° from the center of the integrating sphere port will be approximately 94% as bright as light at the center. We used an integrating sphere with a full diameter of 2" and an output port diameter of 0.5".

The optical reimaging systems described in earlier sections created a projected image at the intermediate pupil plane. The integrating sphere instead places a physical aperture at this pupil plane, where the physical diameter of the aperture limits the angular extent of the image at the detector. Because the integrating sphere aperture is not a physical surface, it is not subject to dust or degradation; because light exits only after multiple bounces, it is highly uniform and is independent of small irregularities in the sphere's inner surface. A diagram of the integrating sphere setup is shown in Figure 7-19.

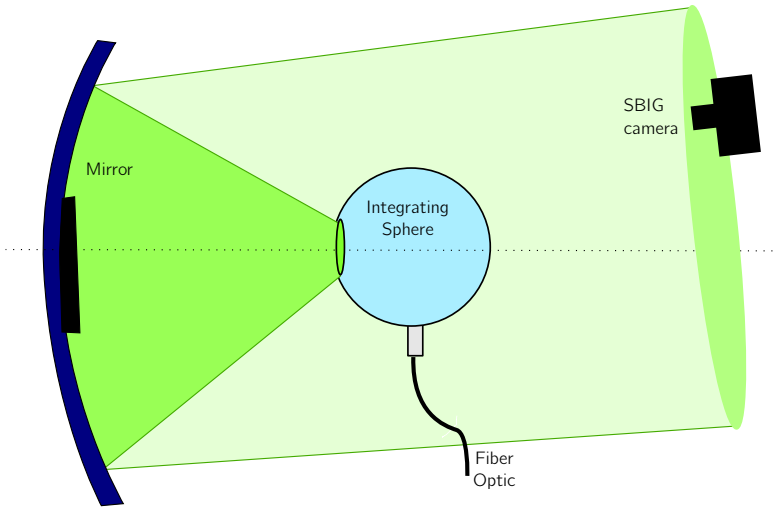

Figure 7-19: Schematic of projector setup using integrating sphere and parabolic mirror. The aperture of the integrating sphere is placed at the focus of the parabolic mirror, where the size of the aperture and the mirror's focal length then determine the maximum divergence angle of the projected beam. Light is again measured by the SBIG test camera with Nikon lens.

Data taken using the integrating sphere prototype are promising. We evaluate the integrating sphere projector as we have for each previous prototype: for stray light, spatial uniformity, and chromatic uniformity.

Stray light

The integrating sphere has a physically delimited aperture whose walls function much like the iris placed at the launch pupil in Engineered Diffuser designs. Here, too, light incident on the detector outside the desired range is minimal, and the falloff is steep. A sample image and one-dimensional profile are shown in Figure 7-20. Note that the entire projected beam spans less than two degrees on the detector: the aperture of this particular integrating sphere is too small, or the mirror's focal length too long, to match the LSST's field of view. That problem, though, is simply one of geometry and of available laboratory equipment.

Very little light is detected outside the projected beam. On the detector , light beyond 1° from the beam center is only at the level of 1%. The integrating sphere projector successfully

minimizes stray light.

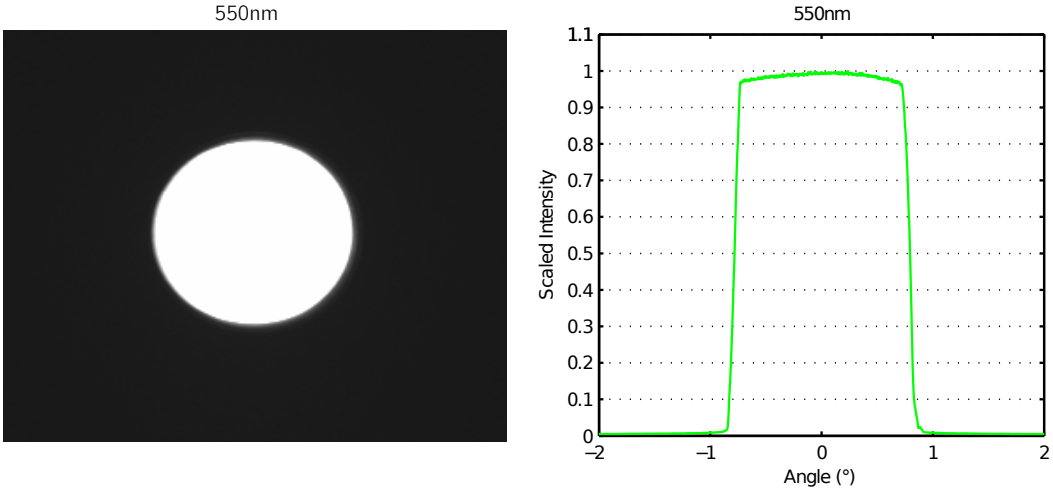

Figure 7-20: Images and plot showing single-profile flatness.

Spatial uniformity

The integrating sphere produces a very flat single-wavelength profile on inspection: a representative image in Figure 7-20 is a bright circle with no evidence of structure on inspection, and the corresponding one-dimensional profile shows only the geometrical edge-dimming we expect. We can quantify the system's flatness as we have done earlier, by measuring average deviation within concentric regions. Results are given graphically in Figure 7-21 : the integrating sphere shows spatial variation only on the level of 1-3%. It outperforms all previous projector incarnations in pixel-to-pixel uniformity.

Chromatic uniformity

Finally, the integrating sphere projector is much more chromatically uniform than any of the diffuser setups tested. Because the projector system has no transmissive element, wavelength-dependent refractive indices contribute no dispersive behavior. Consequently, we expect good agreement between profiles at different wavelengths. Figure 7-22 shows single-wavelength

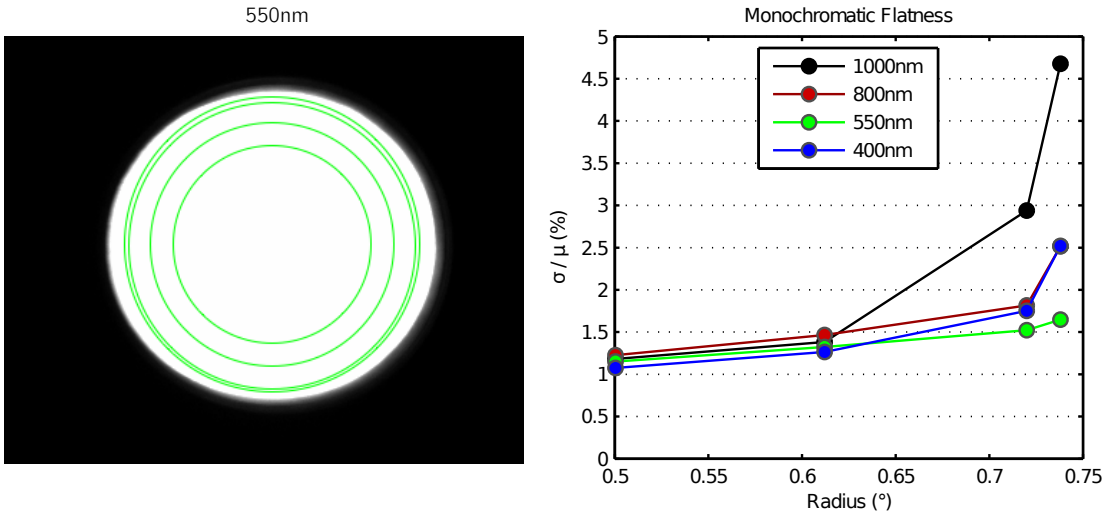

Figure 7-21: Flatness measured as σ/μ for the integrating sphere projector at wavelengths from 400 to 1000nm. Circles in the image denote radii from 0.5° (innermost) to 0.74° (outermost). Angles beyond 0.72° are subject, at some wavelengths, to edge effects due to chromatic aberration in the Nikon lens.

profiles plotted on a single axis. Unlike the Engineered Diffuser profiles, traces across the integrating sphere aperture line up almost exactly at wavelengths from 400 to 1000nm.

We can quantify chromaticity by again measuring deviation in divided images, as presented in Figure 7-23. Note that the divided image is a very even gray across its circle. Divided-image uniformity within the gray circle is on the order of 0.8-1.8%. Figure 7-24 depicts one-dimensional profiles of the divided images, plotted on a single set of axes. In order to make the variation apparent, we have zoomed in on the y-axis. The peak-to-peak chromatic variation is only at the level of a few percent.

The potential problem with the integrating sphere is its efficiency. Part of the appeal of the Engineered Diffuser was that little light is lost in transit: nearly all rays emerging from the launch optic are usable for flat-fielding. Integrating spheres, though, rely on multiple reflections from their internal surface to achieve uniform brightness across the output port. In order for the profile across the output port to be flat within a few percent, the port must be small compared to the sphere diameter. Integrating sphere efficiency scales with larger output port. An integrating sphere with a small port will produce flat illumination across its

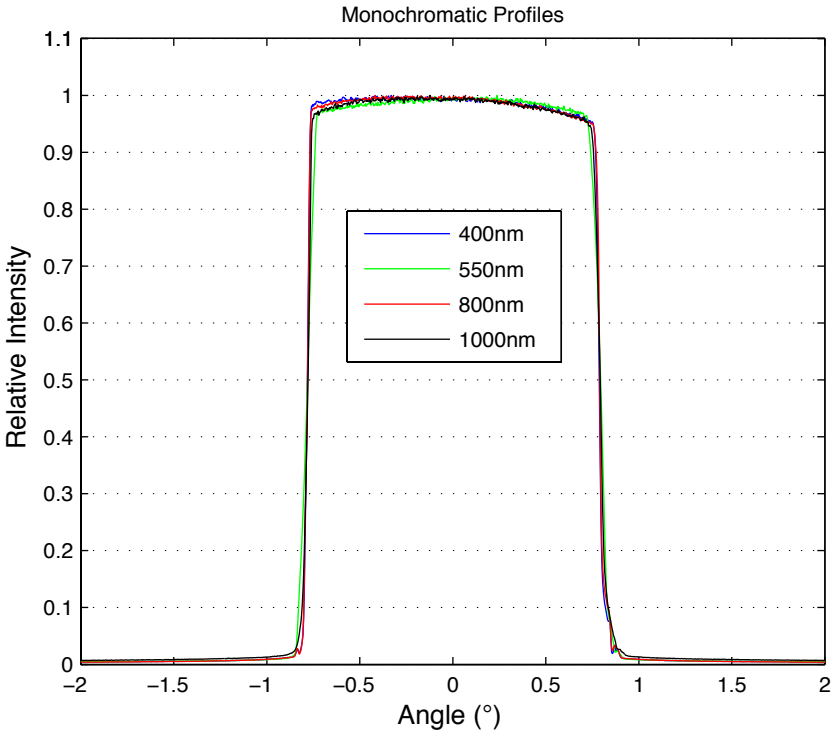

Figure 7-22: Overlaid one-dimensional integrating sphere profiles at wavelengths from 400 to 1000nm. Profiles show very close agreement between colors.

aperture, but will be inefficient; a more efficient larger port will be less uniform in brightness. The balance between uniformity and efficiency can be tailored by varying the dimensions of the sphere itself, and we plan further investigation to determine where the optimum balance might fall.

Figure 7-25 shows an estimate of the relative efficiency of full projector setups – measured as relative counts detected at the CCD, scaled by exposure time – using the integrating sphere, the 30° Engineered Diffuser, and a Lambertian opal glass diffuser. The opal glass was placed at the launch pupil in an attempt to approximate an integrating sphere surface. These data seem to indicate that the integrating sphere is on the order of 60% as efficient as a diffuser – however, it must be noted that the ED efficiency is artificially low. In the ED projectors, much light from the fiber is lost in the initial creation of the collimated beam incident on the diffuser surface, and the amount of light lost in fiber collimation is

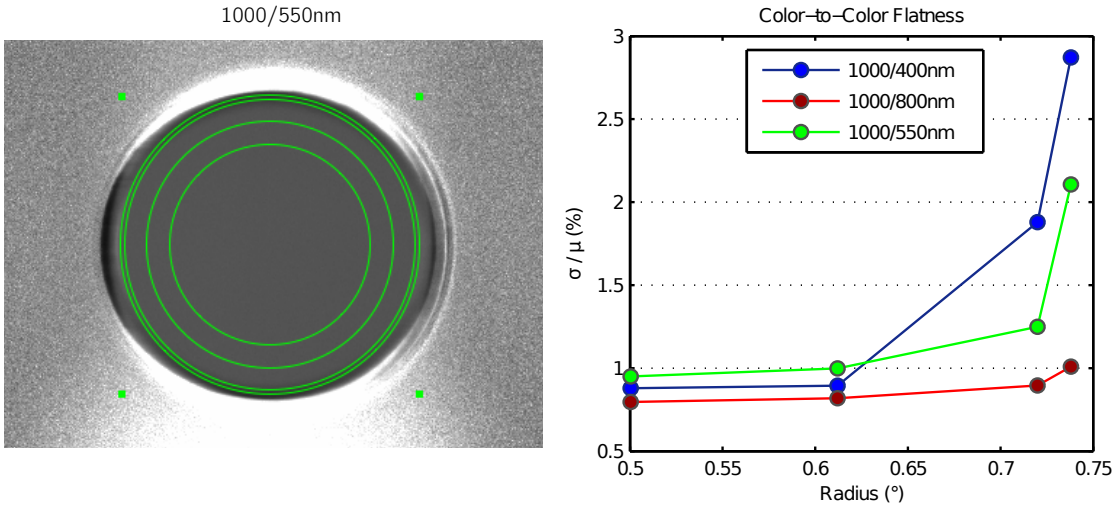

Figure 7-23: Quantitative analysis of color-to-color uniformity in the integrating sphere projector, measured as σ/μ for ratios of two wavelengths. Left: a sample image showing the ratio of 1000nm to 550nm. Circles in the image denote radii from 0.5° (innermost) to 0.74° (outermost). Chromatic aberration due to the Nikon lens is responsible for the bright areas just above and below the flat gray circle.

dependent on the particular collimating lens used. No effort was made, in our tests, to construct a particularly efficient fiber collimator.

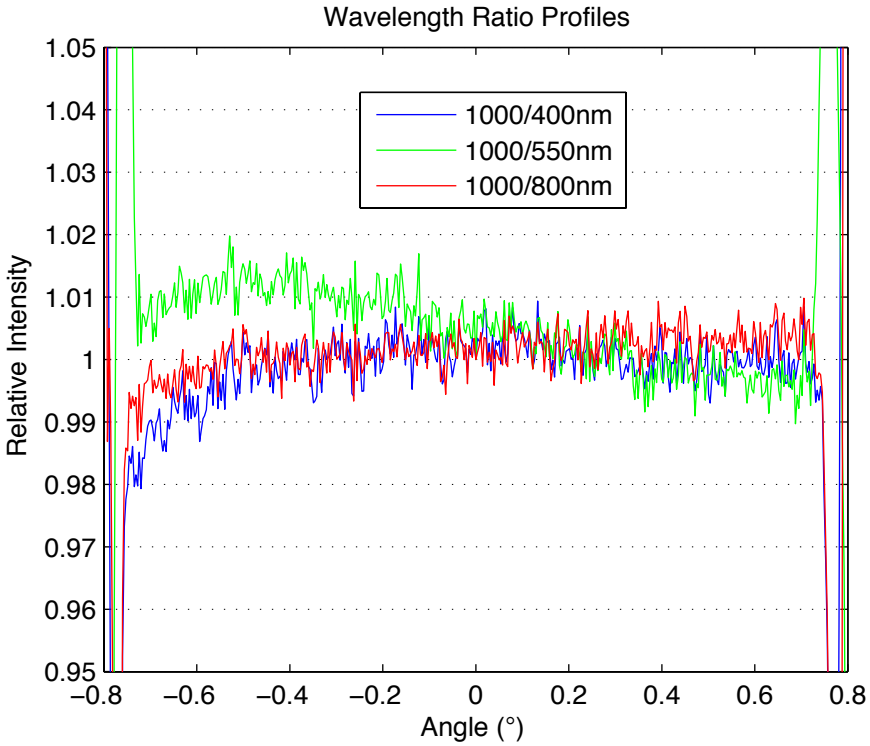

Figure 7-24: Overlaid profiles of ratios between wavelengths with the integrating sphere projector. We have zoomed in on the y-axis.

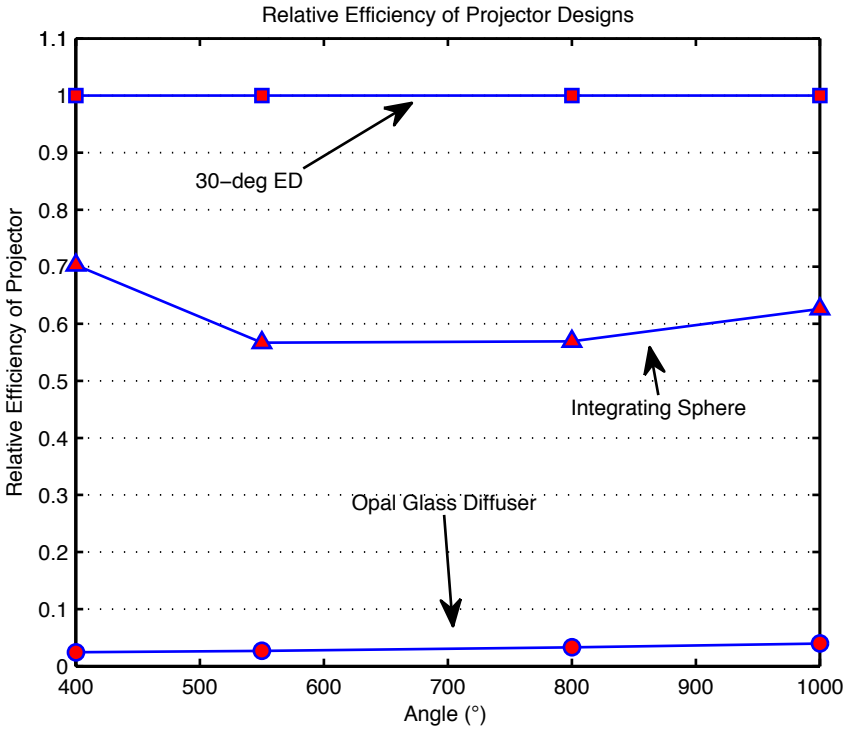

Figure 7-25: Plot showing relative efficiency of integrating sphere vs diffusers.

Chapter 8

Summary, Conclusions, and Future Development

8.1 Summary of Results

We have tested components and full prototypes of calibration projectors for use at the LSST. In hope of countering the main sources of systematic uncertainty reported in previous iterations of in-situ throughput calibration, we have evaluated the output of each projector prototype along the axes of stray light containment, single-wavelength spatial uniformity at the detector plane, and single-pixel uniformity across wavelengths. A complete summary of measured results is tabulated in Table 8.1.

8.1.1 Extrapolating results to the projector array

The final goal of LSST throughput calibration is photometric precision at the 1% level. In order to do so, we require that the final distribution of intensity across the focal plane be *known* to well within 1% at every pixel and at every wavelength measured.

The full-scale LSST design calls for not one projector, but many: between 100 and 200 projectors will pack to form the calibration "screen". Because each projector illuminates a substantial fraction of the telescope primary mirror, we can expect to benefit from statistical

Stray Light Control

Projector	10%-to-90% falloff distance	Background light level
4° ED Alone	0.5°	2-5%
30° ED+reimager+Fresnel	0.3°	1-2%
50° ED+reimager+Fresnel	0.2°	1-2%
30° ED+reimager+mirror	0.3°	1-2%
Integrating sphere + mirror	0.05°	1-2%

Spatial Uniformity

Projector	σ/μ Flatness	
	Within Central 0.5°	Across Total Circle
4° ED Alone	1.1 - 2.0%	7.5 - 8.5%
30° ED+reimager+Fresnel	3.8 - 5.0%	5 - 10%
50° ED+reimager+Fresnel	3 - 5%	8 - 15%
30° ED+reimager+mirror	3 - 5%	5 - 10%
Integrating sphere + mirror	1.1 - 1.3%	1.5 - 3%

Chromatic Uniformity

Projector	σ/μ Flatness Across Measured Wavelength Range	
	Within Central 0.5°	Across Total Circle
4° ED Alone	1.1 - 2.0%	5%
30° ED+reimager+Fresnel	2%	14%
50° ED+reimager+Fresnel	4%	7%
30° ED+reimager+mirror	4%	14%
Integrating sphere + mirror	0.8%	1.8%

Table 8.1: Summary of benchtop tests on all projector prototypes.

averaging of individual projector variation *as long as that variation is randomized with angle*. Non-random angular patterns, however, would not be averaged out: a telescope is designed to map the angle of incoming light to position on its focal plane. As long as each projector is projecting a dome-and-ring, the telescope focal plane will also detect a dome-and-ring.

Because we can compensate for wavelength-independent variation by rastering a celestial source across the detector, spatial uniformity is not strictly necessary. Chromatic uniformity, however, is. The Engineered Diffusers have wavelength variation due to large scale structure in their angular radiance – the position of the entire bright ring, in their patterns, moves inward at redder wavelengths. Because this structure is not randomized but systematic, the

final array of 100-200 projectors would not benefit from any averaging effects. Therefore, in order for us to use an Engineered Diffuser in a projector system, the chromatic non-uniformity of each projector would have to be within our 1% tolerances. Unfortunately, the observed variation is instead on the order of 10%: far too high for our purposes.

Of the designs tested, only the integrating sphere approaches the required level of single-pixel color-to-color uniformity. The integrating sphere shows no evidence of large scale structure variation with wavelength. Because variation in integrating sphere output port illumination is randomizable – by rotating spheres in different projectors relative to one another, for instance, or by varying the location of the input fiber on different spheres – we can expect some averaging effects from an array of integrating-sphere-type projectors. Given an array of 100 projectors, we can expect random variation to be reduced by a factor of ten. Even the highest measured chromatic variation of 2%, then, is more than sufficient.

8.2 Conclusions

Work in this thesis spans a range of optical measurements, including evaluation of 1) the concept of a calibration projector as an alternative to a widely-scattering screen, 2) components for use within such a projector, and 3) prototypes of a single full projector. Our final conclusions, then, are as follows:

We have evaluated the behavior of top-hat Engineered Diffusers in monochromatic light from 400 to 1000nm. We found that the top-hat Engineered Diffuser has a persistent characteristic structure leading to peak-to-peak brightness variations at the level of 10-20% across the "flat" top. Additionally, the top-hat ED has persistent chromatic dependence, leading to visible differences in the pattern of angular radiance between colors – and, in our system, to persistent single-pixel variation with wavelength on the order of 5-10%.

We have further evaluated these Engineered Diffusers as part of a calibration projector whose goal is to produce an angularly constrained, chromatically uniform, monochromatic beam across a telescope pupil. Here, we found that color-to-color uniformity was difficult to achieve. We attribute part of this difficulty to intrinsic ED variation, and part to the sig-

nificant chromatic aberration present in Fresnel lenses. Consequently, unless an achromatic counterpart can be designed, we advocate abandoning Fresnel lenses as collimating optics for this particular projector.

Of the Engineered Diffuser projectors tested, none were sufficiently flat in color – or sufficiently stochastic in the pattern of their chromatic variation – to suit our purposes. Nevertheless, we have repeatedly demonstrated the feasibility of the calibration *projector*, as opposed to the calibration *screen*: we have constructed systems which suppress uncertainty due to stray light by tailoring the paths of available photons to those within the field of view of the instrument.

Finally, we have demonstrated the feasibility of a projector which satisfies all of our criteria – angular constraint, spatial uniformity, and chromatic uniformity at the necessary level – by using an integrating sphere as the launch optic.

8.3 Future Work

The magnitude of improvement seen with the integrating sphere prototype suggests that as an alternative to improving the ED projector, we move instead toward more thorough investigating of the integrating sphere concept. The advantages of a fully reflective system are striking: no transmissive elements means no concern about dispersive effects. Questions to be investigated with the integrating sphere concern the balance between efficiency and uniformity: how much more light can we get out of the integrating sphere while maintaining tolerable uniformity? How many surface reflections on a sphere are necessary to suitably average over any irregularities – and might we mimic the multiple-scattering behavior with another, more efficient, setup?

Longer term work will move from the single projector to the full array to be placed in the LSST. We must design, for instance, a system to measure each projector's intensity relative to others in the array, and to balance their light accordingly. Work presented in this thesis represents a single step towards the final goal of a telescope whose throughput can be precisely measured – a telescope whose combined calibration methodologies will render it

capable of 1% photometry, and allow us to observe the universe with a more discerning eye.

Bibliography

R. C. Bohlin. HST Stellar Standards with 1% Accuracy in Absolute Flux. In C. Sterken, editor, *The Future of Photometric, Spectrophotometric and Polarimetric Standardization*, volume 364 of *Astronomical Society of the Pacific Conference Series*, pages 315–+, April 2007.

G. P. Eppeldauer, H. W. Yoon, Y. Zong, T. C. Larason, A. Smith, and M. Racz. Radiometer standard for absolute responsivity calibrations from 950 nm to 1650 nm with 0.05 % (k=2) uncertainty. *Metrologia*, 46(139), February 2009.

W. J. Gressler, P. Doherty, V. L. Krabbendam, M. Liang, A. Saha, C. W. Stubbs, and A. Vaz. Calibration dome screen for the Large Synoptic Survey Telescope. In *Society of Photo-Optical Instrumentation Engineers (SPIE) Conference Series*, volume 7739 of *Society of Photo-Optical Instrumentation Engineers (SPIE) Conference Series*, July 2010. doi: 10.1117/12.857425.

Ž. Ivezić, J. A. Tyson, R. Allsman, J. Andrew, R. Angel, and for the LSST Collaboration. LSST: from Science Drivers to Reference Design and Anticipated Data Products. *ArXiv e-prints*, May 2008.

Ž. et al Ivezić. *The LSST System Science Requirements Document*. The LSST Science Council, http://www.lsst.org/files/docs/SRD.pdf, v5.1.3 edition, May 2010.

S. Kent, M. B. Kaiser, S. E. Deustua, J. A. Smith, S. Adelman, S. Allam, B. Baptista, R. C. Bohlin, J. L. Clem, A. Conley, J. Edelstein, J. Elias, I. Glass, A. Henden, S. Howell, R. A. Kimble, J. W. Kruk, M. Lampton, E. A. Magnier, S. R. McCandliss, W. Moos, N. Mostek, S. Mufson, T. D. Oswalt, S. Perlmutter, C. Allende Prieto, B. J. Rauscher, A. Riess, A. Saha, M. Sullivan, N. Suntzeff, A. Tokunaga, D. Tucker, R. Wing, B. Woodgate, and E. L. Wright. Photometric Calibrations for 21st Century Science. In *astro2010: The Astronomy and Astrophysics Decadal Survey*, volume 2010 of *ArXiv Astrophysics e-prints*, pages 155–+, 2009.

A Guide to Integrating Sphere Theory and Applications. Labsphere.

E. V. Linder and D. Huterer. Importance of supernovae at z>1.5 to probe dark energy. *Phys.Rev. D*, 67(8):081303–+, April 2003. doi: 10.1103/PhysRevD.67.081303.

LSST Science Collaborations, P. A. Abell, J. Allison, S. F. Anderson, J. R. Andrew, J. R. P. Angel, L. Armus, D. Arnett, S. J. Asztalos, T. S. Axelrod, and et al. LSST Science Book, Version 2.0. *ArXiv e-prints*, December 2009.

N. Regnault, A. Conley, J. Guy, M. Sullivan, J.-C. Cuillandre, P. Astier, C. Balland, S. Basa, R. G. Carlberg, D. Fouchez, D. Hardin, I. M. Hook, D. A. Howell, R. Pain, K. Perrett, and C. J. Pritchet. Photometric calibration of the Supernova Legacy Survey fields. *AAP*, 506:999–1042, November 2009. doi: 10.1051/0004-6361/200912446.

A. Saha, A. E. Dolphin, F. Thim, and B. Whitmore. Faint BVRI Photometric Sequences in Selected Fields. *PASP*, 117:37–78, January 2005. doi: 10.1086/427737.

C. Stoughton, R. H. Lupton, M. Bernardi, M. R. Blanton, S. Burles, F. J. Castander, A. J. Connolly, D. J. Eisenstein, J. A. Frieman, G. S. Hennessy, , and et al. Sloan Digital Sky Survey: Early Data Release. *AJ*, 123:485–548, January 2002. doi: 10.1086/324741.

C. W. Stubbs and J. L. Tonry. Toward 1% Photometry: End-to-End Calibration of Astronomical Telescopes and Detectors. *ApJ*, 646:1436–1444, August 2006. doi: 10.1086/505138.

C. W. Stubbs, F. W. High, M. R. George, K. L. DeRose, S. Blondin, J. L. Tonry, K. C. Chambers, B. R. Granett, D. L. Burke, and R. C. Smith. Toward More Precise Survey Photometry for PanSTARRS and LSST: Measuring Directly the Optical Transmission Spectrum of the Atmosphere. *PASP*, 119:1163–1178, October 2007a. doi: 10.1086/522208.

C. W. Stubbs, S. K. Slater, Y. J. Brown, D. Sherman, R. C. Smith, J. L. Tonry, N. B. Suntzeff, A. Saha, J. Masiero, and S. Rodney. Preliminary Results from Detector-Based Throughput Calibration of the CTIO Mosaic Imager and Blanco Telescope Using a Tunable Laser. In C. Sterken, editor, *The Future of Photometric, Spectrophotometric and Polarimetric Standardization*, volume 364 of *Astronomical Society of the Pacific Conference Series*, pages 373–+, April 2007b.

C. W. Stubbs, P. Doherty, C. Cramer, G. Narayan, Y. J. Brown, K. R. Lykke, J. T. Woodward, and J. L. Tonry. Precise Throughput Determination of the PanSTARRS Telescope and the Gigapixel Imager Using a Calibrated Silicon Photodiode and a Tunable Laser: Initial Results. *"The Astrophysical Journal Supplement"*, 191:376–388, December 2010. doi: 10.1088/0067-0049/191/2/376.